Analyse de l'évapotranspiration et du bilan d'énergie de surface d'une forêt boréale humide aux échelles locales et régionales

Thèse

Pierre-Erik Isabelle

Doctorat en génie des eaux
Philosophiæ doctor (Ph. D.)

Québec, Canada

Résumé

La forêt boréale recouvre 30% de la surface du Canada et 14% de la surface émergée de la terre. Les changements climatiques vont fortement l'affecter, et ces écosystèmes vont significativement impacter la climatologie et l'hydrologie mondiale avec des échanges importants d'eau, d'énergie et de carbone entre le sol et l'atmosphère. Il est maintenant crucial de bien comprendre le bilan d'énergie de surface sur ce biome pour efficacement prévoir son comportement et son évolution dans un climat changeant. Beaucoup d'études ont analysé le bilan d'énergie de la forêt boréale, mais des lacunes importantes subsistent : il y a peu d'études en terrain non plat, ou dans des zones recevant d'importantes précipitations, ou encore avec des mesures à des échelles spatiales variées, et encore moins des combinaisons de ces trois possibilités.

Le principal but de cette thèse est d'attaquer ces lacunes de front en offrant l'analyse du bilan d'énergie et de l'évapotranspiration d'une forêt boréale humide couvrant une topographie prononcée, et ce à plusieurs échelles spatiales (point : ~m^2; locale : ~ha; régionale : ~km^2). Les résultats sont principalement basés sur une campagne de mesures ayant cours à la forêt Montmorency de l'Université Laval, à 80 km au nord de Québec, Canada. La forêt est une sapinière à bouleau blanc avec des arbres à divers degrés de maturité. Là, deux tours à flux mesurant tous les termes du bilan d'énergie sont installés depuis l'automne 2015. Trois objectifs spécifiques sont associés à trois échelles spatiales de mesure ou de modélisation dans un gradient allant de l'échelle ponctuelle vers l'échelle régionale.

Dans un premier objectif, l'hétérogénéité spatiale du couvert forestier est caractérisée par des mesures de rayonnement solaire sous-canopée. Ensuite, l'évaluation de la densité de végétation permet de paramétrer un schéma de surface pour obtenir la variabilité de l'évapotranspiration et de ses composantes. Les résultats montrent que même si la transmission du rayonnement est très variable de point en point (entre 7% et 69% sur toute la saison), une moyenne spatiale à l'échelle locale représente bien la zone. Les résultats de modélisation indiquent qu'une forêt plus dense cause légèrement plus d'évapotranspiration totale, car elle évapore plus de précipitations interceptées et transpire plus. Une forêt plus dense évapore toutefois moins d'eau au sol, ce qui peut mener à une humidité du sol accrue dans des conditions de sécheresse momentanée.

Dans le deuxième objectif, l'impact de fortes précipitations sur le bilan d'énergie à l'échelle locale et l'évapotranspiration en forêt boréale est évalué. Pour ce faire, le site principal de la forêt Montmorency est d'abord comparé avec 13 sites en forêt boréale dans le monde sur la base du bilan d'énergie et de l'évapotranspiration. La forêt Montmorency est le site qui reçoit le plus de précipitations avec ~1600 mm a^{-1}. Pour tous les sites, la précipitation reçue est liée à l'évapotranspiration annuelle, et c'est aussi le site principal qui a la plus forte évapotranspiration, avec ~550 mm a^{-1}. Grâce à des mesures précises des débits sortants du bassin versant de 3.5 km^2 contenant les sites de mesure, le bilan hydrique est clairement établi : l'eau

excédentaire provenant des précipitations est principalement évacuée par des débits sortants dans les cours d'eau du bassin versant, à une hauteur de ~1050 mm a^{-1}.

Pour le troisième objectif, la méthode de la scintillométrie à deux longueurs d'onde est testée sur le site d'étude et ses mesures du bilan d'énergie à l'échelle régionale sont comparées à celles à l'échelle locale. Les scintillomètres sont installés à travers une vallée où est également présente une des deux tours à flux. Les faisceaux électromagnétiques parcourent 1347 m à une hauteur variant entre 5 et 100 m et une hauteur efficace de 88 m. Les résultats montrent que les deux montages expérimentaux ont une faible concordance au niveau des paramètres de structure météorologiques, mais une concordance plus qu'acceptable au niveau des flux turbulents. Pour ces derniers, la corrélation entre les scintillomètres et la tour à flux est optimale lorsque les faisceaux électromagnétiques sont entièrement inclus dans la couche de surface atmosphérique. Cependant, comme la hauteur des faisceaux est hautement variable, ceux-ci se retrouvent la plupart du temps en partie dans la couche de surface atmosphérique, ce qui mène à une corrélation tout de même acceptable dans ces circonstances. Néanmoins, les mesures des scintillomètres sont souvent de qualité douteuse lors des périodes nocturnes et lorsque l'atmosphère est stable.

En bref, la forêt boréale étudiée exhibe un bilan d'énergie et une évapotranspiration significativement différents d'autres sites dans des biomes semblables recensés dans la littérature. Cette thèse apporte des précisions importantes sur ce type d'environnement. De plus, la thèse offre des outils méthodologiques rigoureux pour évaluer le bilan d'énergie à diverses échelles spatiales et élabore sur le passage entre ces échelles, une contribution à ne pas négliger pour les modélisateurs hydrologiques et du climat au Canada et dans le monde.

Abstract

The boreal forest covers 30% of Canada's surface and 14% of the earth's land surface. Climate change will severely affect it, and these ecosystems will in turn impact climate and global hydrology with significant exchanges of water, energy and carbon between the soil and the atmosphere. It is now crucial to understand the surface energy balance of this biome to effectively predict its behavior and evolution in a changing climate. Many studies have analyzed the energy balance of the boreal forest, but significant gaps remain: there are little studies in non-flat terrain, or in areas receiving significant rainfall, or with measurements at various spatial scales, let alone combinations of these three possibilities.

The main aim of this thesis is to fill these gaps with a rigorous analysis of the energy balance and evapotranspiration of a boreal forest covering a pronounced topography, and this at several spatial scales (point: ~m^2, local: ~ha, regional: ~km^2). The results are mainly based on a measurement campaign taking place at the Montmorency Forest of Université Laval, 80 km north of Québec, Canada. The forest is a balsam fir – white birch forest with trees of varying degrees of maturity. There, two flux towers are measuring all the energy balance terms since autumn 2015. Three specific objectives are associated with three spatial scales of measurement or modeling in a gradient from the point scale to the regional scale.

In a first objective, the spatial heterogeneity of the forest cover is characterized by sub-canopy solar radiation measurements. Then, the vegetation density evaluation makes it possible to parameterize a land-surface scheme to obtain the variability of the evapotranspiration and its components. The results show that even though the transmission of radiation is highly variable from point to point (seasonal average between 7% and 69%), a spatial average at the local scale represents the area quite well. Modeling results indicate that a denser forest causes slightly more total evapotranspiration because it evaporates more intercepted precipitation and generates more transpiration. A denser forest, however, evaporates less water on the ground, which can lead to increased soil moisture under conditions of momentary drought.

In the second objective, the impact of heavy rainfall on the local energy balance and evapotranspiration in the boreal forest is evaluated. To do this, the main site of Montmorency Forest is first compared with 13 boreal forest sites around the world on the basis of energy balance and evapotranspiration. The Montmorency Forest is the site receiving the most rainfall with ~1600 mm y^{-1}. For all sites, the precipitation received is positively related to annual evapotranspiration, which means the main site has the highest evapotranspiration rates, with ~550 mm y^{-1}. With accurate measurements of the outflow from the 3.5 km^2 watershed containing the Montmorency Forest measurement sites, the water balance is clearly established: excess water from precipitation is mainly discharged through outflows of the watershed, to an extent of ~1050 mm y^{-1}.

For the third objective, the two-wavelength scintillometry method is evaluated at the study site and its regional energy balance measurements are compared to those at the local scale. The scintillometers are installed across a valley where one of the two flux towers is localized. The scintillometers' electromagnetic beams travel 1347 m at a height varying between 5 and 100 m and an effective height of 88 m. The results show that the two experimental systems have a low agreement in terms of the meteorological structure parameters, but a more than acceptable agreement for the turbulent fluxes. For the latter, the correlation between scintillometers and flux tower is optimal when the electromagnetic beams are entirely included in the atmospheric surface layer. However, since the beam height is highly variable, they are more often than not partially present in the atmospheric surface layer anyway, which leads to a correlation that is still acceptable in these circumstances. However, measurements of scintillometers are often unrealistic during nocturnal periods and when the atmosphere is stable.

In short, the studied boreal forest exhibits an energy balance and evapotranspiration significantly different from other sites in similar biomes referenced in the literature. This thesis provides important details on this type of environment. In addition, the thesis offers rigorous methodological tools to assess the energy balance at various spatial scales and elaborates on the possibility of upscaling and/or downscaling results, a contribution not to be overlooked for hydrological and climate modelers in Canada and around the world.

Table des matières

Liste des tableaux

Liste des figures

Liste des variables

Variable	Identification	Unités
A	Âge du peuplement d'arbres	an
A_A	Aire du bassin A	m^2
A_{AB}	Somme des aires des bassins A et B	m^2
A_B	Aire du bassin B	m^2
$A_{q,LAS}$	Coefficient décrivant q pour le LAS	-
$A_{q,MWS}$	Coefficient décrivant q pour le MWS	-
$A_{T,LAS}$	Coefficient décrivant T pour le LAS	-
$A_{T,MWS}$	Coefficient décrivant T pour le MWS	-
Bo	Rapport de Bowen (= H / L_vE)	-
c_p	Chaleur spécifique de l'air humide	$J\ kg^{-1}\ K^{-1}$
$c_{p,s}$	Chaleur spécifique du sol	$J\ m^{-3}\ K^{-1}$
$c_{p,veg}$	Chaleur spécifique d'une composante d'un arbre	$J\ kg^{-1}\ K^{-1}$
$c_{p,water}$	Chaleur spécifique de l'eau	$J\ m^{-3}\ K^{-1}$
CF	Fraction de fermeture du bilan d'énergie	-
C_n^2	Paramètre de structure de l'indice de réfraction de l'air	$m^{-2/3}$
$C_{n,LAS}^2$	C_n^2 mesuré par le LAS	$m^{-2/3}$
$C_{n,MWS}^2$	C_n^2 mesuré par le MWS	$m^{-2/3}$
$C_{n,LAS\ LAS}$	Équivalent de $C_{n,LAS}^2$	$m^{-2/3}$
$C_{n,OMS}$	C_n^2 obtenu par la covariance entre LAS et MWS	$m^{-2/3}$
$C_{n,MWS\ MWS}$	Équivalent de $C_{n,MWS}^2$	$m^{-2/3}$
C_q^2	Paramètre de structure de l'humidité de l'air	$kg^2\ kg^{-2}\ m^{-2/3}$
C_T^2	Paramètre de structure de la température de l'air	$K^2\ m^{-2/3}$
C_{Tq}	Paramètres de structure combiné température-humidité	$K\ kg\ kg^{-1}\ m^{-2/3}$
C_y^2	Paramètre de structure d'une variable y	$[y]\ m^{-2/3}$
d_0	Hauteur de déplacement du plan zéro	m

D	Déficit de tension de vapeur dans l'air	Pa
D_{yy_t}	Fonction de structure temporelle de la variable y	$[y]^2$
D_{yy_x}	Fonction de structure spatiale de la variable y	$[y]^2$
E	Évapotranspiration	mm
E^*	Évapotranspiration, non-corrigée pour déséquilibre du bilan énergétique	mm
E_{AB}	Évapotranspiration moyenné du bassin AB	mm
E_g	Évaporation au sol	mm
E_i	Évaporation de précipitations interceptées	mm
$E_{Juvenile}$	Évapotranspiration à la tour Juvénile	mm
E_p	Évapotranspiration potentielle	mm
$E_{Sapling}$	Évapotranspiration à la tour Gaule (« Sapling »)	mm
E_t	Transpiration	mm
f_d	Fraction diffuse du rayonnement solaire ($=K_a{\otimes} / K_a$)	-
f_q	Fonction de similarité pour l'humidité spécifique	-
f_T	Fonction de similarité pour la température	-
g	Constante gravitationnelle (= 9.81 m s^{-2})	m s^{-2}
G	Flux de chaleur dans le sol	W m^{-2}
h_v	Hauteur de végétation (arbres)	m
H	Flux de chaleur sensible	W m^{-2}
H_{EC}	Flux de chaleur sensible, covariance des tourbillons	W m^{-2}
H_{TWd}	Flux de chaleur sensible, scintillomètre, méthode TW dépendante	W m^{-2}
H_{TWi}	Flux de chaleur sensible, scintillomètre, méthode TW indépendante	W m^{-2}
i	Identifiant d'une classe dans une distribution de probabilité	-
I_{LAS}	Intensité du signal du LAS	mV
I^0_{LAS}	Moyenne mobile de période ω de l'intensité du signal du LAS	mV
I_{MWS}	Intensité du signal du MWS	mV
I^0_{MWS}	Moyenne mobile de période ω de l'intensité du signal du MWS	mV
k_{LAS}	Nombre d'onde (2π / λ) du LAS	m^{-1}

k_{MWS}	Nombre d'onde (2π / λ) du MWS	m^{-1}
K	Rayonnement solaire	W m^{-2}
K_a	Rayonnement solaire au-dessus de la canopée	W m^{-2}
$K_a\otimes$	Rayonnement solaire diffus au-dessus de la canopée (= f_d K_a)	W m^{-2}
K_d	Rayonnement solaire incident	W m^{-2}
K_m	Rayonnement solaire réfléchi	W m^{-2}
K_u	Rayonnement solaire sous-canopée	W m^{-2}
L	Longueur du trajet du scintillomètre	m
L_d	Rayonnement de longues longueurs d'onde incident	W m^{-2}
L_m	Rayonnement de longues longueurs d'onde émis par la surface	W m^{-2}
LAI	Indice de surface foliaire (« leaf area index »)	m^2 m^{-2}
L_{Ob}	Longueur d'Obukhov	m
L_v	Chaleur latente de vaporisation de l'eau	J kg^{-1}
L_vE	Flux de chaleur latente	W m^{-2}
L_vE_{EC}	Flux de chaleur latente, covariance des tourbillons	W m^{-2}
L_vE_{TWd}	Flux de chaleur latente, scintillomètre, méthode TW dépendante	W m^{-2}
L_vE_{TWi}	Flux de chaleur latente, scintillomètre, méthode TW indépendante	W m^{-2}
m_{veg}	Masse d'une composante d'un arbre	kg
n	Nombre de classe d'une distribution de probabilité	-
N	Taille d'échantillon	-
O	Débit sortant d'un bassin versant	mm
P	Précipitation	mm
P_{clim}	Moyenne climatologique de la précipitation annuelle	mm
P_g	Précipitation atteignant le sol	mm
$P_{r,EC}$	Probabilité d'occurrence, rayonnement net, empreinte 50%, covariance des tourbillons	-
$P_{r,SC}$	Probabilité d'occurrence, rayonnement net, empreinte 50%, scintillomètre	-
$P_{v,EC}$	Probabilité d'occurrence, hauteur de végétation, empreinte 50%, covariance des tourbillons	-

$P_{v,SC}$	Probabilité d'occurrence, hauteur de végétation, empreinte 50%, scintillomètre	-
q	Humidité spécifique de l'air	kg kg^{-1}
q_*	Variable d'échelle de l'humidité spécifique de l'air	kg kg^{-1}
Q	Stockage de flux de chaleur entre un appareil de mesure et la surface	W m^{-2}
Q_B	Stockage de flux de chaleur dans la biomasse	W m^{-2}
Q_G	Stockage de flux de chaleur dans le sol	W m^{-2}
Q_H	Stockage de flux de chaleur sensible	W m^{-2}
Q_{LvE}	Stockage de flux de chaleur latente	W m^{-2}
Q_{veg}	Stockage de chaleur dans une composante d'un arbre	W
R	Ruissellement	mm
R_n	Rayonnement net	W m^{-2}
$R_{n,hor}$	Rayonnement net, plan horizontal	W m^{-2}
$R_{n,inc}$	Rayonnement net, plan incliné à 12° vers le nord-est	W m^{-2}
R_{Tq}	Coefficient de corrélation de température – humidité	-
S	Stockage d'eau dans et au-dessus du sol	mm
t	Temps	s
T	Température de l'air	K
T_s	Température du sol	K
T_{veg}	Température d'une composante d'un arbre	K
T_*	Variable d'échelle de la température de l'air	K
u	Vitesse du vent selon la direction cartésienne x	m s^{-1}
u_*	Vitesse de friction	m s^{-1}
U	Vitesse du vent totale	m s^{-1}
v	Vitesse du vent selon la direction cartésienne y	m s^{-1}
w	Vitesse du vent selon la direction cartésienne z	m s^{-1}
WD	Direction du vent	°
W_{LAS}	Fonction de poids du trajet du LAS	-
W_{OMS}	Fonction de poids du trajet du système combiné LAS – MWS	-

W_{MWS}	Fonction de poids du trajet du MWS	-
$x_{q,1}$	Premier coefficient empirique de la fonction de similarité de l'humidité	-
$x_{q,2}$	Deuxième coefficient empirique de la fonction de similarité de l'humidité	-
$x_{q,3}$	Troisième coefficient empirique de la fonction de similarité de l'humidité	-
$x_{q,4}$	Quatrième coefficient empirique de la fonction de similarité de l'humidité	-
$x_{T,1}$	Premier coefficient empirique de la fonction de similarité de la température	-
$x_{T,2}$	Deuxième coefficient empirique de la fonction de similarité de la température	-
$x_{T,3}$	Troisième coefficient empirique de la fonction de similarité de la température	-
$x_{T,4}$	Quatrième coefficient empirique de la fonction de similarité de la température	-
X	Variable exemple	[X]
y	Variable exemple dépendant du temps	[y]
z	Hauteur ou altitude	m
z_0	Longueur de rugosité	m
z_{0m}	Longueur de rugosité pour la quantité de mouvement de l'air	m
z_{0v}	Longueur de rugosité pour la vapeur d'eau	m
z_{ASL}	Hauteur de la couche de surface atmosphérique	m
z_{BL}	Hauteur de la couche limite atmosphérique	m
z_m	Hauteur de mesure	m
$z_{m,eff}$	Hauteur effective de mesure du scintillomètre	m
z_v	Hauteur de mesure de l'humidité de l'air	m
Z	Angle solaire zénithal	°
α	Albédo (= K_m / K_d)	-
δ	Écart spatial	m
Δ	Variation temporelle d'une variable	-
Δ_e	Pente de la tension de vapeur à saturation en fonction de la température	Pa K^{-1}
ε	Écart temporel	s
φ	Latitude	°
ϕ	Puissance évaporante de l'air	W m^{-2}

γ	Constante psychrométrique	Pa K^{-1}
κ	Constante de Von Kármán (= 0.41)	-
λ_{LAS}	Longueur d'onde du LAS (= 0.88 μm)	μm
λ_{MWS}	Longueur d'onde du MWS (= 1860 μm)	μm
η	Coefficient d'extinction du rayonnement dans la canopée	-
Ω	Période d'intégration de variances	min
ω	Période de moyenne mobile	s
θ	Contenu en eau volumétrique des 10 premiers cm de sol	$m^3\ m^{-3}$
ν_d	Fraction ouverte de la canopée en ligne avec le soleil	-
ν_s	Fraction ouverte de la canopée sur toute la photo hémisphérique	-
Ψ_m	Fonction de correction de stabilité pour la quantité de mouvement	-
ρ	Masse volumique de l'air humide	kg m^{-3}
$\sigma_{S\,S}$	Variance d'une intensité lumineuse mesurée avec un scintillomètre *S*	-
$\sigma_{LAS\,LAS}$	Variance logarithmique du signal normalisé du LAS	-
$\sigma_{LAS\,MWS}$	Covariance logarithmique des signaux normalisés du LAS et du MWS	-
$\sigma_{MWS\,MWS}$	Variance logarithmique du signal normalisé du MWS	-
σ_u^2	Variance de la vitesse du vent selon la direction cartésienne *x*	$m^2\ s^{-2}$
σ_v	Écart-type de la vitesse du vent perpendiculaire au vent dominant	m s^{-1}
σ_v^2	Variance de la vitesse du vent selon la direction cartésienne *y*	$m^2\ s^{-2}$
σ_w^2	Variance de la vitesse du vent selon la direction cartésienne *z*	$m^2\ s^{-2}$
τ	Transmittance de la canopée au rayonnement solaire (K_u / K_a)	-
$\tau^{\otimes}$	Transmittance de la canopée au rayonnement solaire diffus	-
$\tau^{\odot}$	Transmittance de la canopée au rayonnement solaire direct	-
ζ	Paramètre de stabilité (= ($z - d_0$) / L_{Ob})	-

Liste des abréviations

Abréviation	Signification
AMSL	Au-dessus du niveau moyen de la mer (« above mean sea level »)
ASL	Couche de surface atmosphérique (« atmospheric surface layer »)
BC	Méthode bichromatique (« bichromatic method »)
BEREV	Bassin versant du ruisseau des Eaux-Volées
BOREAS	« Boreal Ecosystem Atmosphere Study »
CDIAC	« Carbon Dioxide Information Analysis Center »
CLASS	Schéma de surface canadien (« Canadian Land Surface Scheme »)
CV	Coefficient de variation (moyenne / écart-ype)
DBH	Diamètre à hauteur de poitrine (« diameter at breast-height »)
DFIR	« Double-Fence Intercomparison Reference »
EC	Covariance des tourbillons (« eddy-covariance »)
ECMWF	« European Centre for Medium-range Weather Forecasts »
FFP	Modèle de prédiction de l'empreinte (« Flux Footprint Prediction »)
FRD	« Footprint radiation dissimilarity »
FRQNT	Fonds de recherche québécois – nature et technologies
FVD	« Footprint vegetation height dissimilarity »
GIÉC	Groupe intergouvernemental sur l'évolution du climat
GS	Saison de croissance (« Growing season »)
ICOS	« Integrated Carbon Observation System »
IPCC	« International Panel on Climate Change »

LAI	Indice de surface foliaire [m^2 m^{-2}] (« leaf area index »)
LAS	Scintillomètre optique (« Large-Aperture Scintillometer »)
LBA	« Large-scale Biosphere-atmosphere experiment in Amazonia »
LIDAR	« Light Imaging, Detection and Ranging »
LITFASS	« Lindenberg Inhomogeneous Terrain Fluxes between Atmosphere and Surface Study »
MELCC	Ministère de l'environnement et de la lutte aux changements climatiques du Québec
METRIC	« Mapping Evapo-Transpiration at high spatial Resolution with Internalized Calibration »
MODIS	« Moderate Resolution Imaging Spectroradiometer »
MWS	Scintillomètre à micro-ondes (« Micro-Wave Scintillometer »)
NECC	« Nordic Centre for Studies of Ecosystem Carbon Exchange »
NSERC	« Natural Science and Engineering Research Council of Canada »
OMS	Système de scintillomètres combinés (« Optical Micro-wave Scintillometer »)
PAI	Indice de surface foliaire incluant branches et troncs [m^2 m^{-2}] (« plant area index »)
PASL	Fraction du jour avec le faisceau du scintillomètre dans la couche de surface atmosphérique
PNEU	Fraction du jour sous conditions quasi-neutres
PRAD	Fraction de rayonnement par rapport au maximum journalier théorique
PSTA	Fraction du jour sous conditions stables
PUNS	Fraction du jour sous conditions instables
R^2	Coefficient de détermination
RMSE	Erreur-type
RX	Récepteur
TW	Méthode à deux longueurs d'ondes (« two-wavelength method »)

TX	Transmetteur
USCCC	« US-China Carbon Consortium »

C'est sous pression que
le carbone devient diamant.

- Prof. Louis J. Dubé

Remerciements

Avant toute chose, il est important pour moi de remercier mes directeurs et co-directeurs de thèse : Daniel Nadeau, Alain N. Rousseau et François Anctil. La relation étudiant-directeur peut être parfois houleuse, dit-on. Ce n'est certes pas mon expérience. Je retiendrai une relation harmonieuse avec ces trois personnes. Daniel est un mentor et un pédagogue hors pair, en plus d'être le motivateur parfait pour ma personnalité. Toutes ces opportunités offertes auront été des expériences inestimables, même si elles ont pu être acceptées à contrecœur parfois. La récompense pour du bon travail, c'est plus de travail. Merci d'avoir insisté pour me ramener à Québec, ce qui avait l'air d'un retour au confort a en fait changé ma vie. Je remercie Alain de continuer à me suivre de loin, d'apporter ses idées différentes, mais toujours très allumées. Je remercie finalement François pour son enthousiasme calme, sa confiance tranquille et pour être celui qui me lit le plus rapidement malgré qu'il est parmi les plus occupés. Je vous remercie les trois à la fois pour mes études graduées au complet, qui m'ont permis de voyager partout en Amérique du Nord et de rencontrer des dizaines de personnes formidables. Sans votre appui, c'eut été impossible.

Je dois ensuite remercier tous les collègues qui ont participé de près ou de loin à l'installation et la maintenance de tous ces appareils. Il y en a beaucoup, mais celle qui se démarque est sans contredit Annie-Claude Parent. Merci, Annie-Claude, de toujours faire passer en premier nos besoins de recherche, nos idées folles et farfelues (aller recharger une génératrice en quatre-roues au milieu de la nuit?). Tu te donnes tellement pour nos travaux, je n'imagine pas mon projet sans toi derrière. Je remercie aussi, dans une liste que j'espère complète : Patrick Pineault, Charles Villeneuve, Dany Crépault, Denis Jobin, Benjamin Bouchard, Sophie Robitaille, Jean-Pierre Tatchegnon Gbegan, Derek Jensen, Chaoxun Hang, Pascale Girard, Martin Pharand, Gabriel Hould Gosselin, Fabien Gaillard Blanca, Gonzalo Americano Leonardini Quelca, Bram Hadiwijaya, Achut Parajuli, Marco Alves, Laurie (Solution) Migneault, Carine Poncelet, Antoine Thiboult, Guillaume Frédéric Hazemann, Audrey Combes, Jonas Götte et Georg Lackner. La liste est longue, mais chacune de ces personnes a soulevé quelque chose de lourd pour que je puisse écrire cette thèse. Merci, merci, merci.

Un remerciement spécial aux membres de jury de cette thèse et des examens doctoraux en début de parcours : Monique Leclerc, Audrey Maheu, Peter Vanrolleghem, Brian Morse et Sylvain Jutras. Votre encadrement est nécessaire au processus de formation doctorale, et votre contribution volontaire est très appréciée. Je remercie également les coauteurs des articles scientifiques présentés dans cette thèse qui n'ont pas encore été nommés : Marie-Hélène Asselin, Richard Harvey, Keith N. Musselman, Alexei O. Perelet, Eric R. Pardyjak et Biljana Music. Vous avez tous contribué de différente façon à cette thèse, mais chacune de ces façons était absolument essentielle. Merci.

Ce doctorat a été mon emploi pendant presque 5 ans en incluant le séjour à Polytechnique Montréal. Il est nécessaire pour moi de remercier les organismes qui m'ont permis de vivre de ce travail en finançant mes recherches. Je remercie le Conseil de recherche en sciences naturelles et en génie du Canada (CRSNG), le Fonds de recherche du Québec – Nature et technologie (FRQNT), le consortium Ouranos, Environnement et Changement climatique Canada, CentrEau – Centre de recherche sur l'eau de l'Université Laval, la Faculté des études supérieures de l'Université Laval, et la Fondation de Polytechnique. Votre contribution permet de se concentrer sur la science sans soucis d'autre ordre.

En dehors de l'Université, je dois aussi remercier famille et amis pour leur support et leur intérêt dans mes recherches. Vos encouragements sont essentiels pour garder le niveau de motivation nécessaire aux études doctorales, et surtout pour oublier mon projet pendant de plus ou moins longues périodes. Je retiens particulièrement mes parents Pierre et Sylvie, ma sœur Karina et son conjoint Jérôme, avec une contribution non négligeable de mon filleul Léandre; mes beaux-parents Francine et Marcel, mon beau-frère Sylvain et ma belle-sœur Christiane et mes neveux Philippe et Pierre-Olivier; mes « frères » Bruno, Doun et Julien (repose en paix mon gars, je m'ennuie); les VIP à Québec, les planteurs et la gang du chalet. Le plein air, D&D, les fiestas, les chalets, sans ça, je ne serais jamais passé à travers.

La dernière personne que je remercie est la plus importante de toutes : ma fiancée Julie-Anne Pelletier-Bergeron. Le support qu'elle m'a apporté depuis notre rencontre est d'une valeur inestimable et difficile à mettre en mots. Elle a été ma fan #1 durant les moments glorieux, et ma lumière dans les moments sombres. Elle a relu mes textes, mes présentations, et mes formulaires. Dans notre jeune vie commune, elle est présente quand je le souhaite et s'efface quand le travail le commande. Je t'aime, et j'entame la suite de notre aventure avec un enthousiasme égal à mon amour pour toi.

Avant-propos

Cette thèse est basée sur trois articles scientifiques publiés ou soumis à des revues scientifiques de premiers plans. Chaque article forme un chapitre, et cette section les présente.

Le **premier chapitre** est calqué sur l'article :

Isabelle, P.-E., Nadeau, D. F., Asselin, M.-H., Harvey, R., Musselman, K. N., Rousseau, A. N., & Anctil, F. (2018). Solar radiation transmittance of a boreal balsam fir canopy: Spatiotemporal variability and impacts on growing season hydrology. *Agricultural and Forest Meteorology, 263*, 1–14. doi:10.1016/j.agrformet.2018.07.022.

Cet article a été soumis le 13 avril 2018, accepté par l'éditeur le 19 juillet 2018 et publié le 15 décembre 2018. La version présente dans cette thèse est reprise directement du manuscrit publié. Pour cet article, j'étais l'auteur principal : j'ai aidé au design expérimental et à la collecte de données, j'ai traité et analysé les données pour créer les résultats de l'article, j'ai écrit la vaste majorité du texte et j'ai appliqué les corrections suggérées par les réviseurs. Daniel Nadeau a dirigé les travaux scientifiques et a révisé le manuscrit en profondeur. Marie-Hélène Asselin (Polytechnique Montréal) a piloté la campagne de terrain à l'été 2016 et a révisé le manuscrit. Richard Harvey (Environnement et Changement climatique Canada) a aidé au paramétrage du modèle CLASS et a révisé le manuscrit. Keith N. Musselman (University of Colorado – Boulder) a aidé à l'analyse numérique des photos hémisphériques et a révisé le manuscrit. Alain N. Rousseau et François Anctil ont participé aux analyses et ont révisé le manuscrit.

Le **deuxième chapitre** provient de l'article :

Isabelle, P.-E., Nadeau, D. F., Anctil, F., Rousseau, A. N., Jutras, S., & Music, B. Impacts of high precipitation on the energy and water budgets of a humid boreal forest. Soumis à *Agricultural and Forest Meteorology*.

L'article a été initialement soumis le 12 avril 2019 et resoumis après des révisions le 12 août 2019. La version présentée dans cette thèse est directement celle qui a été resoumise. Je suis encore l'auteur principal de cet article : j'ai grandement assisté lors du design expérimental, de l'installation et de la collecte des données du site principal. J'ai effectué le traitement des données et les analyses, en plus d'acquérir et d'analyser les données publiques des autres sites. J'ai écrit le texte en entier. Daniel Nadeau a dirigé le déploiement des instruments à la forêt Montmorency, en plus de réviser le manuscrit avec grand soin. L'instrumentation a été installée grâce à une subvention du Conseil de recherche en sciences naturelles et en génie du Canada, dont la demande a été chapeautée par François Anctil, Daniel Nadeau, Sylvain Jutras et Biljana Music. François Anctil, Sylvain Jutras, Biljana Music et Alain N. Rousseau ont révisé le manuscrit dans son entièreté.

Le **troisième chapitre** se base sur l'article :

Isabelle, P.-E., Nadeau, D. F., Perelet, A. O., Pardyjak, E. R., Rousseau, A. N., & Anctil, F. Application and evaluation of a two-wavelength scintillometry system to a complex shallow boreal-forested valley. Soumis à *Boundary-Layer Meteorology.*

L'article a été initialement soumis le 13 mars 2019 et resoumis après des révisions majeures le 2 août 2019. La version présentée dans cette thèse est directement celle qui a été resoumise. Pour cet article, j'étais encore une fois l'auteur principal : j'ai conçu le design expérimental, j'ai installé et maintenu en marche les appareils spécialisés de hautes technologies, les scintillomètres, j'ai collecté, traité et analysé les données pour créer les résultats et j'ai écrit le texte en entier. Daniel F. Nadeau a dirigé les travaux scientifiques, a aidé sur le terrain et a révisé le manuscrit en profondeur. Alexei O. Perelet et Eric R. Pardyjak (University of Utah) m'ont formé à l'utilisation des scintillomètres et ils ont apporté leur expertise inestimable dans la révision de l'article, tant au niveau du traitement de données, de l'analyse et de la discussion qu'au niveau de la forme. Alain N. Rousseau et François Anctil ont révisé le manuscrit.

Notez que pour assurer la cohésion de la thèse, la nomenclature a été normalisée pour les trois articles (abréviations, symboles, variables, etc.). Le lecteur peut se référer aux listes en début de document à ce sujet.

Introduction générale

Une gestion efficace et durable de la ressource en eau est nécessaire dans notre société. Elle est évidemment essentielle à notre existence, mais elle devient de plus en plus un enjeu de sécurité des infrastructures et des populations. La base de données canadienne sur les catastrophes dénombre plus d'une soixantaine d'incidences de fortes précipitations causant des inondations graves dans les 10 dernières années (Sécurité publique Canada, 2019). Les rapports du Groupe intergouvernemental sur l'évolution du climat (GIEC) anticipent une augmentation de l'intensité et de la fréquence de tels épisodes désastreux dans le prochain siècle en raison des changements climatiques (IPCC, 2013). Conséquemment, il est primordial de générer des prévisions hydrologiques et météorologiques de qualité pour assurer la sécurité des populations québécoises et canadiennes. Les modèles hydrologiques et météorologiques permettant de construire ces prévisions se doivent donc d'être robustes et fiables, particulièrement dans un contexte de climat changeant.

Une part importante du fonctionnement de ces modèles est attribuable à leur capacité à bien reproduire les échanges d'eau et d'énergie entre la surface terrestre et l'atmosphère. L'évapotranspiration (E) est particulièrement névralgique, puisqu'elle est la principale source d'eau et d'énergie pour l'atmosphère (Brutsaert, 1982 ; 2005). Traditionnellement, E est modélisée à l'aide de formulations tenant compte de variables décrivant les conditions atmosphériques, *p. ex.* : la température de l'air (T), l'humidité de l'air (q), le rayonnement net (R_n) et la vitesse du vent (U). L'évolution de ces modèles est nécessairement tributaire d'une validation faite avec des données *in situ* de qualité et d'une compréhension accrue des processus physiques spécifiques à certains environnements particuliers. C'est d'autant plus crucial dans un contexte de climat changeant, puisque certains modèles simples de E peuvent mener à des projections très divergentes dans le futur (Lofgren et al., 2011 ; Hoerling et al., 2012 ; Seiller et Anctil, 2014). Néanmoins, ces incertitudes pourraient se résorber avec une modélisation dépendant d'une quantification adéquate du fractionnement de l'énergie solaire en ces différentes composantes pour une surface donnée, ce qu'on appelle le bilan d'énergie de surface.

Théorie : Bilan d'énergie

L'évapotranspiration est partie intégrante du bilan d'énergie de surface, puisque le changement de phase de l'eau (ou de la glace) vers la vapeur nécessite un intrant d'énergie qui sera relâchée lors de la condensation. Ainsi, comprendre les mécanismes physiques favorisant E demande de comprendre également le bilan d'énergie de surface. Tel que mentionné précédemment, celui-ci exprime le fractionnement de la principale source d'énergie à la surface, le rayonnement solaire, en diverses composantes souvent exprimées avec l'équation suivante et par la Figure 0.1 :

$$R_n = H + L_v E + G + \Delta Q \tag{0.1}$$

où R_n [W m^{-2}] est le flux d'énergie thermique par rayonnement net solaire; L_v [J kg^{-1}], la chaleur de vaporisation de l'eau; E [kg m^{-2} s^{-1}], le flux d'eau par évaporation; H [W m^{-2}], le flux de chaleur sensible; G [W m^{-2}], le flux de chaleur dans le sol; et ΔQ [W m-2], le taux de stockage de chaleur dans le volume de contrôle.

Le rayonnement net est aussi le résultat d'un bilan, décrit par l'équation suivante :

$$R_n = K_d - K_m + L_d - L_m \tag{0.2}$$

où K_d [W m^{-2}] est le rayonnement de courtes longueurs d'onde incident, soit le rayonnement solaire; K_m [W m^{-2}], le rayonnement de courtes longueurs d'onde ascendant, la réflexion par la surface, souvent définie comme αK_d où α est appelé l'albédo (rapport K_m / K_d); L_d [W m^{-2}], le rayonnement de longues longueurs d'onde incident émis par l'atmosphère; et L_m [W m^{-2}], le rayonnement de longues longueurs ascendant émis par la surface terrestre.

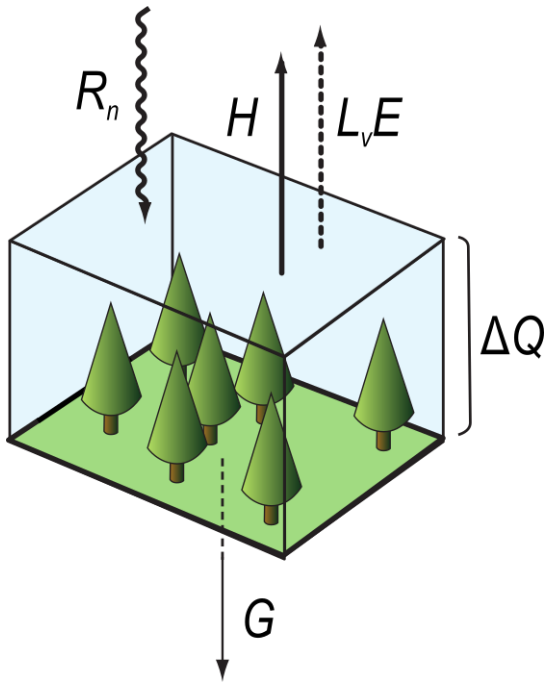

Figure 0.1 : Schéma du bilan d'énergie d'une surface végétalisée (gracieuseté d'Andreas Christen, University of Freiburg).

Pour les autres termes, H est le flux de chaleur transférée de la surface vers l'atmosphère ou inversement par convection naturelle et forcée; G est le flux de chaleur qui s'enfonce dans le sol ou qui provient de celui-ci par conduction; et ΔQ est un terme ajouté pour tenir compte du stockage d'énergie dans le volume de contrôle, dans l'air sous forme sensible (fluctuations de température) ΔQ_H et sous forme latente (fluctuations d'humidité) ΔQ_{LvE}, et dans toute fluctuation de température de la biomasse ΔQ_B. Finalement, L_vE est le flux de chaleur latente, soit le flux d'énergie emmagasinée dans l'eau lorsqu'elle se vaporise à la surface et monte dans

l'atmosphère. E est donc un lien entre le bilan d'énergie de surface et le bilan hydrique. Notez qu'on quantifie habituellement le partitionnement de l'énergie dans H et L_vE avec le rapport de Bowen ($Bo = H / L_vE$).

Traditionnellement, la mesure de E a souvent été déduite du bilan énergétique : L_vE étant le terme le plus difficile à mesurer directement, les chercheurs mesuraient tous les autres termes et L_vE devenait alors le terme résiduel dans l'équation 0.1 (Brutsaert, 1982). Cette approche est moins utilisée considérant la globalisation des mesures directes de E par l'approche de la covariance des tourbillons (Stull, 1988 ; Baldocchi et al., 2001 ; Burba, 2013), réputée comme la méthode la plus directe d'obtention des flux de chaleur turbulents (Itier et Brunet, 1996).

La covariance des tourbillons nécessite deux appareils : un anémomètre sonique, qui mesurera la vitesse du vent dans les trois directions cartésiennes; et un analyseur de gaz qui mesurera la concentration de vapeur d'eau dans l'air et la température de l'air. Ces deux appareils mesurent à une haute fréquence (*p. ex.* 20 Hz), et pour une période de moyenne choisie, on évalue les flux de chaleur sensible ou latente comme la covariance entre la vitesse du vent verticale et la température de l'air ou l'humidité de l'air, respectivement. Plusieurs corrections géométriques, atmosphériques et statistiques sont nécessaires (*p. ex.* voir aux sections 2.4.3 et 3.6.2.2). Cette méthode est devenue la référence dans le domaine, et a été déployée sur des centaines de sites dans le monde (Baldocchi et al., 2001; Burba, 2019).

Par contre, avec cette méthode de mesure directe, le bilan d'énergie n'est pas toujours équilibré : on mesure habituellement moins d'énergie par flux turbulents (H te L_vE) et flux de chaleur dans le sol que par rayonnement R_n (Foken, 2008). Plusieurs raisons peuvent expliquer ce phénomène : les incertitudes des appareils et de la méthode d'analyse causées par la non-stationnarité de l'écoulement (Mahrt, 1998), un déphasage entre les flux turbulents et les termes de stockage ΔQ (Leuning et al., 2012), l'hétérogénéité horizontale des surfaces instrumentées (Stoy et al., 2013), l'omission du transport par tourbillons stationnaires (Mahrt, 2010), et les processus d'échanges de chaleur ou d'humidité se produisant à des échelles spatiales et temporelles plus grandes que la zone de mesure de l'appareil, comme l'advection (Foken, 2008), entre autres. Ces incertitudes peuvent toutefois être corrigées assez efficacement (*p. ex.* Mauder et al., 2018), ce qui fait que la méthode est toujours utilisée globalement.

Contexte : Forêt boréale

Au Canada, la modélisation hydrologique et climatique se doit d'être efficace en milieu boréal, car cette zone couvre approximativement 60% du territoire, pour un total d'environ 6 millions de km^2 (Brandt, 2009). Plus particulièrement, le biome de la forêt boréale occupe la moitié de la zone boréale canadienne, et donc ~30% de la surface du pays. À ce titre, c'est le biome prévalant au Canada, alors qu'au monde, il couvre 14% de la surface terrestre et contient 30% des forêts mondiales (Brandt et al., 2013; Gauthier et al., 2015). De façon générale,

on peut dire que ce type d'écosystème occupe une part si grande de la surface terrestre qu'il affecte nécessairement la climatologie et l'hydrologie mondiale, étant donné ses importants échanges sol-atmosphère d'eau et de carbone.

Considérant son importance au Canada et dans le monde, un très grand nombre d'études portent sur ce type d'environnement. Entre autres, le Boreal Ecosystem-Atmosphere Study (BOREAS) est certainement un des plus vastes projets de recherche portant sur l'interaction sol-atmosphère dans la forêt boréale (Sellers et al., 1995; 1997). Ces études nous offrent un portrait global des bilans énergétique et hydrique dans la forêt boréale se retrouvant dans les plaines de l'Ouest canadien, au Manitoba et en Saskatchewan. Cette section relate également des études explorant le bilan d'énergie de la forêt boréale de l'est du Canada (McCaughey 1978a;b).

La forêt boréale est une des surfaces végétalisées absorbant le plus le rayonnement solaire arrivant au sol avec un albédo α d'environ 8% (McCaughey, 1978a; Sellers et al., 1995; 1997). Le rayonnement est majoritairement absorbé par la canopée, laissant peu d'énergie se rendre au sol (~17% du rayonnement total, Baldocchi et al., 1997). On considère ainsi qu'un faible pourcentage (~20%) des flux turbulents (H et L_vE) provient du sol sous la canopée (Sellers et al., 1995; Baldocchi et al., 1997). C'est aussi le cas en hiver étant donné que les conifères majoritaires en milieu boréal ne perdent pas leurs aiguilles et que le soleil est plus bas dans le ciel.

L'absorption intense d'énergie par la canopée crée de forts flux de chaleur sensible H qui vont généralement être largement supérieurs aux flux de chaleur latente L_vE (Bo ~ 1-10; Saugier et al., 1997; Sellers et al., 1997; Barr et al., 2001). C'est aussi le cas pour les espèces feuillues de la forêt boréale comme les trembles (*Populus tremuloides*) lorsque les feuilles sont absentes (Bo ~ 8; Blanken et al., 1997). Toutefois, à l'apparition des feuilles, E redevient dominante (Bo ~ 0,5; Oke, 1987; Blanken et al., 1997). Comme c'est le cas pour plusieurs autres surfaces végétalisées, les instruments ne mesurent pas un bilan d'énergie équilibré : on mesure environ 10% plus d'énergie disponible ($R_n - G - \Delta Q$) que par les flux turbulents ($H + L_vE$) (Baldocchi et al., 1997; Barr et al., 2006).

Au printemps, la faible E est causée par le gel du sol qui coupe l'accès des arbres à l'eau nécessaire pour la transpiration (Sellers et al., 1995; 1997). En été, Sellers et al. (1997) estiment que la faible profondeur racinaire des arbres et la composition du sol sous les racines créent une couche semi-imperméable sur laquelle l'eau ruisselle : le sol ne se charge donc pas en eau ce qui diminue la transpiration des arbres. Ces derniers sont aussi très réactifs aux temps plus secs et cessent la photosynthèse, et donc de transpirer, lorsque l'humidité de l'air est trop faible, ce qui survient souvent sur les plaines de l'Ouest canadien (Bailey et al., 1997). Même si ces conifères ne transpirent pas beaucoup d'eau, la présence de feuillus, même en proportion minoritaire, peut influencer grandement le bilan d'énergie régional (Barr et al., 2001).

De façon générale, les variables contrôlant *E* en forêt boréale durant l'été sont majoritairement l'humidité et la température de l'air (Sellers et al., 1995; 1997; McCaughey et al., 2006). L'humidité du sol n'aurait que peu d'impact (Sellers et al., 1995). L'âge des arbres affecte aussi *E* : les jeunes arbres peuvent transpirer beaucoup plus que les arbres matures (Amiro et al., 2006).

Malgré la vaste étendue de la littérature disponible sur l'hydrologie et le bilan d'énergie des forêts boréales, certaines lacunes demeurent. Peu de recherches ont été effectuées dans des terrains avec une topographie prononcée, car la méthode de la covariance des tourbillons est typiquement utilisée en terrain plat. Également, peu d'études ont porté sur les forêts de l'est du Canada qui reçoivent un nombre plus important de précipitations, un facteur certainement important pour *E*.

Problématique

Topographie

Les régions montagneuses ont une influence cruciale sur l'hydrologie mondiale en étant à la source de la plupart des bassins versants mondiaux (Brutsaert, 2005). Or, plusieurs études estiment que ces régions seront sujettes à des changements climatiques plus rapides en comparaison avec les régions à faible altitude adjacentes (Beniston & Rebetez, 1996; Williams et al., 1996; Giorgi et al., 1997). L'hydrologie des bassins versants comportant des régions montagneuses risque donc de subir des modifications importantes dans le futur.

La topographie a une influence majeure sur les composantes du bilan hydrologique comme la précipitation (Daly et al., 1994), la distribution de la neige (Walland & Simmonds, 1996; Essery, 2003a), la teneur en eau du sol (Zheng et al., 1996; Grant, 2004), le ruissellement (Haddeland et al., 2002) et également *E* (Kang et al., 2004). Celle-ci aurait tendance à diminuer avec l'altitude, mais la tendance n'est pas simplement linéaire puisqu'elle dépend de plusieurs facteurs (rayonnement, température de l'air, densité de végétation, etc.; El Maayar & Chen, 2006).

L'inclinaison d'une pente et son orientation ont une influence plus importante sur *E* que l'altitude puisque ces aspects dictent la quantité de rayonnement solaire atteignant la surface (Whiteman & Allwine, 1986; Fritschen & Qian, 1990; Olmo et al., 1999; Holst et al., 2005; Matzinger et al., 2003; McVicar et al., 2007; Aguilar et al., 2010) et que le rayonnement est le principal moteur de *E*. À ce titre, Rim (2009) rapporte que l'augmentation de l'inclinaison d'une pente est généralement accompagnée d'une baisse de *E*. Cette dernière conclusion est toutefois probablement fausse lorsque la pente est orientée vers le sud et donc beaucoup plus exposée au rayonnement solaire (Fritschen & Qian, 1990). Ces effets sont moins prononcés lors de la présence d'un couvert nuageux, puisque seul le rayonnement diffus se rend à la surface et que celui-ci est isotrope (Holst et al., 2005). Les effets sont par contre plus prononcés aux hautes latitudes (et donc en milieu boréal) puisque la hauteur du

soleil dans le ciel varie grandement dans l'année, changeant l'angle entre la surface et les rayons lumineux (Oke, 1987; Fritschen & Qian, 1990).

Malheureusement, les connaissances actuelles sur *E* dans les pentes sont limitées. Ceci est explicable par le fait que la méthode de la covariance des tourbillons a longtemps été considérée impossible à appliquer en terrain accidenté en raison de certaines hypothèses de base pour l'applicabilité de la méthode. En effet, la covariance des tourbillons suppose un sol plat pour que la moyenne du vent vertical soit nulle, que les fluctuations de la densité de l'air soient négligeables et qu'il n'y ait pas de convergence ou divergence de l'écoulement. Toutefois, un changement de paradigme est survenu depuis quelques années, et les mesures par covariance des tourbillons sont maintenant reconnues comme valides dans les pentes (Turnipseed et al., 2002; Hammerle et al., 2007; Hiller et al., 2008; Goulden et al., 2012; Nadeau et al., 2013b; Stiperski & Rotach 2016) à condition que des précautions spéciales soient prises dans l'installation des instruments et lors du traitement des données (Wilczak et al., 2001; Shimizu, 2015; Oldroyd et al., 2016; Stiperski & Rotach; 2016).

Il est d'abord important de s'assurer d'installer les instruments de mesure de façon parallèle à la pente. Cette façon de procéder réduit la distorsion de l'écoulement (Geissbühler et al., 2000; Christen et al., 2001; Oldroyd et al., 2016), offrant ainsi une meilleure qualité des données et une meilleure fermeture du bilan énergétique (Zitouna-Chebbi et al., 2012). L'alignement des instruments mesurant le rayonnement solaire doit aussi être parallèle à la pente pour obtenir des données de meilleure qualité (Fritschen & Qian, 1990; Holst et al., 2005) et un meilleur équilibre du bilan énergétique (Nadeau et al., 2013a; Serrano-Ortiz et al., 2016). En post-traitement, la correction de l'alignement de l'appareil de mesure par covariance des tourbillons doit être faite pour l'aligner sur des plans parallèles aux directions de vents dominants avec la méthode du « planar fit » spécifique à certains secteurs de vents dominants (Wilczak et al., 2001; Ono et al., 2008; Oldroyd et al., 2016).

Malgré ces avancées, une lacune importante dans la science demeure sur la connaissance du bilan d'énergie en milieu accidenté. Cette lacune est d'autant plus importante en forêt boréale, qu'elle soit dans l'Ouest canadien ou ailleurs.

Précipitation

Tel que mentionné plus haut, il est prévu que les changements climatiques occasionneront une augmentation de la fréquence et de l'intensité des événements de précipitations extrêmes. De façon générale, le principe théorique de Clausius-Clapeyron prévoit que le réchauffement attendu de l'air impliquera que l'atmosphère pourra contenir plus d'eau, et ainsi créer plus de précipitations, un résultat corroboré par les nombreuses études sur les changements climatiques (IPCC, 2013). Ce sera d'autant plus vrai pour les régions boréales, qui subiront un réchauffement plus substantiel (IPCC, 2013) : à ce titre, le nord du Québec devrait recevoir plus de

précipitations (Ouranos, 2015). Dans ce contexte, le futur de la forêt boréale est incertain : le réchauffement prévu pourrait augmenter la longueur de la saison de croissance et donc la productivité de la forêt (Kauppi et al., 2014; Schaphoff et al., 2016), mais encore faut-il que les précipitations puissent alimenter *E*, puisque les arbres ne peuvent croître sans une photosynthèse liée à *E* (Barber et al., 2000; Lloyd & Bunn, 2007; Walker et al., 2015). Il semble par ailleurs que les forêts boréales du Québec pourraient être ainsi nettement plus productives (D'Orangeville et al., 2016).

Les études du projet BOREAS sur le bilan d'énergie en forêt boréale se situent dans l'Ouest canadien, qui reçoit de faibles quantités de précipitations (509 mm a^{-1}, moyenne climatologique 1980-2010, station Thompson d'Environnement et Changement climatique Canada, disponible au http://climat.meteo.gc.ca). Ces quantités de précipitations sont nettement en deçà des quantités reçues dans l'est du Canada (*p. ex.* 1583 mm a^{-1}, moyenne climatologique 1980-2010 de la station Forêt Montmorency d'Environnement et Changement climatique Canada). Considérant que les précipitations globales risquent d'augmenter dans le futur, il est important de comprendre les effets de celles-ci sur *E* en forêt boréale, particulièrement dans un contexte humide peu étudié.

Certaines études de BOREAS ont toutefois observé les interactions entre précipitations et *E* : il semble que *E* augmente de façon importante après un épisode de pluie, mais pour une brève période : c'est l'eau contenue dans les premiers mm du sol et celle interceptée par les arbres qui s'évapore (Kelliher et al., 1998; Joiner et al., 1999). Les pins (*Pinus banksiana*) sont plus réactifs aux précipitations que les épinettes (*Picea mariana*), mais c'est possiblement causé par leur environnement de croissance (Barr et al., 2001). En effet, les pins poussent sur des sols plus perméables et donc plus secs, alors que les épinettes préfèrent les zones déjà humides : l'apport d'eau les affecte peu. Dans l'est du Canada, les sapins baumiers (*Abies balsamea*) se retrouvent entre ces deux extrêmes avec une dépendance à l'humidité du sol lorsque celle-ci descend sous ~30% (McCaughey, 1978b). Brümmer et al. (2012) décrit la variation de *E* annuelle en fonction de la précipitation annuelle comme une montée qui atteint un plateau à environ ~450 mm a^{-1} pour une précipitation annuelle de ~800 mm a^{-1}. Cependant, les sites en forêt boréale recensés dans leur étude ont des précipitations annuelles maximales de ~1000 mm a^{-1}, et aucune information n'est disponible pour des précipitations plus importantes.

En termes d'hydrologie de bassin versant, les sites de mesure de *E* en forêt boréale prévoient que la majorité de la précipitation annuelle retournera vers l'atmosphère via ce processus. Ainsi, les débits annuels sortants des bassins versants où se trouvent les sites BOREAS sont habituellement très faibles (Nijssen & Lettenmeier, 2002; Barr et al., 2012). Des résultats similaires ont été obtenus dans des bassins versants de Scandinavie (Ilvesniemi et al., 2010) et de Russie (Oltchev et al., 2002). Globalement, les informations disponibles sur l'effet des précipitations sur *E* sont plutôt éparses, et il y a un manque à gagner important dans les forêts boréales humides de l'est du Canada.

Échelle de mesure

Les modèles hydrologiques et météorologiques sont souvent caractérisés par une résolution spatiale grossière pour diminuer les temps et difficultés de calcul, spécialement sur un territoire aussi vaste que celui du Canada. En effet, la plus petite résolution spatiale utilisée dans des modèles météorologiques canadiens est de 2,5 km (Leroyer et al., 2011), et celle des modèles de prévision du National Weather Service (États-Unis) est de 12 km (Kleissl et al., 2009). Ces modèles calculent donc une valeur *E* pour chacune de leurs tuiles ayant la taille de 6,25 et 144 km^2, respectivement. Idéalement, la mesure de *E* servant à caler ces modèles devrait donc avoir une zone d'empreinte (zone où les mesures de *E* sont valides) de taille semblable. Il est également nécessaire de comprendre la variation de *E* à diverses échelles spatiales pour espérer faire des mises à l'échelle supérieure ou inférieure.

Dans cette thèse, trois échelles spatiales seront utilisées dans la description des zones d'empreinte des mesures. L'échelle ponctuelle s'applique au processus ayant cours sur des espaces de quelques mètres carrés. L'échelle locale décrit un espace plus grand de quelques hectares (1 ha = 10 000 m^2). L'échelle régionale, quant à elle, s'applique à un espace encore plus grand de quelques kilomètres carrés (1 km^2 = 1 000 000 m^2).

Les méthodes habituellement utilisées pour la mesure in situ de *E*, incluant la covariance des tourbillons, sont principalement valides pour une zone d'empreinte à l'échelle locale. C'est donc dire que la mesure de *E* est représentative d'une seule zone locale, sans informations sur les valeurs possibles de *E* à l'échelle ponctuelle. Or, les connaissances sur *E* à cette petite échelle et la comparaison avec l'échelle locale peuvent nécessairement aider à mettre les mesures en perspectives. De plus, la mesure de *E* par covariance des tourbillons est applicable sur une zone locale, mais peut différer largement pour une autre zone quelques kilomètres plus loin. Étant donné l'importante hétérogénéité de la zone boréale, où se succèdent les forêts de conifères, les milieux humides, les lacs et les sols nus, il est difficile de caractériser *E* à plus grande échelle. La solution évidente est de multiplier les montages expérimentaux sur un territoire, mais cette option est virtuellement impossible vu le coût élevé des instruments de mesure.

Une alternative est d'utiliser l'imagerie satellitaire pour obtenir *E* à une plus grande échelle spatiale (*p. ex.* Allen et al., 2007a,b). Pour ce faire, les images satellitaires sont utilisées pour obtenir le bilan radiatif de la surface observée en plus d'informations sur la végétation en présence. Divers modèles sont ensuite utilisés pour calculer chacun des termes du bilan énergétique et ensuite isoler *E*. Par exemple, les images satellitaires de MODIS (http://modis.gsfc.nasa.gov/) peuvent être utilisées pour obtenir *E* à une résolution de 1 km^2. Il est ensuite possible d'agglomérer ces données à une échelle plus grossière puisqu'elles sont obtenues pour l'ensemble d'un territoire. L'imagerie satellitaire est par contre peu utile dans un contexte opérationnel de petite échelle temporelle. En effet, les images de MODIS sont obtenues à une seule heure de la journée, qui peut ne pas être

représentative (Kleissl et al., 2009). Cette fréquence peut aussi diminuer si une couverture nuageuse est présente, puisque celle-ci bloque l'imagerie. De plus, l'obtention de *E* à partir des images satellitaires est indirecte (modélisée) et nécessite également un calage (Allen et al., 2007a) puisque *E* dépend de processus invisibles pour un satellite (vitesse du vent, turbulence, flottabilité, etc.). Ce calage est fait à partir de mesures in situ, renforçant le besoin pour une méthode d'acquisition de *E* à l'échelle régionale prise directement sur le terrain étudié.

Objectifs

Cette thèse a pour objectif large d'analyser le bilan d'énergie de surface en terrain accidenté d'une forêt boréale humide typique du nord-est de l'Amérique du Nord, la forêt Montmorency. L'intérêt de cette thèse est particulièrement localisé dans l'analyse des termes de ce bilan à diverses échelles spatiales. Trois chapitres répondent à trois objectifs spécifiques à ce sujet, et ces objectifs sont liés à une échelle spatiale de mesure précise. En premier lieu, nous désirons quantifier les impacts du fractionnement du rayonnement solaire par la canopée très hétérogène sur le bilan d'énergie à l'**échelle ponctuelle** (~m). Ensuite, nous comparons le bilan d'énergie pluriannuel à l'**échelle locale** (~ha) de la forêt étudiée à celui de 13 autres sites situés dans la forêt boréale mondiale. La forêt Montmorency est ainsi mise en perspective, et nous pouvons quantifier l'impact des fortes précipitations sur le bilan d'énergie local et sur le bilan d'eau du bassin versant. Finalement, nous utilisons un système de scintillomètres à deux longueurs d'onde pour comparer le bilan d'énergie de la forêt étudiée à l'échelle locale et à l'**échelle régionale** (~km2). Une réflexion sur les liens entre les différentes échelles spatiales est amenée par la suite.

1 Solar radiation transmittance of a boreal balsam fir canopy: Spatiotemporal variability and impacts on growing season hydrology

1.1 Résumé

Les canopées forestières agissent comme des barrières perméables entre l'atmosphère et le sol, réfléchissant et absorbant le rayonnement solaire. Dans la forêt boréale, le grand nombre de trouées et d'hétérogénéités complique davantage ces processus. Plusieurs études ont correctement mesuré et modélisé la transmittance du rayonnement solaire dans les canopées des forêts de l'ouest de l'Amérique du Nord et de la Scandinavie, mais peu se sont intéressées à celles de l'est de l'Amérique du Nord. En outre, la plupart de ces études ont évalué les effets de la transmittance du rayonnement solaire sur les propriétés énergétiques du manteau neigeux, mais peu se sont concentrés sur les impacts hydrologiques pendant la saison de croissance. Cet article aborde ce manque de connaissances en mesurant avec précision le rayonnement solaire sous-canopée dans une forêt juvénile de sapins baumiers située dans la forêt de Montmorency, Québec, Canada. À la fin de l'été et au début de l'automne 2016, vingt (20) stations sous-canopée ont été déployées dans une grille de 200 m sur 150 m autour d'une tour à flux mesurant le rayonnement au-dessus de la canopée et l'évapotranspiration par covariance des tourbillons. Les résultats montrent que la forêt hétérogène présente une variabilité spatiale substantielle de transmittance, avec des moyennes saisonnières spécifiques à chaque site comprises entre 0,07 et 0,69. Les trouées dans la canopée, de taille relative par rapport à la hauteur de l'arbre (H) entre 0,1H et H, avaient une influence temporelle sur la transmittance du rayonnement solaire dans les trouées de la canopée à l'échelle horaire, mais n'influencent pas les tendances saisonnières. Ceci est attribué à la présence très fréquente de nuages au site, qui rend le rayonnement solaire principalement diffus. En conséquence, une loi d'extinction de Beer-Lambert s'est révélée adéquate pour modéliser la transmittance spécifique à un site ou moyennée spatialement sur une base saisonnière. Nous complémentons les observations en modélisant les bilans d'humidité de la canopée et du sol aux 20 sites à l'aide du « Canadian Land Surface Scheme » (CLASS). Les résultats de la modélisation révèlent la tendance suivante: une végétation plus dense (moins dense) conduit à plus (moins) d'évapotranspiration, car il y a plus (moins) d'évaporation des précipitations interceptées et plus (moins) de transpiration, mais moins (plus) d'évaporation au sol. Pendant les périodes plus sèches, cette dernière tendance conduit à des conditions de sol plus humides pour une végétation plus dense. Ces résultats de modélisation sur la sensibilité à la densité de la végétation, bien qu'informatifs, doivent encore être confirmés par des observations.

1.2 Abstract

Forest canopies act as permeable barriers between the atmosphere and the ground, reflecting and absorbing solar radiation. In the boreal forest, the large number of gaps and heterogeneities further complicates these processes. Several studies have adequately measured and modeled the transmittance of solar radiation through forest canopies in western North America and Scandinavia, but few have addressed those of Eastern North America. Furthermore, most of these studies have assessed the effects of solar radiation transmittance on snowpack energetics, but few have focused on the hydrological impacts during the growing season. This paper addresses this knowledge gap with precise measurements of sub-canopy solar radiation in a juvenile balsam fir forest located in the Montmorency Forest, Quebec, Canada. Twenty (20) sub-canopy stations were deployed in a 200 m by 150 m gridded box around a flux tower measuring above canopy radiation and eddy covariance fluxes during late summer and early fall 2016. Results show that the heterogeneous forest has substantial spatial variability of transmittance, with site-specific seasonal averages ranging between 0.07 and 0.69. Canopy gaps of size relative to tree height (H) between $0.1H$ and H had a temporal influence on solar radiation transmittance in canopy gaps at the sub-daily scale, but do not influence seasonal trends. This is attributed to very frequent cloudiness at the site, which renders the solar radiation mostly diffuse. As a result, a Beer-Lambert extinction law proved adequate at modeling site-specific or spatially averaged transmittance on a seasonal basis. We complement the observations by modeling canopy and soil moisture balances at 20 sites using the Canadian Land Surface Scheme (CLASS). The modeling results exhibit the following trend: a thicker (thinner) vegetation leads to more (less) evapotranspiration, because there is more (less) evaporation of intercepted precipitation and more (less) transpiration, but less (more) ground evaporation. During drier periods, the latter leads to wetter soil conditions for the thicker vegetation. These modeling results of sensitivity to vegetation density, while informative, still need to be confirmed with observations.

1.3 Introduction

Forest canopies have intricate relationships with incoming solar radiation K and precipitation P, acting as a permeable barrier between the atmosphere and the ground. Canopies reflect a proportion of the solar radiation back to the atmosphere, while the rest is either absorbed or transmitted to the ground. The absorbed radiative energy flux activates photosynthesis (Sellers, 1985; Berbigier and Bonnefond, 1995), transpiration (Sellers, 1985; Berbigier and Bonnefond, 1995; Pieruschka et al., 2010) and changes in canopy temperatures that in turn create substantial turbulent transport (Bourque and Arp, 1994; Kellomäki and Wang, 1999) and longwave radiation emissions (Sicart et al., 2004; Pomeroy et al., 2009), along with other processes. Canopies also intercept a fraction of the precipitation before it may reach the ground (Hedstrom and Pomeroy, 1998; Huber and Iroumé, 2001; Storck et al., 2002), part of which is returned to the atmosphere by evaporation (Lundberg et al., 1997; Lundberg and Halldin, 2001; Lundberg and Koivusalo, 2003; Pypker et al., 2005; Toba and Ohta,

2005) or sublimation (Pomeroy et al., 1998; Parviainen et al., 2000; Essery et al., 2003b; Gelfan et al., 2004; Montesi et al., 2004). These water fluxes are also linked to the absorbed solar radiation and resulting canopy temperatures (Asdak et al., 1998; Klaassen et al., 1998; Toba and Ohta, 2005; Molotch et al., 2007). The transmitted fraction of solar radiation plays a crucial role in near-ground plant regeneration processes (Aubin et al., 2000; Montgomery and Chazdon, 2002; Ricard et al., 2003; Balandier et al., 2006), soil temperature dynamics (Breshears et al., 1998; Ritter et al., 2005), and snow energetic (Hardy et al., 2004; Talbot et al., 2006; Tribbeck et al., 2006; Ellis and Pomeroy, 2007; Musselman et al., 2012a,b; Gouttevin et al., 2015).

In the conifer forests of the circumpolar boreal biome, these barrier effects are magnified by the constant influence of a dominant evergreen vegetation. Compared to deciduous species, albedo is lower all year long (Wang, 2005), implying that much of the available energy is absorbed. The needleleaf canopy interception of solar radiation (Reid et al., 2014) and precipitation (Storck et al., 2002) is also higher than that of deciduous species in winter. The boreal forest is characterized by numerous gaps (Kneeshaw and Bergeron, 1998) and large-scale heterogeneities, including those created by anthropogenic disturbances (Gauthier et al., 2015). These gaps directly affect large-scale precipitation interception (Koivusalo and Kokkonen, 2002) and solar radiation (Hardy et al., 2004; Lawler and Link, 2011; Musselman et al., 2015), net radiation (Seyednasrollah et al., 2013), and turbulent exchanges (Wharton et al., 2017) with impacts on the land surface energy and water balance. As this biome contains 30% of the world's forests (Brandt et al., 2013) and sequesters 20% of the global forest carbon (Pan et al., 2011), a proper assessment of the partitioning of non-reflected solar radiation is crucial to the modelling of the thermal energy balance of the land surface.

This study focuses on canopy transmittance of solar radiation, defined as:

$$\tau = \frac{K_u}{K_a} \tag{1.1}$$

where K_u [W m^{-2}] is the under-canopy solar radiation and K_a [W m^{-2}] is the above-canopy solar radiation. In the literature, τ has been identified as a necessary parameter of models focusing on larger-scale processes such as land surface schemes (*e.g.* Verseghy et al., 1993) or hydrological models (*e.g.* Wigmosta et al., 1994; Gouttevin et al., 2015). Even if some more detailed estimation methods of τ are available (*e.g.* Zhao and Qualls, 2005; Mottus and Sulev, 2006), their computational needs render them impractical, leading to the common use of simpler options. Indeed, the most familiar formulation used to estimate τ is an adapted version of Beer-Lambert law for homogeneous medium (Monsi and Saeki, 1953), as follows:

$$\tau = \exp\left(-\eta \mathrm{LAI}\right) \tag{1.2}$$

where η [–] is an extinction coefficient usually dependent on solar elevation and leaf angle distribution and LAI [m^2 m^{-2}] is the leaf area index of the canopy. The general definition of LAI is "the total one-sided area of leaf tissue per unit ground surface area" (Watson, 1947; Breda, 2003). This definition only includes the leaf portion of the canopy, excluding branches, trunks and other obstacles blocking radiation. For this reason, most studies and models use plant area index (PAI) in Equation 1.2 to characterize the canopy-solar radiation interaction (Hardy et al., 2004; Musselman et al., 2012a; Reid et al., 2014).

The simplicity of the Beer-Lambert model makes it popular, but researchers must exercise caution at smaller spatiotemporal scales. τ is known to vary as a function of solar elevation, cloud cover, and canopy architecture (Hardy et al., 2004; Musselman et al., 2012b). Considering that the latter is largely discontinuous in boreal forests, most studies note that the Beer-Lambert formulation falls outside its range of applicability at the sub-daily timescale (Reifsnyder et al., 1971; Li et al., 1995; Ni et al., 1997; Nijssen and Lettenmaier, 1999; Yang et al., 2001). Some more recent models attempt to account for the precise spatiotemporal variation of the canopy elements interfering with solar radiation, with great success (Musselman et al., 2012a, 2013; Reid et al., 2014). Their methods still need to be evaluated in a diversity of environments.

Of the aforementioned studies on solar radiation transmittance, few compare modeling results with direct and precise observations under boreal or montane conifer canopies (Ni et al., 1997; Hardy et al., 2004; Ellis and Pomeroy, 2007; Musselman et al., 2012a,b, 2015; Reid et al., 2014). They are located in various environments of western North America and Scandinavia, but not in eastern North American forests, which host a different type of vegetation. Additionally, all of them focused on the influence of τ on snowpack energy accumulation and melt, a topic of tremendous relevance for the hydrology of boreal regions. Even if snowmelt is often the largest source of recharge of aquifers and surface water in the circumpolar boreal biome, the snow-free period still drives the global carbon and water cycles. Nevertheless, to our knowledge there have not been any studies aimed at quantifying the influence of τ on snow-free hydrology; that is during the growing season up to early fall when photosynthesis starts to decline.

This study characterizes the transmittance of solar radiation through a sparse juvenile balsam fir canopy typical of the southern boreal regions of eastern Canada. We are specifically interested in: (i) quantifying the spatiotemporal variability of solar radiation transmittance, and (ii) assessing the impacts of that variability on the growing season hydrology of the forest. The results are based on a three-month field campaign measuring solar radiation transmittance at 20 locations, complemented by land surface modeling.

1.4 Materials

This study was conducted in the Montmorency Forest (47°17'18"N; 71°10'05.4"W), located 80 km north of Quebec City, Canada, in the Laurentian Mountains. The field site lies within a 1.2-km^2 experimental watershed, part of the "Bassin Expérimental du Ruisseau des Eaux-Volées" (BEREV) (Lavigne, 2007; Tremblay et al., 2008, 2009; Noël et al., 2014). The BEREV has a mean altitude of 750 m above mean sea level (AMSL) with hills reaching 1000 m AMSL. The vicinity of the experimental setup is on a 12° slope facing northeast. The vegetation of the watershed is mostly composed of balsam fir (*Abies balsamea* (L.) Mill) mixed with white birch (*Betula papyrifera* Marsh) and white spruce (*Picea glauca* (Moench) Voss) (Lavigne, 2007; Tremblay et al., 2008, 2009). These trees reach heights between 4-8 m around the experimental setup and are classified as "juvenile", a result of natural regeneration following the logging of 85% of the trees in 1993. The region is dominated by a continental climate with a short and cool growing season and significant precipitation all year round. A mean annual temperature of 0.5 °C and a mean annual precipitation of 1583 mm (40% as snow) was observed over the period of 1981–2010 by Environment and Climate Change Canada (Station "Foret Montmorency", available at: http://climat.meteo.gc.ca/historical_data/search_historic_data_f.html).

1.4.1 Irradiance and complementary measurements

A 15-m flux tower has been in operation since the autumn of 2015 to measure surface energy budget components and other relevant meteorological variables in the watershed (see Figure 1.1). Above-canopy shortwave (solar) and longwave, downward and upward radiation components are measured with two net radiometers (CNR4, Kipp and Zonen, The Netherlands) installed at 15 and 10 m above the surface. Above-canopy radiation was also measured at a complementary flux tower located 1.28 km to the southeast. These devices are equipped with a ventilating and heating unit (CNF4, Kipp and Zonen, The Netherlands) to minimize measurement errors following dew deposition.

Since no measurements of the diffuse fraction of solar radiation f_d were available, it was estimated following Skartveit et al. (1998). f_d is defined as $K_a{\otimes}$ / K_a, where $K_a{\otimes}$ is the solar radiation classified as diffuse. The Skartveit et al. (1998) model was tuned with 32 years of data collected in Bergen, Norway (60°23'28.68"N; 5°19'19.56"E). It calculates the clearness index of the sky by dividing measured solar radiation with theoretical values from Whiteman and Allwine (1986) at specific elevation angle and ground slope and aspect. It also evaluates the presence of intermittent clouds by looking at the changes in clearness indexes of subsequent timesteps.

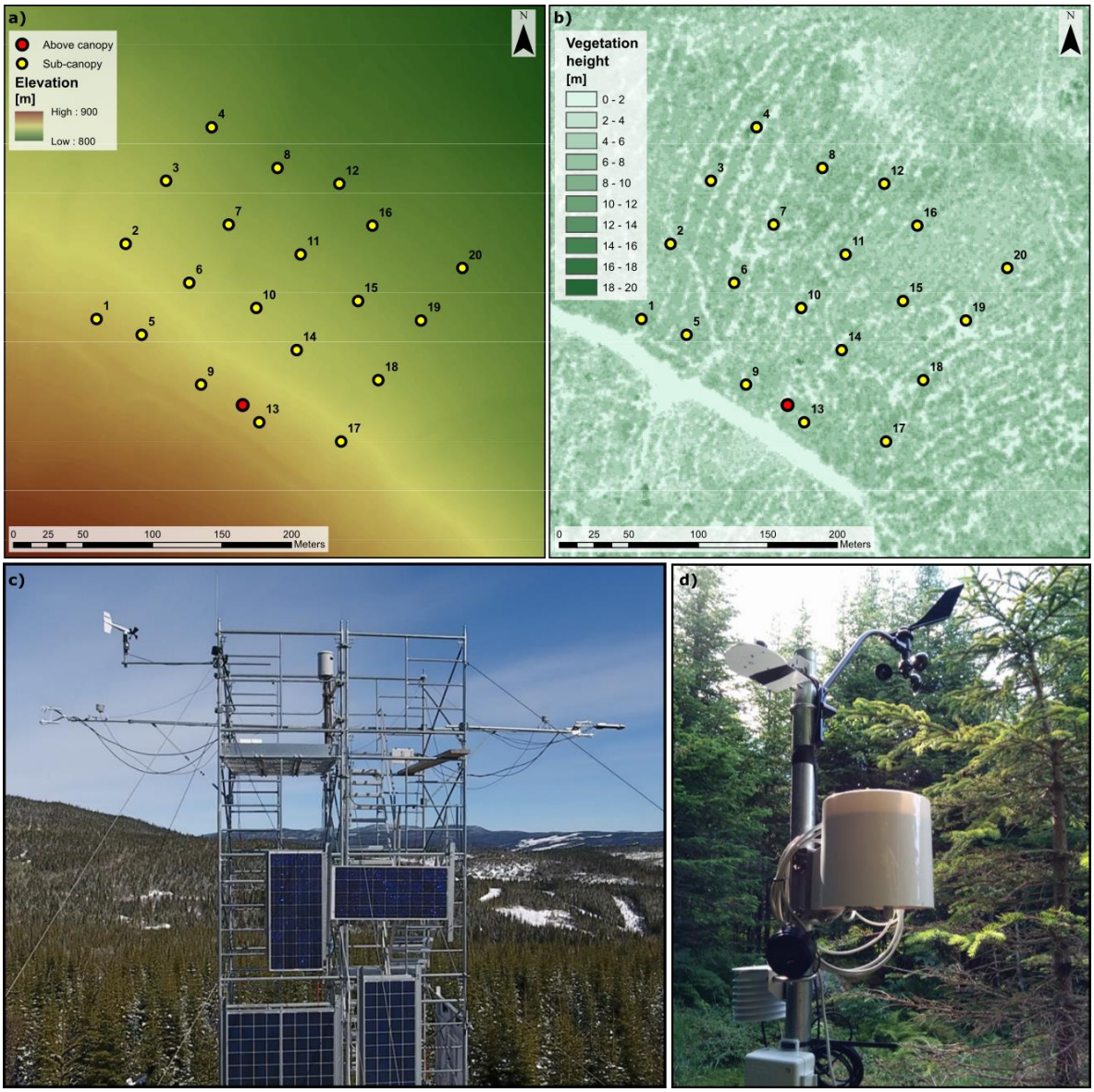

Figure 1.1: (a) Location of sub-canopy and above canopy stations, with topography around the stations; and (b) vegetation height around the stations; (c) above canopy flux tower (Source: La Géofabrique); (d) sub-canopy station 4. Topography and vegetation height are computed from LIDAR surveys (Source: Ministère Forêts, Faune et Parcs du Québec).

Sub-canopy solar radiation was measured with 20 silicon photocell pyranometers (PYR, Decagon Devices, USA) mounted 2 m above the ground (see Figure 1.1d). They were deployed in a 150 m by 200 m gridded box, each grid cell roughly 2500 m^2 located in the vicinity of the flux tower (Figure 1.1a and b). Silicon-cell pyranometers are sensitive to radiation in the range 400-1100 nm, and hence were calibrated to the full spectrum of shortwave radiation (300-2500 nm) (Ross and Sulev, 2000). The calibration method is described in Section 1.5.1.2. The pyranometers were operational between July 12 and September 23, 2016, defining our study period. All radiometers and pyranometers were mounted parallel to the 12° topographical slope for energy budget considerations (Serrano-Ortiz et al., 2016; Wohlfahrt et al., 2016).

The 15-m flux tower is also equipped with two eddy covariance systems (IRGASON, Campbell Scientific, USA) to measure sensible and latent heat fluxes, the latter being used to obtain evapotranspiration. The two systems are facing opposite directions (northwest and southeast), such that the combination of both time series ensured an optimal quality of fluxes, avoiding interference of the wind by the devices and masts. The sensors were mounted parallel to the 12° slope, as recommended to reduce flow distortion (Geissbühler et al., 2000; Oldroyd et al., 2016). Traditionally, eddy covariance measurements are done on flat homogeneous terrain. However, studies have deemed it to be applicable on sloped terrain provided a proper sensor alignment (Turnipseed et al., 2002; Hammerle et al., 2007; Hiller et al., 2008; Goulden et al., 2012; Nadeau et al., 2012; Stiperski and Rotach, 2016).

Fluxes were computed using EddyPro ®, version 6.0 (LI-COR Biosciences, USA). Data processing followed a standard Fluxnet procedure, aside from the coordinate rotation that used sector-wise planar fit (Wilczak et al., 2001), a method recommended for flux measurement on slopes (Ono et al., 2008; Oldroyd et al., 2016). The statistical tests described in Vickers and Mahrt (1997) were used to inspect the quality of raw turbulence data. Data segments with poor flux quality according to the 0-1-2 criteria described in Mauder and Foken (2011) were rejected. Gap filling was performed following the recommendations of Moffat et al. (2007): small gaps were filled by linear interpolation and large gaps were filled using marginal distribution sampling as described in Reichstein et al. (2005). Measurement errors were evaluated using the random uncertainty method of Finkelstein and Sims (2001). Storage of sensible and latent heat fluxes in the air between the ground and the eddy covariance setup were evaluated using a vertical profile of four temperature/humidity shielded probes (HC2S3 and HMP45C, Campbell Scientific, USA) following the method of Aubinet et al. (2001). The probes were installed at height 3.29, 5.68, 10.77 and 14.96 m above ground. The setup also featured three point measurements of the soil volumetric water content (CS650, Campbell Scientific, USA), with sensors installed vertically at 5 cm below the surface.

1.4.2 Hemispherical photography

Hemispherical photographs were taken to assess the extent of the vegetation cover above each sub-canopy pyranometer (see Figure 1.2). Photographs were taken using a DMC-LX5 camera (Panasonic, Japan) equipped with a fisheye lens and both devices were mounted on a self-leveler and north-finder MidOMount 10 MP (Regent Instruments, Canada). For each picture, the camera was positioned at a 1.4-m height and at a 1-m distance south of the pyranometer. Photographs were taken on two overcast days (July 27 and August 12, 2016), as recommended by the manufacturer, to better discern sky and canopy pixels.

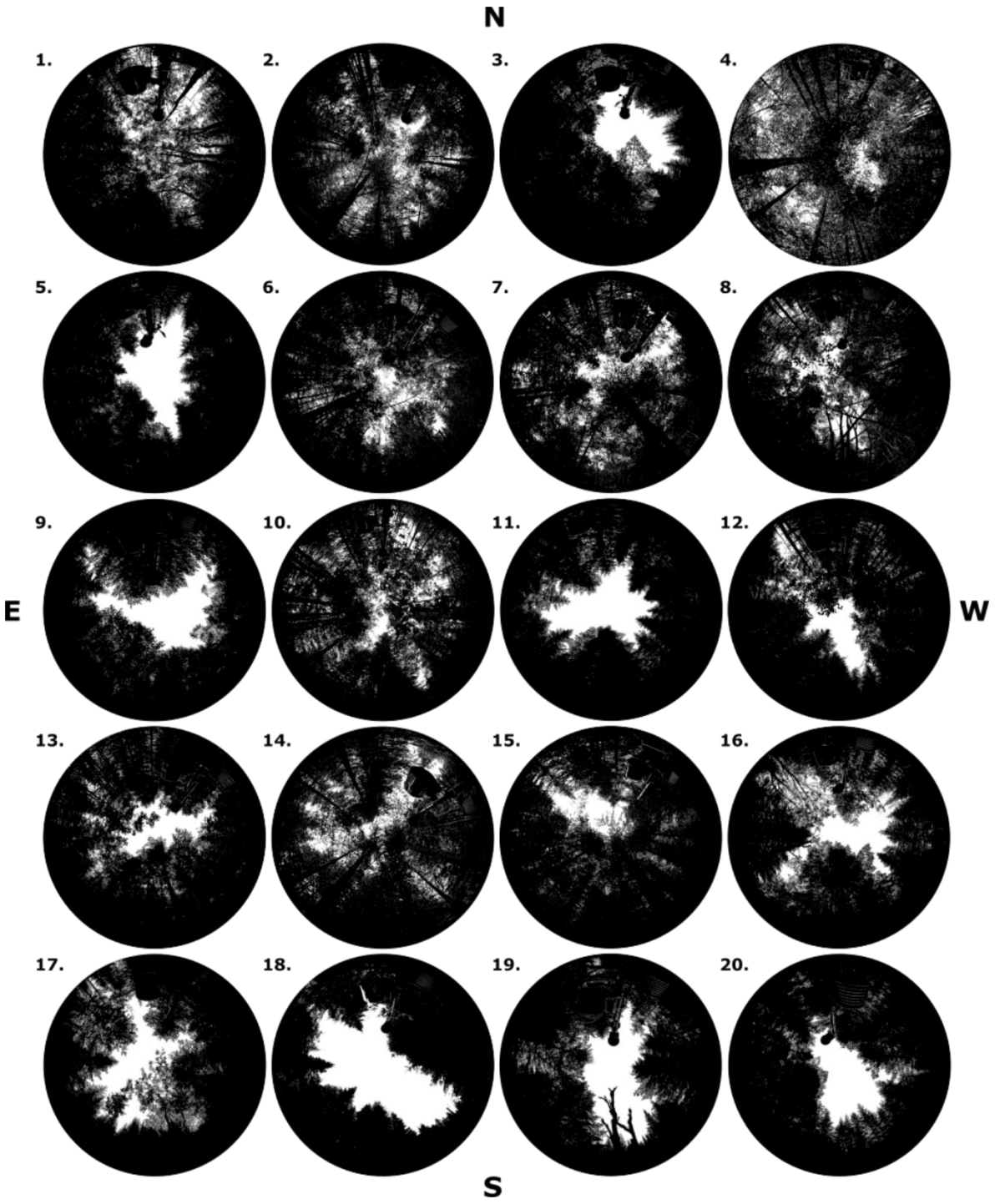

Figure 1.2: Hemispherical photographs taken at each sub-canopy station. Cardinal directions are shown on the picture, with geographic north on top.

Pixel classification was performed using the WinSCANOPY™ software (version 2016a, Regent Instruments, Canada). The 20 photographs are reproduced in Figure 1.2, with pixels classified as sky (white) or canopy

(black), classified with their grey levels. Automated thresholds of grey were used as a first approximation and carefully adjusted afterwards.

The black and white hemispherical photographs were next characterized with the automated image analysis model developed by Musselman et al. (2012a), to obtain gap fraction for the whole image and for a hemispherical 1° grid of 360 × 90 = 32, 400 tiles. This grid allowed for the calculation of the total gap fraction of the hemispherical photograph v_s and of the gap fraction in front of the solar disk on the photograph v_d. To accurately calculate the solar disk position in the sky, the method of Reda and Andreas (2004) was used. The precision of the method (± 0.0003°) is more than adequate to capture the angular velocity of the sun (≈ 0.25° min^{-1}) on a hemiphoto with a 1° resolution.

Note that a slight error is induced in the gap fraction values, as the camera was not located directly at the pyranometers positions. This error is negligible for the total hemisphere gap fraction, but can become substantial on the 1° tiles, especially when the intent is to track the sun position on the photographs. To overcome this, the center of the photographs was relocated under the pyranometer prior to calculations of v_d.

1.4.3 Energy budget model: Canadian Land Surface Scheme (CLASS)

The Canadian Land Surface Scheme (CLASS; Verseghy (1991, 2000) is a land surface model used to simulate heat and moisture exchanges between the surface and the atmosphere within global and regional climate models, thus acting as their lower boundary condition. In particular, it has been extensively used to study the surface energy and water budget in Canada for the last 25 years (Bellisario et al., 2000; Comer et al., 2000; Verseghy et al., 2000; Wang et al., 2002; Kothavala et al., 2005; Morais et al., 2015). CLASS separately computes the water and energy budgets of the soil, snowpack and of a single-layer canopy. As a consequence, both above-canopy and below-canopy components are treated, and the below-canopy component is considered to be bare soil and/or snowpack. In addition to being coupled to climate models, it can also be used in a single-column uncoupled mode, which is the one used in this study.

CLASS requires seven input variables: (i) downwelling solar radiation K_a; (ii) downwelling longwave radiation; (iii) surface air pressure; (iv) air temperature; (v) specific humidity; (vi) wind speed; and (vii) total precipitation P. Note that air temperature, specific humidity and wind speed should all be measured at a reference height above the canopy. In this study, CLASS is forced with downwelling solar radiation measured perpendicular to the 12° slope, to be consistent with the measurements of evapotranspiration and sub-canopy solar radiation.

Above-canopy sensible and latent heat fluxes are modeled as the sum of transfers from ground/canopy and above-canopy air. A bulk-transfer aerodynamic approach is used with gradients of temperature and humidity (for sensible and latent heat fluxes, respectively) between ground/canopy and above-canopy air. Stomatal resistance

has a user-set unstressed minimal value while the stressed value is calculated using solar radiation, vapor pressure deficit, soil moisture and canopy temperature. Precipitation is either intercepted by the canopy or directly transferred to the ground depending on a canopy-dependent sky view factor. Temperature of the ground surface, snowpack surface, and canopy "leaf" surface are obtained by an iterative solution of the energy budgets for each domain. More details are available in Verseghy (1991, 2000). Note that the presence of a 12° slope at the site does not affect CLASS in its single-column version. As turbulence flux calculations do not depend on gravity, forcing CLASS with slope-normal radiation provides turbulent fluxes in the same reference plane as the measured values.

CLASS computes canopy transmittance of the direct ($\odot$ superscript) solar radiation $\tau^{\odot}$ using a classical Beer-Lambert law formulation as in Equation 1.2 (Verseghy et al., 1993). The model uses PAI as a parameter to characterize vegetation. In CLASS, the extinction coefficient η is defined as:

$$\eta = \frac{0.3}{\cos Z} \tag{1.3}$$

where Z [°] is the solar zenith angle and 0.3 is a coefficient specific to conifers. For this study, since above- and sub-canopy radiation were measured parallel to the 12° northeast slope, and since CLASS was forced with slope-normal radiation, the solar zenith angle was geometrically adjusted for that reference plane.

Diffuse ($\otimes$ superscript) solar radiation transmittance $\tau^{\otimes}$ is computed by integrating the "standard overcast" distribution over the whole hemisphere using the simple weighting of three 30° zenith angle bins proposed by Goudriaan (1988):

$$\tau^{\otimes} = 0.308\tau^{\odot}\left(Z = 15°\right) + 0.514\tau^{\odot}\left(Z = 45°\right) + 0.178\tau^{\odot}\left(Z = 75°\right) \tag{1.4}$$

where the right-hand side represents $\tau^{\odot}$ calculated at zenith angle 15°, 45° and 75° weighted by the coefficients 0.308, 0.514 and 0.178, respectively.

In the single-column CLASS version, the diffuse fraction f_d is 1.0 during precipitation events and otherwise varies linearly as a function of the solar zenith angle (0.1 at the zenith and 1.0 at the horizon).

In addition to the energy budget outputs, CLASS also prognostically models the temperature and soil moisture content of the ground; temperature, water content and albedo of the snowpack; temperature of the canopy and intercepted precipitation mass, to name a few. CLASS typically runs at a 15- or 30-min timesteps but outputs may be aggregated to daily values.

1.5 Method

1.5.1 Irradiance processing

1.5.1.1 Above canopy

A rigorous filtering procedure was applied to above-canopy measurements. Unrealistic values of downwelling solar radiation were flagged, by comparison with values computed with the theoretical function of Whiteman and Allwine (1986), and then removed.

The filtered Ka series was assumed to have the best data quality, but complete solar radiation time series are required to run CLASS. Gap-filling was thus performed using the data from a complementary flux tower located 1.28 km to the southeast. Note that as the sensor at this location was installed horizontally, the data was corrected to a 12° northeast slope using Matzinger et al. (2003) procedure. This gap-filling procedure alone filled in 99.5% of the time series. The last few remaining gaps were filled in by linear interpolation. Note that these gap-filled time series are strictly used to run the CLASS model; the ensuing analyses only use periods when above-canopy solar radiation measurements are optimal.

1.5.1.2 Sub-canopy

Silicon-cell pyranometers had to be calibrated to the full range of the visible spectrum. As the optical properties of the canopy can substantially modify the spectral distribution of incoming shortwave radiation, the factory calibration of the sub-canopy pyranometers might cause errors in the measurements (Ross and Sulev, 2000). To prevent this, calibration was performed next to a recently factory-calibrated CNR4, both devices located below canopy, during a full week. This calibration procedure is similar to that used in a previous sub-canopy study (Tymen et al., 2017). A calibration coefficient of 1.12 was derived and applied to the original sub-canopy measurements. Once this correction was applied, the silicon-cell pyranometer measurements were highly correlated and accurate compared with the CNR4 measurements (R^2 = 0.91, root mean squared error RMSE = 4.7 W m^{-2}).

Again, strict filtering procedures were implemented on the dataset to ensure optimal data quality. Instances where $K_u > K_a$ were removed. This happened no more than 5% of the time at each station. Considering that both the above-canopy and sub-canopy devices have a 5% measurement uncertainty, these results are satisfying.

1.5.2 Determination of PAI

Site-specific PAI is generally estimated indirectly with optical methods that measure solar radiation under the canopy or that measure gap fraction of the canopy (Gower et al., 1999; Breda, 2003; Jonckheere et al., 2004). Both methods are inversions of the Beer-Lambert extinction law, but the former assumes a random canopy with

small leaves (needles) relative to the whole canopy size. With the latter method, the concept of leaf-angle distribution adds complexity to the extinction coefficient η (Van Gardingen et al., 1999; Breda, 2003). A version of each method was tested in this study.

Since measurements of τ were available, PAI was estimated by inverting Equation 1.2 – 1.4. This leads to a PAI value for each timestep that can be subsequently averaged over a defined period. In this case, a single PAI value was calculated. This simplification is viable since the focus is strictly on the snow-free period, hence avoiding the effects of intercepted snow on PAI (Stähli et al., 2009). Also, the evergreen-dominated canopy PAI would not be expected to change much during our study period. The site-dependent PAI values were taken as those that minimize the root mean squared error (RMSE) between observed K_u and those modeled with Equation 1.2 – 1.4.

As mentioned earlier, the method described by Van Gardingen et al. (1999) was tested as well. This method was designed for highly clumped canopies, *i.e.* where leaves (needles) and branches are far from being randomly ordered, like in conifer canopies. The 1° gap fraction grid was separated in 90 × 1° zenith rings, and the average of the natural logarithm of gap fraction was calculated for each ring. PAI was then obtained with the non-linear elimination method described by Van Gardingen et al. (1999) using the algorithm of Norman and Campbell (1989). Because calculations were very sensitive to fringe effects in the photographs, only the zenith rings between 10° and 80° were kept.

Figure 1.3 presents the PAI values obtained using both methods, as a function of the total gap fraction of each associated hemiphoto, along with the theoretical function of Nijssen and Lettenmaier (1999) for random canopies. When evaluated with solar radiation measurements, PAI clearly decreases with increasing gap fraction: this is a generally accepted trend, yet unidentifiable when PAI is calculated from hemiphotos. In addition, PAI values are strictly used as inputs to CLASS in this study. Our focus was to model solar radiation transmittance as accurately as possible to assess its impact on hydrological variables. By design, PAI from solar radiation measurements resulted in improved modeling of sub-canopy solar radiation by CLASS compared to when PAI from hemiphotos were used (R^2 values of 0.57 vs. 0.31, RMSE of 0.14 vs. 0.19 MJ m^{-2}). For these reasons, only PAI values obtained with the solar radiation measurement method were retained as site-specific values.

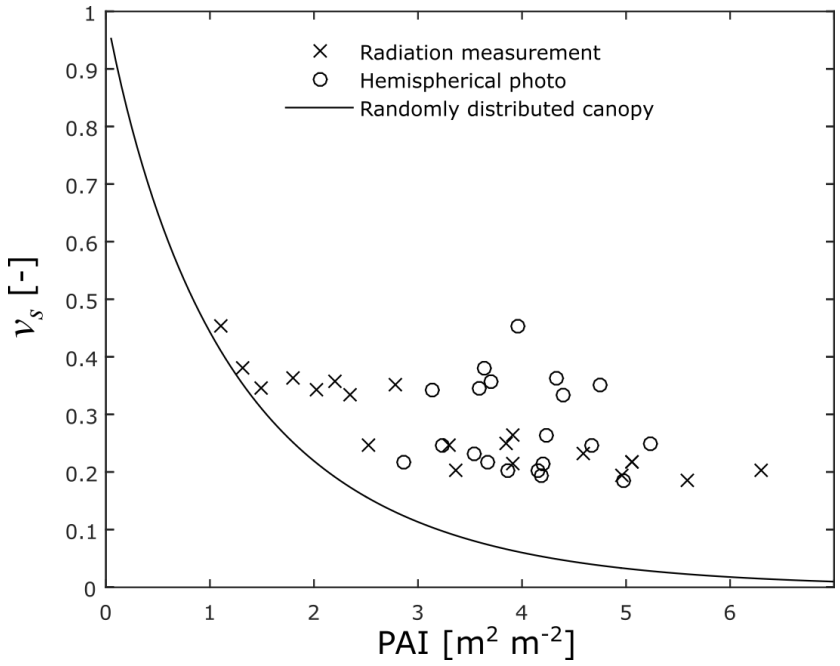

Figure 1.3: Sky view fraction v_s vs. PAI at each sub-canopy station. PAI is obtained from the solar radiation measurement method and from the hemiphotos method (Van Gardingen et al., 1999). The line presents the theoretical function defined for randomly distributed canopies by Nijssen and Lettenmaier (1999).

Additionally, a PAI value representative of the whole plot was tested in CLASS. Its value was obtained from Moderate Resolution Imaging Spectroradiometer (MODIS) LAI (Myneni et al., 2015), a spatial average metric that is a common input to land-surface models. A single value of 3.36 m^2 m^{-2} was calculated by taking the temporal average over the study period for the 500-m tile encompassing our sites.

1.5.3 Spatiotemporal scales of transmittance

Throughout the paper, solar radiation is presented as the cumulative energy over a certain period of time, in MJ m^{-2}. Various spatiotemporal scales of solar radiation transmittance were analyzed, which are related to these summation periods. For example, to quantify sub-daily temporal variability of solar radiation transmittance, analyses were refined to 30-min sums of energy. This timestep illustrates the influence of specific canopy architecture on sub-canopy solar radiation.

To assess the spatial variability of sub-canopy solar radiation over the whole measurement period (≈ 1 season), we focus on time series of daily sums of energy. The daily and seasonal differences between subcanopy stations are then intricately linked to the spatial variability of the seasonal amount of energy available for understorey processes, such as soil evaporation and warming.

1.5.4 CLASS modeling scheme

To run CLASS, the vertical soil profile is defined by layers, each characterized by a defined texture. Three soil layers of 0.10, 0.25 and 3.75 m were used, which is the standard operational configuration for CLASS (Verseghy, 2012). Each layer texture was set based on qualitative observations at the site. The soil at the site has been characterized as a sandy loam (Lavigne, 2007). Thus, its content was set at 55% sand, 35% silt and 10% clay. However, the top layer consists mostly of mor-type humus and hence its content was set to 85% organic, while the remaining 15% was at the same texture proportion as the bottom layers.

In this study, CLASS was run 21 times; one simulation specific to each 20 sub-canopy station and one using PAI from MODIS. Each time, the vegetation type fractional coverage was set at 100% conifers, consistent with plot surveys made at the site. Only the PAI values obtained from solar radiation measurements (see Section 1.5.2) differed amongst the 21 runs. Thus, simulated K_u values from each run were compared to observations at the corresponding sub-canopy stations. Every remaining parameter was set to its default value provided in CLASS technical documentation (Verseghy, 2012).

The CLASS simulations also provided a sensitivity analysis of the impact of changing vegetation cover (*i.e.* PAI) on surface hydrological variables. Five model variables computed by CLASS were analyzed: (i) total evapotranspiration E [mm]; and the partitioning of E in: (ii) ground evaporation E_g [mm]; (iii) transpiration E_t [mm]; (iv) evaporation of intercepted precipitation E_i [mm]; and (v) volumetric water content of the first 10 cm of soil θ [m^3 m^{-3}]. In-situ observations of θ and E were used to verify the simulated values.

1.6 Results

1.6.1 Spatiotemporal variability of transmittance

1.6.1.1 30-min cumulative sub-canopy energy

Fluctuations of sub-canopy solar radiation at the sub-daily timescale highlight the impacts that canopy architecture can have on understorey energetics. Figure 1.4 illustrates fluctuations of the 30-min cumulative solar radiation measured above and under the canopy, for three typical days: a sunny day (August 8), a cloudy day with 1.62 mm of rain (August 14), and a rainy day (August 28; 14 mm of precipitation). Temporal fluctuations of K_u were particularly high during the sunny day, but fairly constant for the cloudy and rainy days.

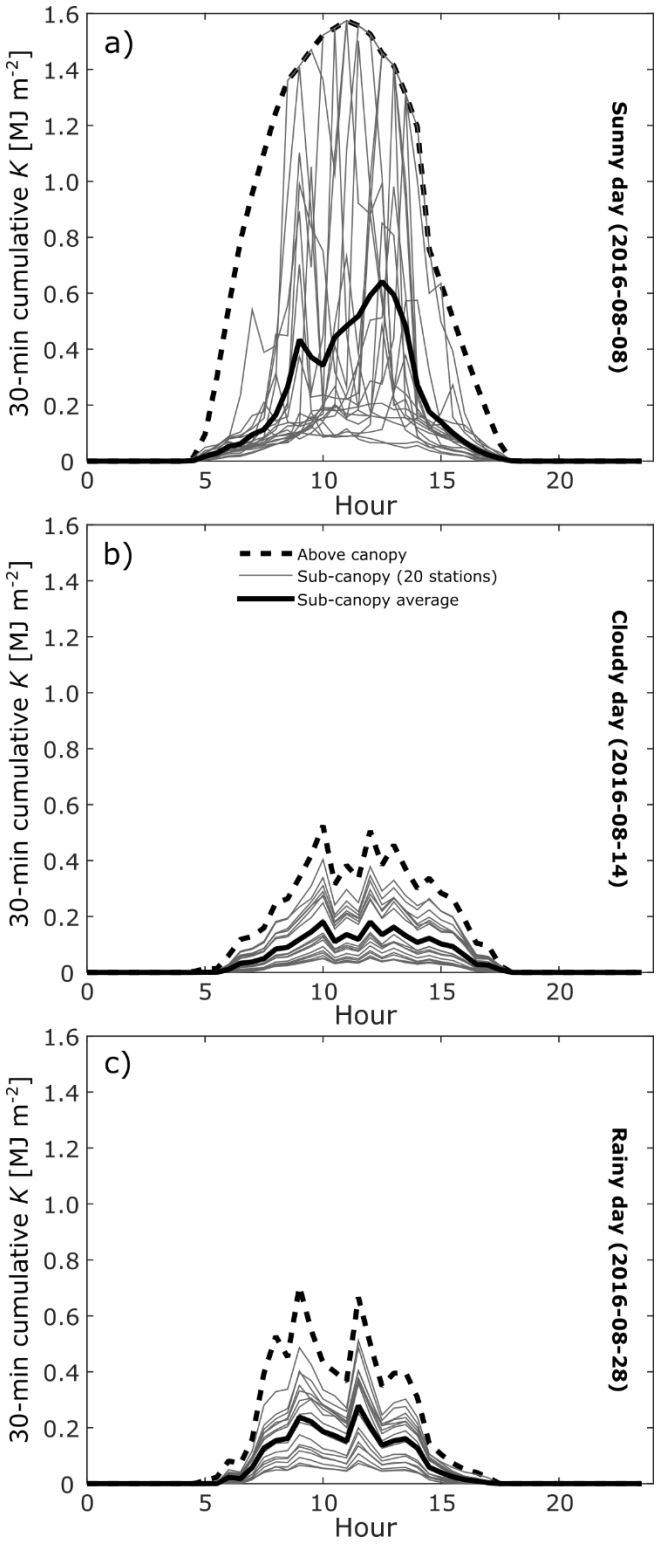

Figure 1.4: Daily cycles of 30-min summed solar radiation above (K_a, thick dashed line) and below (K_u, thin lines) the canopy for three days with different meteorological conditions: (a) a sunny day (2016-08-08); (b) a cloudy day with 1.62 mm of rain (2016-08-14) and; (c) a rainy day with 14 mm of precipitation (2016-08-28). The average of all 20 sub-canopy stations is shown with the thick full line.

The influence of sunflecks was evident during the sunny day (Figure 1.4, a). Some sub-canopy stations measured as much solar energy as above the canopy, but rarely for long. These events coincided with periods when ν_d approached 1.0, that is when the solar disk is in a section of the hemiphotos defined as sky. These sunfleck effects were absent when K_a was mostly diffuse during the cloudy and rainy days. On those days, the diffuse fraction of above canopy solar radiation f_d never fell below 0.7 and was 0.98 on average.

Figure 1.5 presents a side-by-side comparison between observed and CLASS Beer-Lambert modeled 30-min cumulative sub-canopy solar radiation at all sub-canopy stations with the corresponding statistics. Compared to measurements at individual sub-canopy stations, simulated cumulative 30-min K_u yielded R^2 values between 0.26 and 0.66 and RMSE values between 0.02 and 0.25 MJ m^{-2}).

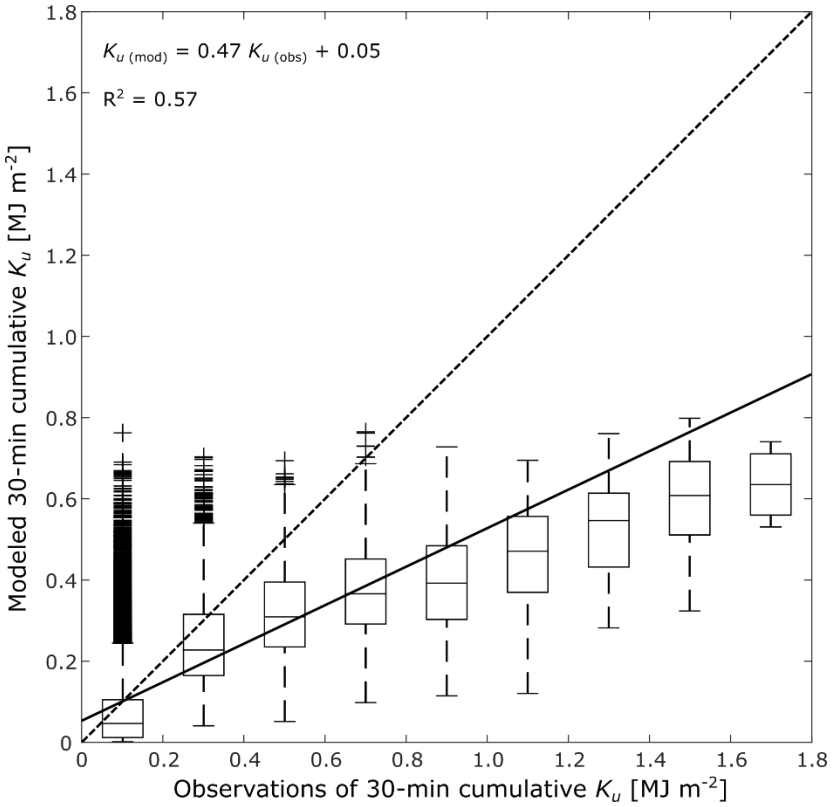

Figure 1.5: Side by side comparison between observed and CLASS modeled K_u at the 20 sub-canopy stations, presented as 30-min cumulative energy in MJ m^{-2}. Data points are grouped in 0.2 MJ m^{-2} bins of observed K_u and a boxplot of modeled K_u is plotted for each bin. "+" are outliers, whiskers are maximum and minimum values without outliers, side of the box are 25th and 75th percentile and thin line within the box is 50th percentile. The dashed line is the 1:1 line, while the solid line is the linear regression between observations and simulated values, with the equation and R^2 shown on top left.

Poor performances occur mostly during sunny days when the subcanopy solar radiation is high (as seen towards the top-right of Figure 1.5). As already mentioned, the Beer-Lambert formulation cannot account for the

discontinuous canopy present in a juvenile balsam fir forest, and the sunflecks it creates. However, the weather was mostly cloudy at the Montmorency forest during our study period: 46 of 70 days had f_d > 0.5 for at least 50% of daylight hours. When solar radiation is mostly diffuse, the Beer-Lambert formulation performs well. Indeed, when f_d was over 0.5, CLASS-simulated sub-canopy solar radiation improved at all sites (R^2 increased from 0.57 to 0.71 and RMSE decreased from 0.14 to 0.07 MJ m^{-2}).

Results also imply that the Beer-Lambert law was adequate at the plot-scale (~ha). Figure 1.6 presents a comparison between CLASS Beer-Lambert modeled K_u and values averaged over all 20 stations at each timestep. The PAI value used for Beer-Lambert extinction was the plot-scale average from MODIS-LAI (3.36 m^2 m^{-2}). CLASS performed very well: the comparison with observations yielded an R^2 value of 0.83 and an RMSE value of 0.06 MJ m^{-2}.

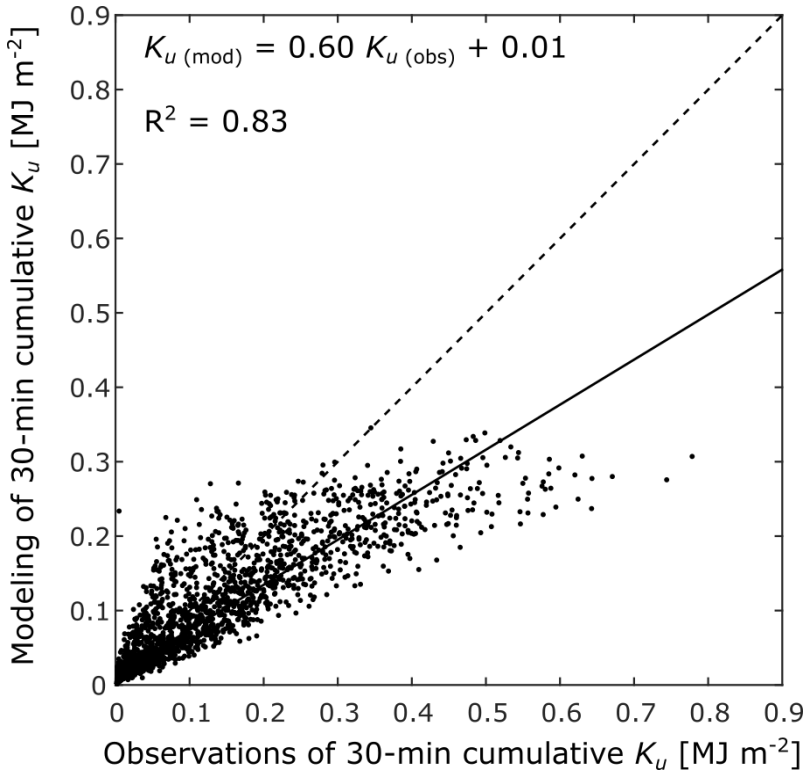

Figure 1.6: Side by side comparison between spatial average of observed K_u and modeling with CLASS using PAI from MODIS. K_u is presented as 30-min cumulative energy in MJ m^{-2}. The dashed line is the 1:1 line, while the solid line is the linear regression between observations and modeling, with the equation and R^2 shown on top left.

This satisfying performance was likely achieved for two reasons. First, averaging τ over 20 sub-canopy sites virtually transforms the canopy into a homogeneous medium. In return, this nullifies the effects of any discontinuous canopy gaps, rendering the exponential reduction of the Beer-Lambert law more accurate. Second, the PAI value given by MODIS (3.36 m^2 m^{-2}) is almost equal to the average of the PAI values measured

at our 20 sites (3.37 m^2 m^{-2}). Of course, the Beer-Lambert formulation becomes very efficient with a homogeneous medium and when properly parameterized.

1.6.1.2 Daily cumulative sub-canopy energy

At larger timescales, fluctuations of the daily sub-canopy energy depict seasonal changes in the spatial variability of τ. Figure 1.7b presents the observed transmittance computed as the ratio of the daily cumulative sub-canopy solar radiation and daily cumulative above-canopy solar radiation. The space between the minimum and maximum curves illustrates the spread of values for the 20 sub-canopy time series. In the boxplot of Figure 1.7a, all data is pooled together. The seasonal mean of τ was ~0.3 for the 20 sub-canopy stations. However, differences between the most and the least radiation-exposed stations were 0.62 on seasonal average and reached 0.91 on August 30.

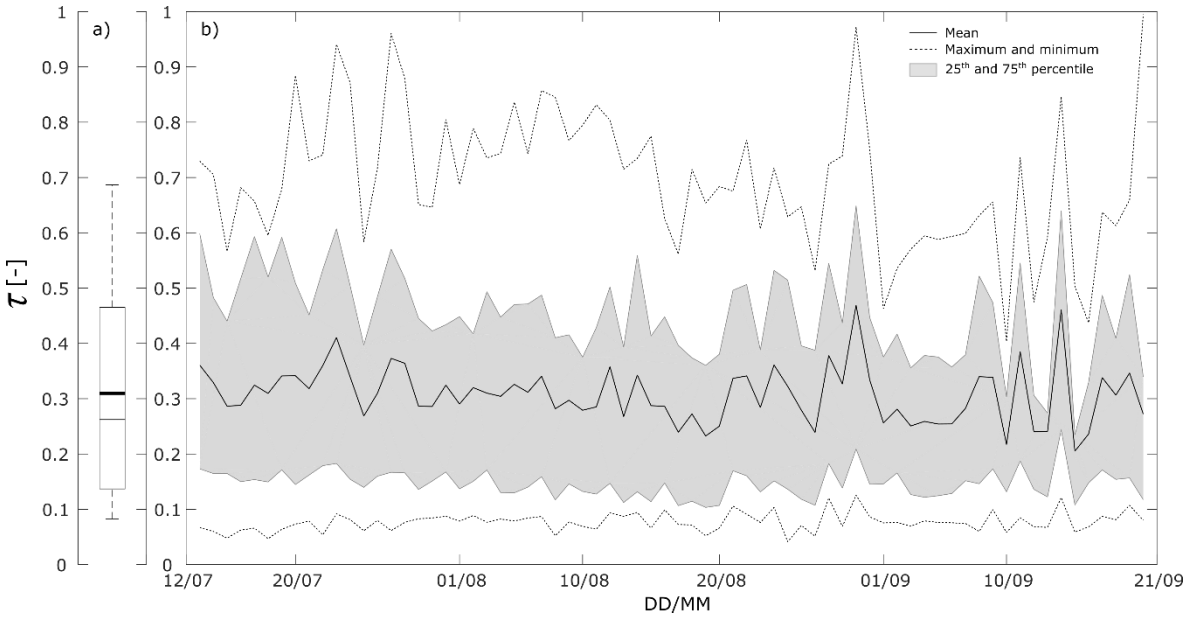

Figure 1.7: (a) Boxplot of seasonal mean of transmittance τ of daily summed sub-canopy solar radiation for all 20 stations. Whiskers are maximum and minimum values, side of the box are 25th and 75th percentile, thin line and thick line within the box are 50th percentile and mean, respectively. (b) Shaded time series of transmittance τ of daily summed sub-canopy solar radiation for all 20 stations. Full line is the mean, shades are 25th and 75th percentile and dashed lines are the maximum and minimum values.

These massive spatial discrepancies in solar radiation transmittance are mostly explained by the heterogeneous vegetation density. Total gap fraction ν_s from the hemiphotos varies between 0.18 and 0.45, while optimized PAI values vary from 1.11 to an impressive 6.29 m^2 m^{-2}. These seasonal bulk vegetation parameters correlate strongly with seasonal averages of station-specific daily τ values (R^2 of ~0.9 when compared with ν_s and PAI), which renders a simple Beer-Lambert formulation quite efficient (between observed daily cumulative K_u from the 20 sites and that modeled with CLASS Beer-Lambert, R^2 is 0.87 and RMSE is 1.22 MJ m^{-2}; results not shown).

Radiation transmittance does not exhibit a spatial pattern across the sub-canopy stations. Figure 1.8 presents point values of seasonal averages of τ and of PAI optimized values with vegetation height derived from a local LIDAR survey. The southeast side of the study domain features the highest variability by encompassing the least (14, 15) and most (18, 19) radiation-exposed sub-canopy stations. Nevertheless, neither transects of northeast-southwest nor northwest-southeast averages of seasonal τ or PAI exhibits a significant spatial trend (results not shown).

Given the absence of spatial trend in vegetation characteristics, an estimate of the minimal and optimal number of sub-canopy stations to properly describe the vegetation was made. We randomly sampled *N* sub-canopy stations and computed the average PAI value from this sub-dataset. We repeated this operation 100,000 times for each *N* value between 1 and 20 stations and computed the coefficient of variation (CV; standard deviation divided by the mean) of the 100,000 PAI averages for each *N* (results not shown). CV drops by 80%, from 0.5 to 0.1, when *N* = 10 stations, and the next 10 stations decrease CV by only 20%. Therefore, according to the dataset, 10 sub-canopy stations are enough to accurately characterize the average PAI value at this site.

1.6.2 Impacts of solar radiation transmittance on growing season hydrology

Prior to the results showing the sensitivity of CLASS to PAI values, a justification of the relevance of this type of analysis is warranted. First, we assume that a sensitivity analysis based on PAI values is a proper way to assess the impacts of solar radiation transmittance on sub-canopy hydrology, which is a worthy assumption considering the strong correlation between seasonal τ and PAI. Second, we assume that CLASS simulations of hydrological variables will agree well with measurements. Indeed, compared to observations, CLASS adequately modeled the 30-min cumulative *E* (for the whole season and 20 PAI values, when comparing observed and modeled *E* values, R^2 is between 0.64 and 0.70, while the RMSE varies from 0.037 to 0.044 mm). The good correspondence between measured and modeled *E* and the satisfying modeling of K_u provide confidence in the suitability of CLASS and its parameterizations to simulate canopy transmittance effects on evapotranspiration partitioning.

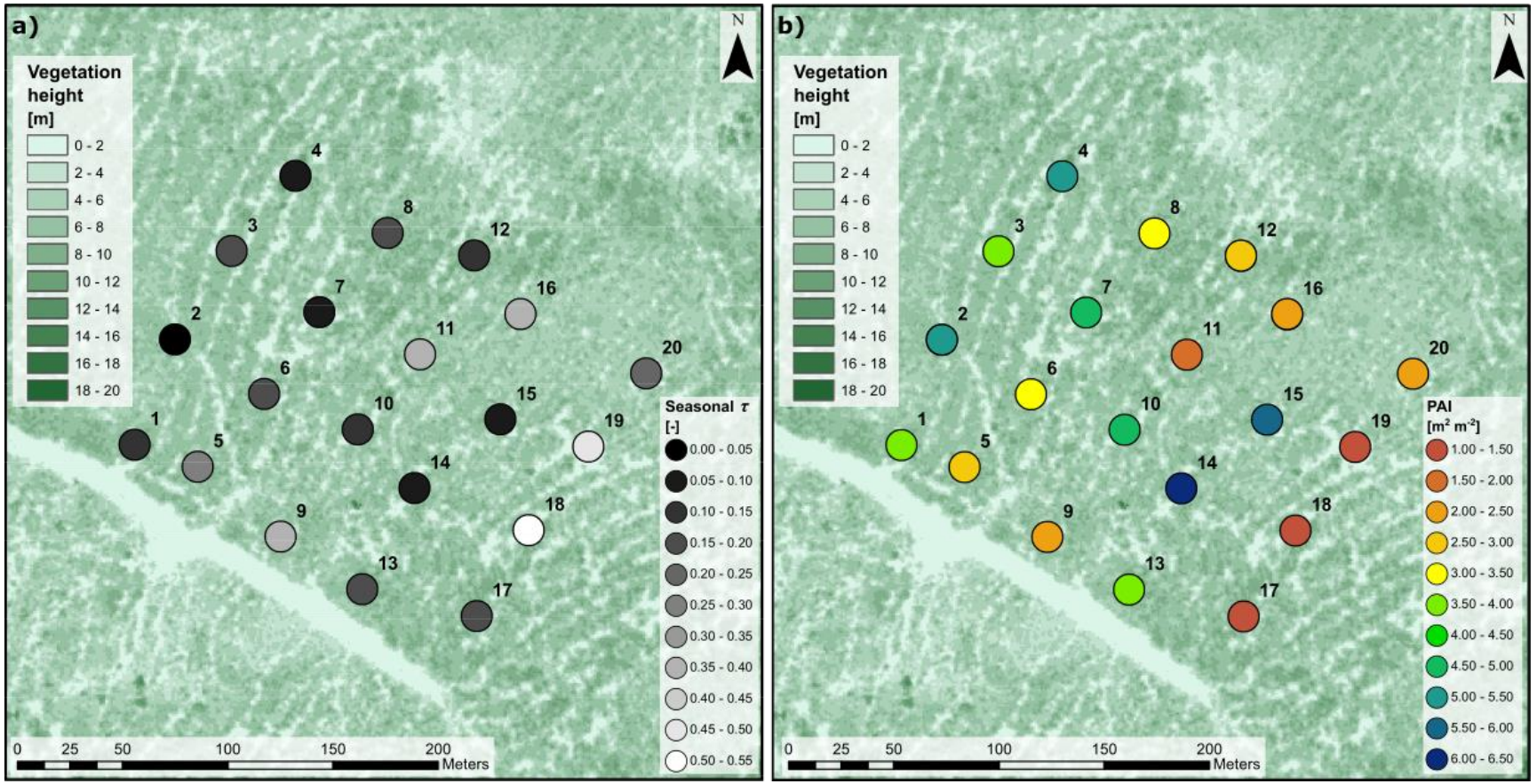

Figure 1.8: Spatial representation of (a) observed seasonal τ; and (b) PAI values at the 20 sub-canopy stations, over vegetation height map from LIDAR surveys (Source: Ministère Forêts, Faune et Parcs du Québec).

1.6.2.1 *Impacts on evapotranspiration partitioning*

Figure 1.9 illustrates the daily cycles of 30-min cumulative E and their components (in each column) for the same three days as in Fig. 4 (in rows). Note that the non-zero E_i at the start of the sunny day was likely caused by the evaporation of a 1.5 mm precipitation event that occurred during late evening the day before. Total evapotranspiration E did not vary much between PAI values in Figure 1.9. On sunny days, transpiration E_t increased considerably with increasing PAI values with the maximum deviation reaching 0.11 mm. These differences were slightly overcompensated by an opposite effect on ground evaporation E_g, which increased with decreasing PAI values (maximum deviation of 0.14 mm), resulting in a slightly lower midday E at the highest PAI. This happened only for sunny days that followed recent precipitation: otherwise, the differences in E_t exceeded those in E_g, meaning that a higher E was modeled at higher PAI (results not shown). A similar phenomenon happened on the rainy day, where differences in E_g (maximum of 0.10 mm) were overcompensated by differences in evaporation of intercepted water E_i (maximum of 0.15 mm), leaving a slightly higher midday E at the highest PAI. For cloudy days, all E components were low, so deviations associated with changing PAI were minimal.

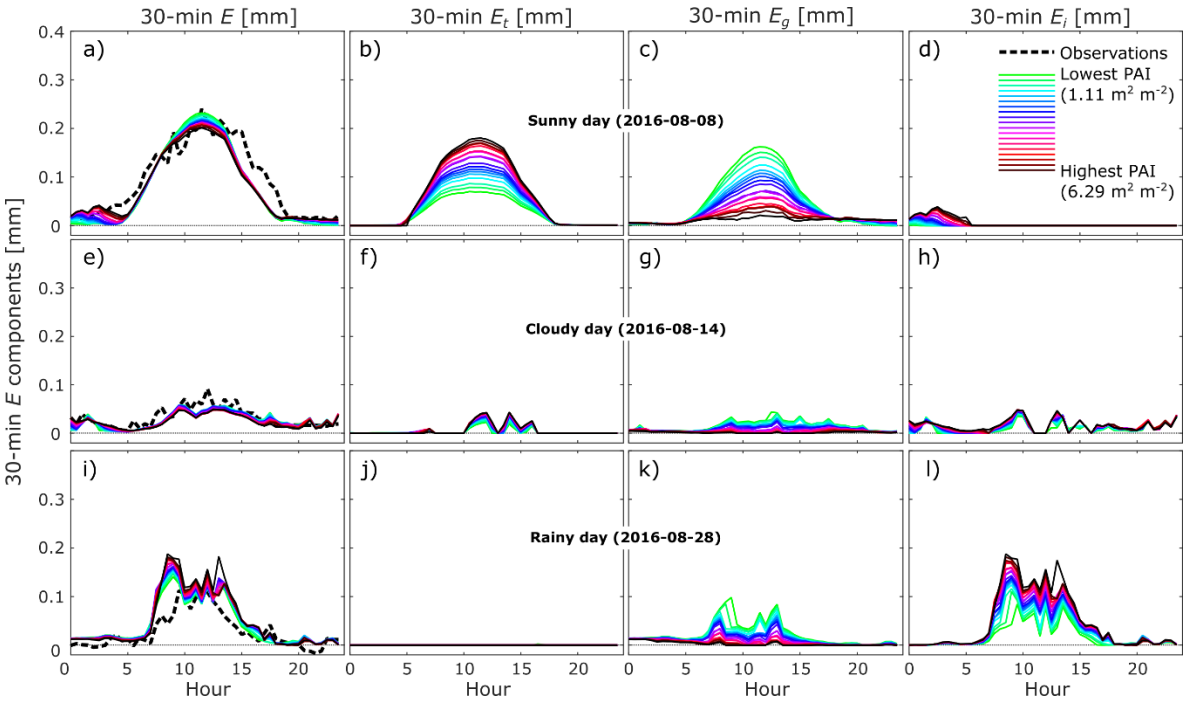

Figure 1.9: Daily cycles of 30-min summed E and its components modeled by CLASS with 20 different PAI values. Columns are for total evapotranspiration E, transpiration E_t, ground evaporation E_g and evaporation of intercepted precipitation E_i, respectively. Rows are for the sunny day (2016-08-08, (a) to (d)), the cloudy day (2016-08-14, (e) to (h)) and the rainy day (2016-08-28, (i) to (l)).

These competing effects lead nonetheless to some deviations in seasonal cumulative *E*. Figure 1.10 presents the time series of seasonal cumulative *E* and its components for sub-canopy optimized PAI values. A total deviation of 13 mm of *E* was modeled, or ~7% of the ~193 mm of total measured *E*. The stark differences in E_g (up to ~53% of total measured *E*) were largely compensated by E_t and E_i from a denser canopy (up to ~20% and ~39% of total measured *E*, respectively). On a seasonal basis, the compensating effects on rainy days (larger differences in E_i than in E_g between highest and lowest PAI) dominated those observed on sunny days (larger differences in E_g than in E_t between highest and lowest PAI), a direct consequence of the fact that the season had more cloudy and wet days than sunny ones.

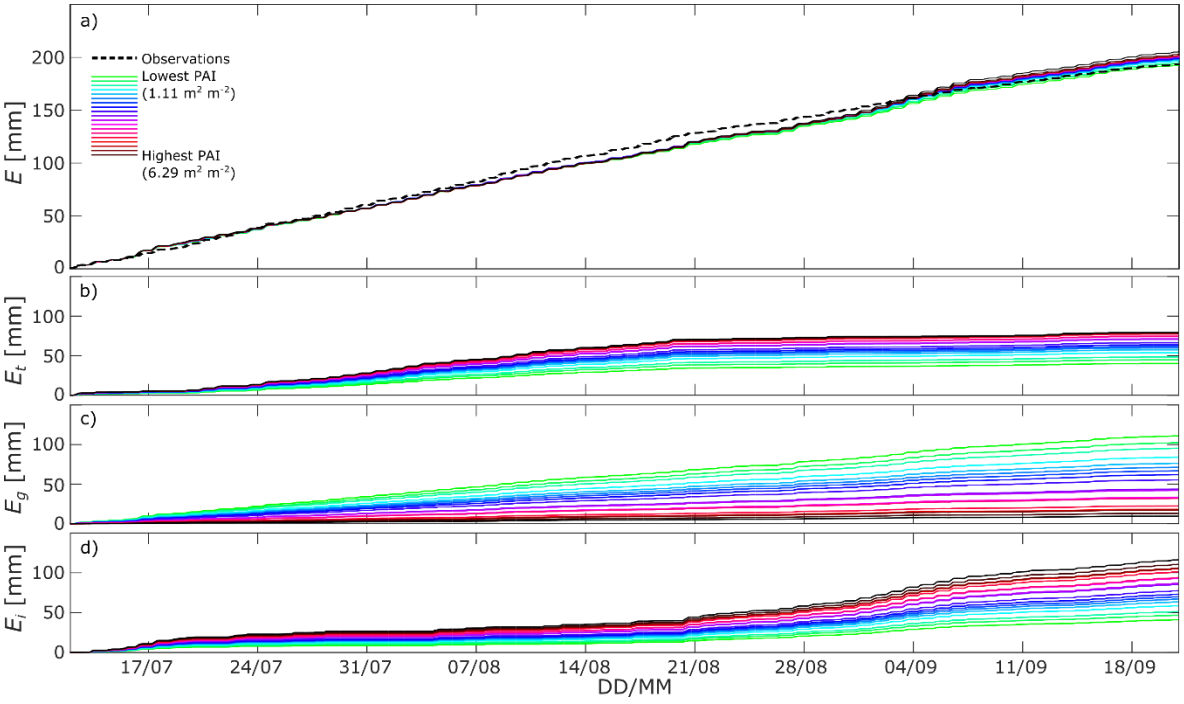

Figure 1.10: Seasonal evolution of cumulative evapotranspiration and basic components: (a) total evapotranspiration *E* with observations; (b) E_t; (c) E_g; and (d) E_i.

Seasonal cumulative *E* was closest to observations using a PAI value of 1.11 m^2 m^{-2}. Correlation between observed and modeled 30-min cumulative *E* was also maximized with the lowest PAI value (1.11 m^2 m^{-2}) and minimized with the highest PAI value (6.29 m^2 m^{-2}). Figure 1.10 shows that CLASS seems to generally underestimate *E*, regardless of PAI, until August 28. After that date, rainfall became frequent, and the denser vegetation generated substantial evaporative fluxes through E_i that caused modeled cumulative *E* to be closer to observations. Note however that cumulative uncertainties in measured *E* calculated with the commonly used Finkelstein and Sims (2001) method amounted to ~30 mm or ~16% of total measured *E*.

To better ascertain the hydrological impacts of these results, Table 1.1 illustrates the differences in the sub-canopy water budget calculated by CLASS over the full range of measured PAI values. The proportion of each term relative to total cumulative P (359 mm) is shown. As CLASS enforces a closed water budget, the full precipitation either reaches the ground (P_g) or is evaporated after interception (i.e. $P = E_i + P_g$). The sub-canopy budget is also balanced, with the ground-reaching precipitation compensated by ground evaporation, transpiration, runoff R, surface ponding of water (included in runoff here), and soil infiltration that changes soil water storage ΔS (*i.e.* $P_g = E_g + E_t + R + \Delta S$).

Table 1.1: Water budget components as proportion of total incoming precipitation P (359 mm) for the lowest and highest PAI values measured at our sites (1.11 and 6.29 $m^2\ m^{-2}$, respectively). R is the total soil runoff, while ΔS is the variation of soil water storage.

	% of P	
	Lowest PAI	Highest PAI
E_i	11.5	32.6
E_g	40.0	2.7
E_t	11.2	22.1
R	42.9	39.4
ΔS	3.4	3.2

The first effect of a denser vegetation is to intercept more precipitation that is then returned to the atmosphere as E_i (+21.1% of P from lowest to highest PAI). This created a difference of ~76 mm of water reaching the ground over the whole season. The lower exposure of the ground to K_u at high PAI, however, created a large difference in ground evaporation (−37.3% of P from lowest to highest PAI). As previously mentioned, this difference is generally superseded by the reverse trend in E_i, and transpiration E_t (+10.9% of P from lowest to highest PAI), meaning that more total evapotranspiration occurs with a thicker vegetation. At ground level, runoff R and changes in soil moisture ΔS seem relatively similar with changes in PAI, implying that simulating a denser vegetation has a relatively limited impact on these terms.

1.6.2.2 Impacts on soil moisture

The weak differences in ΔS with increasing vegetation density create small seasonal differences in the volumetric water content θ of the top 10 cm of the soil. Figure 1.11 compares observed and simulated seasonal variation of θ for the 20 CLASS runs, along with cumulative daily precipitation. Maximum deviations in θ (~0.03 $m^3\ m^{-3}$) were reached several days after the last substantial precipitation event (*e.g.* the relatively dry period between July 28 and August 21). When a substantial precipitation event occurred (*e.g.* July 22, August 5, 21, September 8), the 20 θ time series converge. From this we infer that during periods of substantial

precipitation, the water retention capacity of all canopy densities is satisfied, and the excess water volumes brings the soil to near saturation.

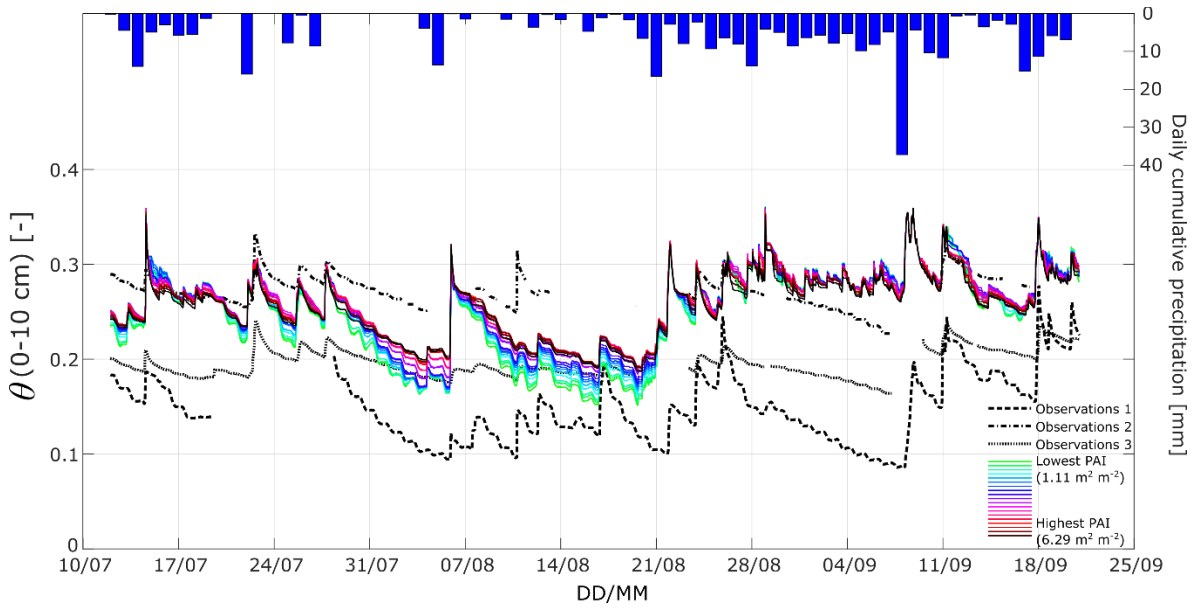

Figure 1.11: Seasonal evolution of top soil volumetric water content θ modeled by CLASS with 20 different LAI values. Observations at 8 cm below the surface from three CS650 sensors are also plotted as a reference. Daily summed precipitation is shown on top.

During dry spells, θ becomes markedly lower with thinner vegetation. Interestingly, one cause may be the frequent occurrence of weak rainfall events during that period. As previously mentioned, differences in E_g between dense and thin vegetation were larger than those in E_t for sunny days following precipitation. When PAI is low, even low precipitation volumes reach the ground, which in turn generates higher E_g when solar radiation increases. However, after a few days without precipitation, θ decreased more rapidly at low PAI as did E_g. With enough time, differences in E_t between thin and dense vegetation surpass those in E_g, but this seldom happened during the relatively wet study period.

This positive trend between θ and PAI does not always hold. In several instances, thinner vegetation led to wetter soil, usually in periods with high precipitation, low solar radiation and hence lower E_g (*e.g.* around September 1 to 7; see Figure 1.11). There were also periods where θ is highest at a PAI value that was neither the maximum nor minimum of our dataset (*e.g.* between September 12 and 18). At this time, autumn is setting in and solar radiation diminishes while precipitation rates increase, strongly weakening E_t. Total evapotranspiration is then mostly partitioned between E_i and E_g. There seemed to be a cut-off PAI value, around 3.30 $m^2 m^{-2}$, that created a minimum of the sum of E_i and E_g and therefore maximum soil water content.

1.7 Discussion

The modeling framework assumes spatially invariant physical properties and composition of the soil layers, described in Section 1.5.4. In practice, spatially variable soil properties, slopes and microtopography induce a variability in small-scale surface hydrology. This is especially the case for soil moisture, but also evapotranspiration since the soil water content influences stomatal resistance. As an example, the observations of θ shown in Figure 1.11 are only separated horizontally by a few meters, yet results are starkly different. CLASS can simulate these differences by its sensitivity to soil parameters. Increasing the top soil layer porosity accentuates the divergence in soil moisture between thinner and denser vegetation. It also makes θ more reactive to precipitation. However, keeping fixed soil properties and composition has the advantage of isolating the effects of vegetation on the modeling of surface hydrology.

A similar comment can be made on understorey vegetation diversity. It is well-known that the variability of solar radiation transmission induces a similar variability in understorey vegetation species and density (Aubin et al., 2000). Typically, more shrubs are present in forest clearings where sunlight is available. Evidently, this understorey vegetation variability causes differences in evapotranspiration partitioning and soil moisture dynamics. In its current version, CLASS models a single-layer canopy and cannot account for that understorey vegetation. In any case, results generated from models are always indicative rather than conclusive, until appropriate observations are made, and uncertainties are characterized.

Despite these limitations, our results support previously identified trends, especially during the driest part of the season at our study site. For example, from modeling results in a Mediterranean semi-arid basin, Gigante et al. (2009) also describe that a denser vegetation reduces simulated E_g, yet increases E_i and E_t, thus increasing total evapotranspiration compared to results with a thinner canopy. This general trend is also supported by other studies (*e.g.* Simic et al., 2014; Tesemma et al., 2015). However, not all research agrees on this tendency: Pongratz et al. (2006) modeled a slight decrease in E with denser vegetation during the dry season in Mato Grosso, Brazil. Nonetheless, in dry conditions, higher vegetation density has been mostly linked to lower soil moisture due to larger evapotranspiration fluxes (*e.g.* Montaldo et al., 2005; Ford and Quiring, 2013; Simic et al., 2014; Tesemma et al., 2015).

This last feature contrasts with our observations, where during the dry period, the increase in E_g from a thinner vegetation causes lower soil moisture. However, all of these studies focus on deciduous or grassland vegetation, subject to more E_t than conifers. Consequently, the positive effect on E_t of increasing the density of a more water-demanding vegetation may supersede the negative effect on E_g and reduce soil moisture. Also, the dry periods of the surveyed regions are notably drier than those of our study site. At the Montmorency

forest, it is possible that E_t could generate lower soil moisture with denser vegetation after more consecutive days without precipitation.

Our results indicate that a proper representation of solar radiation transmittance is essential to the hydrometeorological modeling of a humid boreal forest typical of northeastern North America. τ dictates the partitioning of E and thus has a strong impact on soil moisture and runoff during periods between rainfall events. This has implications for the relatively dry boreal forests of the western Great Plains of Canada, for example. Modelers focusing on these regions should obtain accurate ground measurements of PAI whenever possible. Conversely, the Montmorency forest experiences frequent cloudiness and precipitation. The cloudy conditions support the use of a simple Beer-Lambert formulation. This is an important finding with implications on large-scale modeling efforts, leveraging the accuracy of remotely-sensed PAI values shown here. Frequent precipitation effectively eliminates the discrepancies in soil moisture between vegetation densities created during dry spells.

1.8 Conclusion

This study describes the spatiotemporal variability of sub-canopy solar radiation in a juvenile balsam fir canopy. An experimental design comprised of 20 sub-canopy sensors and one above-canopy solar radiation sensor permitted an extensive plot-scale analysis. The spatial variability was substantial: the seasonal cumulative energy transmitted through the canopy ranged from 7.4% to 55.4% of the seasonal cumulative above-canopy energy (1061.1 MJ m^{-2}). That variability can be explained by the vegetation bulk density around the stations, with Beer-Lambert optimized PAI values ranging between 1.11 and 6.29 m^2 m^{-2}. Temporal variability is related to the location of canopy gaps and general regional cloudiness. The former creates high variability of τ at the sub-daily scale, when the sun can pass through openings in the canopy. The general cloudiness effectively nullifies sunfleck effects by making the solar radiation mostly diffuse. Since the climate of the research site is characterized by frequent precipitation events and clouds, the sub-daily temporal variability of transmitted solar radiation can be neglected at longer timescales.

This last feature contributed to a fairly good performance of the Beer-Lambert formulation at most of the 20 sites. The comparison is particularly striking when the model is compared to plot-scale averages of transmittance. This should not be surprising as this plot-scale averaging assimilates the canopy as a homogeneous medium, which satisfies the underlying assumptions of the Beer-Lambert law. An interesting conclusion of this study is that the PAI value obtained from MODIS is highly similar to the plot-scale average of our observations. This provides a convincing argument to use MODIS-derived PAI values with the Beer-Lambert formulation to model plot-scale averaged solar radiation transmittance at sites where clouds and frequent precipitation are dominant.

To conclude, this study has shown that a simple transmittance model can be accurate in a juvenile balsam fir forest at the scales studied here. The Beer-Lambert formulation adequately characterized seasonal and even daily sub-canopy energy when PAI values were correctly specified. According to sub-canopy solar radiation measurements, PAI over our 0.03 km^2 site could be adequately estimated with 10 sensors. Field measurements are ideal, but the results shown here indicate that satellite-derived values may be appropriate, although this conclusion should be investigated at other locations characterized by different vegetation types.

The study assessed the impacts that this spatiotemporal variability in τ could have on growing season hydrology of the forest. Precipitation interception, partitioning of evapotranspiration, and soil moisture were simulated using the CLASS land surface model with 20 values of Beer-Lambert optimized PAI values used as a proxy of τ. Results indicate that denser (thinner) vegetation lead to more (less) total evapotranspiration, because there is more (less) evaporation of intercepted precipitation and more (less) transpiration. However, denser (thinner) vegetation lead to less (more) ground evaporation.

During drier periods, this last phenomenon lead to increased soil moisture conditions for denser vegetation. Given enough days between precipitation events, this trend would likely reverse, causing soil moisture to be lower with denser vegetation; however, this was not observed during the wet study period. Frequent occurrence of heavy precipitation seems to nullify the effect that PAI has on θ. This was especially apparent starting at the end of August when precipitation became more frequent and intense. Thus, model efforts focusing on dry boreal forests should obtain precise estimates of vegetation parameters to assure the highest accuracy in soil moisture. On the other hand, humid boreal forests do not seem to demand such accurate parametrisation. These modeling results will serve to guide future in situ observations and modeling campaigns in more diverse climate and in regions with different vegetation species.

1.9 Acknowledgments

The authors acknowledge all Montmorency Forest staff, especially Patrick Pineault and Charles Villeneuve, for their extremely valuable help in the field. We also would like to thank Annie-Claude Parent, Dany Crépault, Denis Jobin, Benjamin Bouchard, Sophie Robitaille, Martin Pharand, Derek Jensen, Chaoxun Hang, Pascale Girard, Gabriel Hould Gosselin, Jean-Pierre Tatchegnon Gbegan, Marco Alves, Achut Parajuli, Bram Hadiwijaya and Fabien Gaillard Blancard for their help installing and maintaining the micrometeorological towers. This work was funded by the Natural Sciences and Engineering Research Council of Canada (NSERC), the Fonds de recherche du Québec – Nature et technologies, the Ouranos Consortium, Hydro-Québec, Environment and Climate Change Canada, and Ministère du Développement durable, de l'Environnement et de la Lutte contre les Changements climatiques, through NSERC project RDCPJ-477125-14.

2 Impacts of high precipitation on the energy and water budgets of a humid boreal forest

2.1 Résumé

Les changements climatiques affecteront fortement la forêt boréale et, à leur tour, ces vastes écosystèmes pourraient avoir un impact important sur la climatologie et l'hydrologie mondiales en raison de leurs échanges de carbone et d'eau avec l'atmosphère. Il est maintenant crucial de comprendre les relations complexes entre précipitations et évapotranspiration dans ces environnements, en particulier dans des zones peu étudiées caractérisées par un climat froid et humide. Cette étude présente les mesures les plus récentes des composantes des bilans énergétique et hydrique sur trois ans (2016-2018) à la forêt de Montmorency (Québec, Canada), une forêt boréale de sapin baumier qui reçoit environ 1600 mm de précipitations par an (climat continental subarctique ; sous-type de classification de Köppen : Dfc). Les précipitations, l'évapotranspiration et l'évapotranspiration potentielle au site sont comparées aux observations de treize sites expérimentaux du monde entier. Ces sites de comparaison, totalisant 89 années d'études, englobent différents types de climat et de végétation (épinettes noires, pins gris, etc.) rencontrés dans les forêts boréales du monde entier. La forêt de Montmorency se distingue en recevant la plus grande quantité de précipitations. Sur tous les sites, la disponibilité de l'eau semble être la principale contrainte de l'évapotranspiration, les précipitations ayant tendance à avoir plus d'influence que l'évapotranspiration potentielle ou que d'autres facteurs. Cela conduit la forêt Montmorency à générer la plus grande quantité d'évapotranspiration, en moyenne 550 mm an^{-1}. Cette valeur semble être un maximum écosystémique pour l'évapotranspiration, ce qui peut s'expliquer par une limite physiologique ou par une disponibilité énergétique limitée en raison de la présence d'un couvert nuageux. Le bilan hydrique de la forêt de Montmorency évacue l'excès de précipitations principalement par des débits sortants du bassin versant, à un taux moyen d'environ 1050 mm an^{-1}, avec des pics pendant la crue printanière. Ce comportement, typique des bassins d'altitude montagneux, influence nécessairement dans une large mesure les régimes hydrologiques en aval. Cette étude fournit des informations indispensables sur les régimes hydrologiques d'un bassin versant montagneux couvert de forêt boréale humide, un type de bassin rarement étudié avec des bilans énergétiques et hydriques précis.

2.2 Abstract

The boreal forest will be strongly affected by climate change and in turn, these vast ecosystems may significantly impact global climatology and hydrology due to their exchanges of carbon and water with the atmosphere. It is now crucial to understand the intricate relationships between precipitation and evapotranspiration in these environments, particularly in less-studied locations characterized by a cold and humid climate. This study presents state-of-the-art measurements of energy and water budget components

over three years (2016-2018) at the Montmorency Forest, Québec, Canada: a balsam fir boreal forest that receives ~1600 mm of precipitation annually (continental subarctic climate; Köppen classification subtype Dfc). Precipitation, evapotranspiration and potential evapotranspiration at the site are compared with observations from thirteen experimental sites around the world. These intercomparison sites (89 study-years) encompass various types of climate and vegetation (black spruces, jack pines, etc.) encountered in boreal forests worldwide. The Montmorency Forest stands out by receiving the largest amount of precipitation. Across all sites, water availability seems to be the principal evapotranspiration constraint, as precipitation tends to be more influential than potential evapotranspiration and other factors. This leads to the Montmorency Forest generating the largest amount of evapotranspiration, on average ~550 mm y^{-1}. This value appears to be an ecosystem maximum for evapotranspiration, which may be explained either by a physiological limit or a limited energy availability due to the presence of cloud cover. The Montmorency Forest water budget evacuates the precipitation excess mostly by watershed discharges, at an average rate of ~1050 mm y^{-1}, with peaks during the spring freshet. This behaviour, typical of mountainous headwater basins, necessarily influences downstream hydrological regimes to a large extent. This study provides a much needed insight in the hydrological regimes of a humid boreal-forested mountainous watershed, a type of basin rarely studied with precise energy and water budgets before.

2.3 Introduction

The boreal forest covers roughly 14% of the Earth emerged surface, globally enclosing 30% of the world's forests (Brandt et al., 2013; Gauthier et al., 2015). It is the second largest vegetated area in extent (12 to 14 million km^2) behind tropical forests (Landsberg & Gower, 1997). Furthermore, it sequesters 20% of the global forest carbon (Pan et al., 2011). On the whole, the circumpolar boreal biome controls fluxes of carbon and water over a huge area and thus impacts the Earth's global climatology and hydrology. In return, global climate tremendously affects the boreal forest; this biome will in all likelihood experience one of the strongest warming in the future (IPCC, 2013), lengthening the growing season and forest productivity (Kauppi et al., 2014; Schaphoff et al., 2016; Liu et al., 2019). In some regions, these changes could be modulated by lower precipitation leading to conditions where evapotranspiration is unable to meet an increase in evaporative demand (Barber et al., 2000; Lloyd & Bunn, 2007; Walker et al., 2015). However, boreal forest regions of northeastern North America, enduring large precipitation, could be sheltered from such destructive effects (D'Orangeville et al., 2016).

For these reasons, there is a need to further our understanding of the intricate relationship between precipitation (*P*), evapotranspiration (*E*), and evaporative demand in various regions of the boreal forest. The first step towards this goal is to quantify the energy and water budgets of the ecosystem.

The surface energy budget of for a watershed covered by forest can be described as follows:

$$R_n = H + L_v E + G + \Delta Q \tag{2.1}$$

where R_n is the net radiation; H, the sensible heat flux; L_vE, the latent heat flux associated with evaporation of surface water and transpiration of vegetation, or evapotranspiration; G, the soil heat flux; ΔQ, variations in storage of heat in the air and biomass below a certain height – all terms are expressed as energy fluxes per surface area in W m^{-2}.

Similarly, the water budget of a watershed can be described as:

$$P = E + O + \Delta S \tag{2.2}$$

where P is the total precipitation; E, the evapotranspiration; O, the watershed outflow, in streams and grounds; ΔS, the storage variations of water in the ground via water table and soil water content fluctuations and above the ground via snowpack accumulation – with all terms are expressed in mm; that is for a given time interval as water volumes per surface area of the watershed. In both budgets, the left-side terms are input of energy or water, while right-side terms generally express outputs. E is the obvious link between energy and water budgets, appearing in both Equations 2.1 and 2.2 (as a mass flux in the former and as a water height in the second, the latter being the mass flux multiplied by the time interval over water density).

The boreal forest energy budget has been documented at length during the Boreal Ecosystem Atmosphere Study (BOREAS; Sellers et al., 1995; 1997) and in the ensuing measurement years at the Boreal Ecosystem Research and Monitoring Sites (BERMS; Barr et al., 2002). The mostly evergreen canopy absorbs a large amount of solar radiation year-long (Sellers et al., 1997). In the BERMS studied area, the absorbed energy returns to the atmosphere mostly by means of H (Saugier et al., 1997; Barr et al., 2001; Coursolle et al., 2006; Gao et al., 2017), except in the presence of deciduous species (Blanken et al., 1997; Zha et al., 2010; Brown et al., 2014). The incidentally low E rates still account for a large portion of annual P, leaving small volumes to generate watershed outflows (Nijssen & Lettenmaier, 2002; Barr et al., 2012). Similar results were also observed in Scandinavia (Ilvesniemi et al., 2010) and Russia (Oltchev et al., 2002).

Because of their climate, the aforementioned BERMS sites cannot effectively describe the effects of high rainfall on the energy and water budgets of the boreal forest. While the humid forests of northeastern North America have been studied for their carbon budget (Giasson et al., 2006; Bergeron et al., 2007; Payeur-Poirier et al., 2012), a detailed description of the interrelationships between the energy and water budgets is still lacking. Besides, very few studies have used precise E measurements to assess the water balance of the boreal forest at the watershed scale (*e.g.*, Nijssen & Lettenmaier, 2002; Ilvesniemi et al., 2010; Barr et al.,

2012), none in precipitation-heavy regions, to the best of our knowledge. Given that these regions are expected to undergo changing climate conditions, more studies are needed.

This work assesses the impacts of high precipitation on boreal forest energy and water budgets for the balsam fir – white birch bioclimatic domain. The experimental site is a small watershed featuring an extensive instrumental setup measuring most terms of the energy and water budgets. The watershed, at the southern extent of the circumpolar boreal biome, is subject to particularly high precipitation, making it an ideal site for this study. This paper is specifically interested in: (i) comparing the energy and vertical water budgets of the main study site and specifically *E-P* interactions with observed values in other boreal forest sites around the world; and (ii) quantify the impact of *E-P* interactions on the water budget, specifically on measured discharges. Results are based on three-year flux tower measurements in two locations featuring trees at different stages of maturity. Comparison data include 89 study-years spread over 13 sites around the circumpolar boreal biome.

2.4 Main Study Site

2.4.1 Site description

The main study site is located in the Montmorency Forest (47°17'18"N; 71°10'05.4"W), 80 km north of Québec City, Canada (BF1993 and BF2003 in Figure 2.1c), part of the balsam fir – white birch bioclimatic domain. Specifically, two flux towers were installed in the "Bassin Expérimental du Ruisseau des Eaux-Volées" (BEREV) (Lavigne, 2007; Tremblay et al., 2008, 2009; Nöel et al., 2014; Isabelle et al., 2018a). This experimental watershed lies at a mean altitude of 750 m above mean sea level (AMSL) with peaks at 1000 m AMSL. Figure 2.1a presents the boundaries of two sub-catchments of the BEREV covering an area of 3.49 km^2. The sub-catchment A, located upstream of the sub-catchment B, is gauged and has a 1.04-km^2 area; the sub-catchment B, which is also gauged, has a 2.45-km^2 area. The general slope of the entire catchment, referred to here as AB, is 0.064 m m^{-1}.

The vegetation of both catchments consists mostly of balsam fir (*Abies balsamea* (L.) Mill) along white birch (*Betula papyrifera* Marsh) and white spruce (*Picea glauca* (Moench) Voss) (Lavigne, 2007; Tremblay et al., 2008, 2009). Trees reach heights between 4-8 m in the sub-catchment A, the product of natural regeneration after the logging of 85% of the trees in 1993. The trees are labeled as "juvenile", hence the flux tower name. Sub-catchment B was logged progressively between 2000 and 2010, but not entirely. Tree height distribution is heterogeneous, but in the vicinity of the flux tower prevail trees 2-4 m tall that were classified as "sapling", hence naming the flux tower.

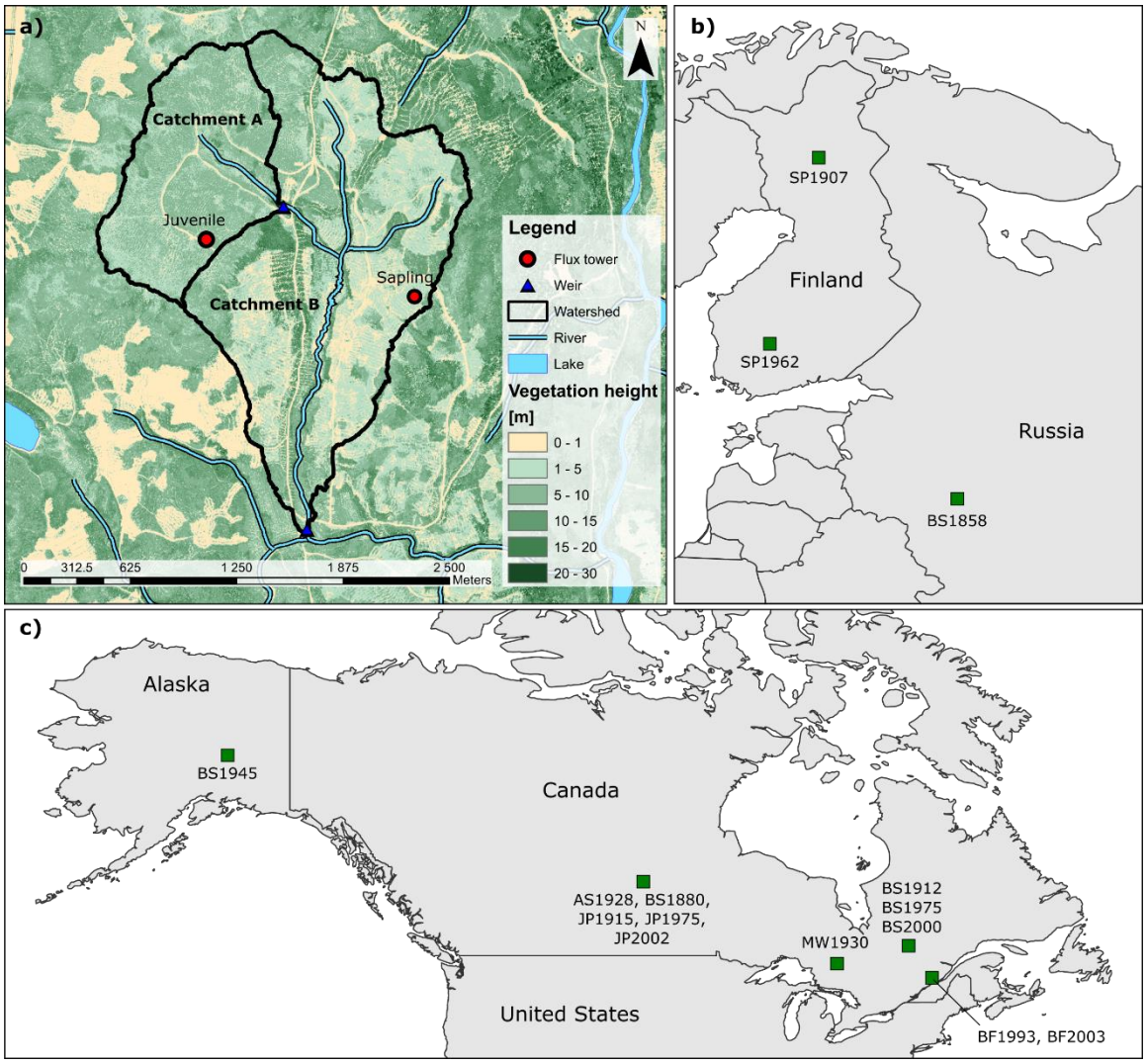

Figure 2.1: a) Location of instruments at the study site, with catchment boundaries and vegetation height from LiDAR surveys (Source: Ministère Forêts, Faune et Parcs du Québec); b) Location of European study sites; c) Location of study sites in North America.

The Montmorency Forest is under the influence of a continental subarctic climate (Köppen classification subtype Dfc) with a short and cool growing season and high volumes of year-round precipitation. Mean annual temperature is 0.5°C and mean annual precipitation amounts to 1583 mm (40% as snow) over the period of 1981-2010, as per Environment and Climate Change Canada (Station "Foret Montmorency", available at: http://climat.meteo.gc.ca/historical data/search historic data f.html).

2.4.2 Instrumental setup

Two flux towers were installed in the BEREV in October 2015: the Juvenile and Sapling flux towers (see Figure 2.1a). The Juvenile flux tower is a 15-m scaffolding structure featuring two sets of sonic anemometers and CO_2/H_2O gas analyzers (IRGASONs, Campbell Scientific, USA). The two devices are mounted 14.63 m

above the ground, or ≈8 m above the top of the canopy, and face opposite directions (303°, northwest; and 118°, southeast). This feature allows for optimal flux quality control, since wind interference by the tower structure and devices is avoided by combining both time series based on wind direction. Both devices were installed parallel to the local 12° northeast-facing slope. This alignment is required to apply the eddy-covariance method on sloped terrain (Turnipseed et al., 2002; Hammerle et al., 2007; Hiller et al., 2008; Goulden et al., 2012; Nadeau et al., 2013b; Stiperski & Rotach, 2016), as it weakens flow distortion (Geissbühler et al., 2000; Oldroyd et al., 2016).

The Sapling flux tower is a 10-m triangular tower with one eddy-covariance system (IRGASON, Campbell Scientific, USA) mounted at a height of 8.5 m, or ≈5 m above the canopy. As the tower is located on a plateau, the instrument was leveled. Measurements from all eddy-covariance systems were sampled at 10 Hz and logged separately on three CR3000 dataloggers (Campbell Scientific, USA).

The Juvenile and Sapling towers also featured measurements of net radiation and soil heat flux. Net radiation was measured with 4-component radiometers (CNR4, Kipp and Zonen, The Netherlands). At the Juvenile tower, two devices were mounted at 15 and 10 m above the surface and parallel to 12° northeast-facing slope to follow the inclination of the eddy-covariance systems (Nadeau et al., 2013a; Serrano-Ortiz et al., 2016). At the Sapling tower, one device was installed 7 m above the ground and leveled.

The flux towers were also equipped with general meteorological measurements. Air temperature and relative humidity were measured with standard probes (HC2S3 and HMP45C, Campbell Scientific, USA). The Juvenile tower included a profile of four probes installed at heights of 3.29, 5.68, 10.77 and 14.96 m above the ground. The Sapling tower featured one probe at 2.10 m. Wind speed and direction were measured using wind vanes (05103, RM Young, USA), namely, two of them were installed at the Juvenile tower at heights of 8.53 and 14.63 m above ground, while one was installed at 3 m above ground at the Sapling tower.

The Juvenile site also featured measurements of biomass temperature using a set of 39 thermistors (Omega Engineering, USA) placed in five trees around the flux tower (3 balsam firs, 1 white spruce and 1 white birch). Three thermistors were installed in each tree trunk (one in the center of the bole, one on the south side and one on the north side, both beneath the bark) at a height of 1.3 m. The temperature of the top portion of each tree trunk was also monitored with thermistors placed on the north and south sides beneath the bark at two-thirds of the tree height. 15 thermistors were installed in tree branches: either on the top of the lowest branches or on the bottom of the top branches, on the north and south sides of each monitored tree.

Total precipitation and complementary measurements of air temperature, relative humidity, and atmospheric pressure were measured at a station located ≈4 km north of the study sites and operated by the Québec

government (MELCC, 2019). To obtain the most accurate snowfall measurements, the site also had a Double-Fence Intercomparison Reference (DFIR, Pierre et al., 2019), which is the reference to avoid solid precipitation under-catch (Yang, 2014). Data are available and substituted to the regular station between November 1 and March 31 each year for the part of our analysis that focuses on the Montmorency Forest watershed budget (see section 2.7.2). We did not use DFIR data for the comparison between boreal sites (section 2.7.1), as the precipitation of the other sites were not corrected for undercatch. Discrepancies in measurements with and without undercatch corrections at Montmorency Forest are discussed in section 2.7.2.

The setup also includes discharge measurements, as illustrated in Figure 2.1a. Discharge were obtained using v-notch weirs also operated by the Québec government (Station 51004 and 51007, available at: https://www.cehq.gouv.qc.ca/hydrometrie/historique_donnees/). Daily mean runoffs were used in this study.

2.4.3 Data processing

Eddy-covariance raw 10-Hz measurements were processed using EddyPro©, version 6.0 (LI-COR Biosciences, USA). The procedure included linear detrending, correction of low-pass (Moncrieff et al., 1997) and high-pass (Moncrieff et al., 2004) filtering effects, covariance maximization, density fluctuations compensation with the Webb correction (Webb et al., 1980). Coordinate rotation of wind speed was performed using a sector-wise planar fit (Wilczak et al., 2001), since this procedure is recommended for eddy-covariance measurements on slopes (Ono et al., 2008; Oldroyd et al., 2016). Spikes, amplitude resolution artifacts, unrealistic drop-outs, outliers and discontinuities, as well as other artifacts were detected and removed using the statistical tests of Vickers & Mahrt (1997). Turbulent fluxes were computed using a 30-min averaging period. Errors associated with fluxes were quantified using the random uncertainty method of Finkelstein & Sims (2001).

Data runs during rainfall events were filtered out, because rain can obstruct the path of the open gas analyzer light signal. Periods when winds were blowing from a 90° sector centered on the back of the devices were also removed, as these conditions imply that the flow of air is distorted by the tower structure. Poor data quality was assessed and removed using the 0-1-2 criteria of Mauder & Foken (2011). Periods when turbulent fluxes largely violated the energy budget (*i.e.*, $H + L_vE > 5R_n$) were discarded. Filtering was completed by a meticulous visual inspection to detect and remove periods of clear malfunction. This rigorous filtering procedure removed ≈35% and ≈50% of data segments for H and L_vE, respectively, for both sites between 2016 and 2018 inclusively.

For the Juvenile site, time series of fluxes from both eddy-covariance setups were combined using wind direction. To further complete these time series, the Juvenile and Sapling fluxes were gap-filled using marginal

distribution sampling (MDS) as described in Reichstein et al. (2005) (see their Appendix A and Figure A1), as recommended by Moffat et al. (2007). This procedure left only ≈5% and ≈20% of missing data for H and L_vE, respectively. Remaining gaps were filled with monthly linear regression with zero-set origin between fluxes and net radiation.

As was the case for eddy-covariance data, all complementary meteorological and biomass temperature measurements were subjected to a rigorous filtering procedure that began with a careful visual inspection to detect clear periods of malfunction. Some meteorological variables received specific filtering procedures. Shortwave downwelling radiation was capped by maximum theoretical values calculated following Whiteman & Allwine (1986). For every temperature-humidity sensor, humidity values were capped using temperature-dependent maximum humidity.

For every variable, gap-filling was performed by merging time series from different devices with monthly linear regressions using a clear step-by-step procedure: (i) a variable is filled with other on-site devices by order of proximity; (ii) variables are next filled with the other site similar devices; and (iii) the few remaining gaps are completed with data from the nearby governmental station.

Soil heat fluxes were measured with soil heat flux plates, but energy storage above the plates (ΔQ_G [W m^{-2}]) was also calculated and included in G. They were obtained from the standard calorimetric method (Ochsner et al., 2007):

$$\Delta Q_G = c_{p,s} \frac{\Delta T_s}{\Delta t} \Delta z \tag{2.3}$$

where ΔT_s [K] is the difference in soil temperature T_s between two time steps of length Δt [s]; Δz [m] is the soil layer thickness between the plates and the surface; and $c_{p,s}$ [J m^{-3} K^{-1}] is the specific heat of the soil, taken as:

$$c_{p,s} = c_{p,s,dry} + c_{p,water}\theta \tag{2.4}$$

where $c_{p,s,dry}$ and $c_{p,water}$ are values taken from the literature for a sandy loam and for water (1.28×10^6 and 4.184×10^6 J m^{-3} K^{-1}, respectively; Van Wijk, 1963) and θ [m^3 m^{-3}] is the volumetric water content of the soil.

Soil heat flux plates were subject to very frequent malfunctions. Fortunately, ΔQ_G measurements were almost continuous once on-site time series were merged, and correlation between soil heat flux plates measurements and ΔQ_G were high (R^2 between 0.7 and 0.9). Missing G values were obtained using a monthly linear regression with ΔQ_G.

To account for the measurement height of the eddy-covariance systems, storage fluxes of sensible heat and latent heat (ΔQ_H and ΔQ_{LvE}) were also evaluated at each station using the method of Aubinet et al. (2001):

$$\Delta Q_H = \sum_{i=1}^{4} c_{p,i}\rho_i \frac{\Delta T_i}{\Delta t}\Delta z_i \tag{2.5}$$

$$\Delta Q_{LvE} = \sum_{i=1}^{4} L_{v,i}\rho_i \frac{\Delta q_i}{\Delta t}\Delta z_i \tag{2.6}$$

where subscript i applies to the four (one) measurement height for each variable of the Juvenile (Sapling) station; ΔT_i [K] and Δq_i [kg kg^{-1}] are the differences in T or q at height i between two time steps of length Δt [s]; and Δz_i [m] is the air layer thickness associated with each measurement probe. For the Juvenile station, Δz_i is 4.49 m, 3.74 m, 4.64 m and 1.50 m from bottom to top probe, respectively, while Δz is the measurement height (8.5 m) for the Sapling station.

Biomass heat storage (ΔQ_B) was computed for specific portions (upper and lower trunk, branches, needles or leaves) of each monitored tree using vegetation temperature measurements and the following general formula (Oliphant et al., 2004):

$$\Delta Q_{veg} = m_{veg} c_{p,veg} \frac{\Delta T_{veg}}{\Delta t} \tag{2.7}$$

where ΔQ_{veg} [W] is a heat storage within a specific tree portion; m_{veg} [kg] is its mass [kg]; $c_{p,veg}$ is its heat capacity [J kg^{-1} K^{-1}]; and ΔT_{veg} is the temperature variation during a time step of length Δt.

Specific properties of the trees were obtained from USDA (2007). Tree trunk portions were approximated as cylinders, and bulk temperature variations of the upper and lower trunks as a whole were calculated using the method outlined in Garai et al. (2010). Branch and needle temperatures were taken as the average of branch thermistors. Branch mass was calculated using surveyed branch density with height and assuming that branch length decreases linearly from the bottom branches to the top of the tree. Needle mass was calculated using the empirical functions of Ter-Mikaelian & Korzukhin (1997). ΔQ_B was then taken as the sum of ΔQ_{veg} values from trunk, branch and needle for each tree species (the three balsam firs were averaged), and multiplied by species-specific stem densities surveyed around the flux tower (balsam fir: 0.26 m^{-2}; white spruce: 0.01 m^{-2}; white birch: 0.003 m^{-2}). Missing ΔQ_B values were filled with monthly linear regression with zero-set origin between heat storage and net radiation.

2.5 Comparison Sites

The energy budgets of the Montmorency Forest sites were compared to those of 15 sites located in the boreal forest that are described in Table 2.1. Data from European (BS1858, SP1907, SP1962) and United States (BS1945) sites were obtained from the Fluxnet 2015 dataset (available at: https://fluxnet.fluxdata.org), while data from Canadian sites were part of the FLUXNET Canada Research Network Canadian Carbon Program Data Collection, 1993-2014 (FLUXNET–Canada, 2016). Note that the Juvenile and Sapling sites are also featured in Table 2.1 as sites BF1993 and BF2003, respectively.

The sites used for comparisons are spread all across the circumpolar boreal biome and include most of the usual trees found in these regions at different stages of maturity. Annual averages of temperature are relatively constant throughout the sites, with variations between -2.0°C in Alaska (BS1945) and 3.9°C in Russia (BS1858). Climatological averages of annual cumulative precipitation vary greatly across sites, from the very dry Alaskan site (275 mm y^{-1}) to the humid sites of eastern Canada (MW1980 at 831 mm y^{-1}; BS1912, BS1975 and BS2000 at 961 mm y^{-1}), culminating at the main study sites in the Montmorency Forest receiving an average of 1583 mm y^{-1}.

Table 2.1 also presents the main references for each study site, in which instrumental setups are described. All sites featured standard eddy-covariance systems installed following diligent procedures. Data from the Fluxnet 2015 dataset was processed following methods outlined at https://fluxnet.fluxdata.org/data/fluxnet2015-dataset/data-processing/: every variable is rigorously quality-checked (Pastorello et al., 2014), meteorological variables are gap-filled using ERA-Interim reanalysis (Vuichard & Papale, 2015), while turbulent fluxes are gap-filled with the standard MDS procedure (Reichstein et al., 2005). The FLUXNET–Canada (2016) dataset was processed following similar procedures described in Papale & Valentini (2003); Reichstein et al. (2005); Papale et al. (2006); Moffat et al. (2007).

In this study, we first present the fluxes that were uncorrected for energy balance closure (see section 2.7.1.1). To account for missing flux values at each site, we linearly scaled monthly sums of energy; multiplying the latter by the ratio of total number of periods in a given month over periods of available data in the same month. Note that this procedure was also applied for annual sums of E and P.

Table 2.1: Description of the study sites. Site IDs are generated with main tree species at the site (first two letters) and approximate year of the last on-site disturbance, when vegetation started to grow back (last four numbers). LAI is the leaf area index at the start of the site study period, while GS is the average growing season length in days [d], calculated using the method of Bergeron et al. (2007). *T* and *P* are climatological averages of *T* and *P* on an annual basis. Age of tree stand is at the start of the site study period, described in the "Study years" column.

Site ID	Location	Coordinates	Altitude [m AMSL]	Vegetation (Age [y])	LAI [m^2 m^{-2}]	Study years	GS [d]	*T* [°C]	*P* [mm]	Reference
AS1928	Saskatchewan, Canada	53.63°N; 106.20°W	601	Aspen (70)	3.8	1997-2000; 2002-2010	227	0.4	467	Blanken et al. (1998)
BF1993	Québec, Canada	47.29°N; 71.17°W	855	Balsam Fir (25)	3.4	2016-2018	198	0.5	1583	Isabelle et al. (2018)
BF2003	Québec, Canada	47.29°N; 71.15°W	805	Balsam Fir (10)	2.9	2016-2018	199	0.5	1583	This study
BS1858	Fyodorovskoye, Russia	56.46°N; 32.92°E	265	Black Spruce (140)	3.5	1999-2012	268	3.9	711	Kurbatova et al. (2008)
BS1880	Saskatchewan, Canada	53.99°N; 105.11°W	629	Black Spruce (120)	5.6	2001-2010	216	0.4	467	Jarvis et al. (1997)
BS1912	Québec, Canada	49.69°N; 74.34°W	382	Black Spruce (95)	4.0	2005-2009	221	0.0	961	Bergeron et al. (2007)
BS1945	Alaska, USA	65.12°N; 147.49°W	210	Black Spruce (65)	0.7	2011-2012; 2014	173	-2.0	275	Ikawa et al. (2015)
BS1975	Québec, Canada	49.76°N; 74.57°W	385	Black Spruce (35)	3.5	2008-2010	233	0.0	961	Payeur-Poirier et al. (2012)
BS2000	Québec, Canada	49.27°N; 74.04°W	415	Black Spruce (5)	1.6	2005-2010	225	0.0	961	Giasson et al. (2006)
JP1915	Saskatchewan, Canada	53.92°N; 104.69°W	579	Jack Pine (90)	2.0	2004-2009	215	0.4	467	Baldocchi et al. (1997)
JP1975	Saskatchewan, Canada	53.88°N; 104.65°W	534	Jack Pine (30)	3.1	2005-2006	205	0.4	467	Mkhabela et al. (2009)
JP2002	Saskatchewan, Canada	53.94°N; 104.65°W	520	Jack Pine (5)	0.2	2005-2007	207	0.4	467	Mkhabela et al. (2009)
MW1930	Ontario, Canada	48.22°N; 82.16°W	340	Mixed Forest (75)	4.1	2006-2013	240	1.3	831	McCaughey et al. (2006)
SP1907	Sodankylä, Finland	67.36°N; 26.64°E	179	Scots Pine (110)	3.8	2003-2004	208	-0.4	527	Thum et al. (2007)
SP1962	Hyytiälä, Finland	61.85°N; 24.29°E	181	Scots Pine (35)	7.9	1997-2010	276	2.9	709	Suni et al. (2003)

This study also presents annual sums of E as components of the water budget at each site. However, every site experiences non-closure of the energy budget on a yearly basis (see section 2.7.1.1). Energy budget imbalance is a common problem with studies using eddy-covariance fluxes (*e.g.*, Baldocchi et al., 1997; Barr et al., 2001; 2006; Foken et al., 2010; Isabelle et al., 2018b), where the technique measures smaller turbulent fluxes (H+ L_vE) than the available energy (R_n−G−ΔQ). Probable causes behind this anomaly are well-described by Foken (2008), Leuning et al. (2012), and Stoy et al. (2013), among others. The consequence of this imbalance is that uncertainties are associated with E measurements, which are probably underestimated at all sites. For this reason, annual sums of E have to be corrected in water balance studies (Wohlfahrt et al., 2010).

In the present study, closure fraction (CF) was evaluated as the annual sums of turbulent fluxes (H+ L_vE) divided by the annual sums of available energy (R_n− G − ΔQ). However, precise and accurate measurements of G and ΔQ were not available at all sites: to be consistent for the sake of site comparison, we computed annual sums of available energy using only R_n. The relevance of this assumption is discussed in section 2.7.1.1. Annual E was then obtained by dividing measured annual E by annual CF, a method that preserves the Bowen ratio, *i.e.* the proportion of H to L_vE (Blanken et al., 1997; Twine et al., 2000; Wohlfahrt et al., 2010). This energy imbalance correction method was successfully applied in a hydrological study of the BOREAS region, in the Western Great Plains of Canada (Barr et al., 2012), and deemed appropriate to account for the underestimation of E in eddy-covariance measurements (Mauder et al., 2018).

2.6 Potential evapotranspiration calculation

This study focused on the effect of high precipitation on E, as it is viewed as a good proxy for water availability that can constrain land-atmosphere exchanges of water. However, to put comparison sites in perspective, it is also important to quantify site-specific values of the energy available for E and the potential water vapor content of the atmosphere. These concepts are well-described using potential evapotranspiration (E_p).

To evaluate E_p, we used the formula developed by Penman (1948). This equation was originally devised to quantify evaporation from an open-water surface, but it can also apply to saturated land surfaces. It combines energy-balance and mass-transfer approaches to evaluate E_p from available energy (R_n) and from atmospheric vapour deficit, which determines drying power of the air (ϕ). The equation goes as follows:

$$E_p = \frac{1}{L_v}\left[\frac{\Delta_e}{(\Delta_e+\gamma)}R_n + \frac{\gamma}{(\Delta_e+\gamma)}\phi\right] \quad (2.8)$$

where E_p [kg m^{-2} s^{-1}] is the potential water vapor flux; L_v [J kg^{-1}], the latent heat of vaporisation of water; Δ_e [Pa K^{-1}], the slope of saturation vapour pressure versus temperature curve; γ [Pa K^{-1}], the psychrometric constant; R_n [W m^{-2}], the net radiation; and ϕ [W m^{-2}], the drying power of the air defined by Katul & Parlange (1992) as:

$$\phi = \frac{c_p \kappa^2 \rho U D}{\gamma \ln\left(\frac{z_v - d_0}{z_{0v}}\right) \ln\left(\frac{z_m - d_0}{z_{0m}}\right)} \tag{2.9}$$

where c_p [J kg^{-1} K^{-1}] is the specific heat of the humid air; κ, the von Kármán constant (≈ 0.4); ρ [kg m^{-3}], the humid air density; U [m s^{-1}], the mean wind velocity measured at height z_m [m]; D [Pa], the vapor pressure deficit measured at height z_v [m]; γ [Pa K^{-1}], the psychrometric constant; z_{0m} and z_{0v} [m], the roughness lengths for momentum and humidity, respectively; d_0 [m], the zero-plane displacement height. d_0, z_{0m}, and z_{0v} are estimated with the site-specific mean vegetation height (h_v) as (2/3)h_v, 0.1h_v, and 0.01h_v, respectively (Brutsaert, 1982; 2005).

Note that this evaluation of E_p is a theoretical upper bound: in reality, soil heat fluxes (G), and heat storage in biomass and air below measurement devices (ΔQ) should be subtracted from R_n to obtain available energy. Unfortunately, as was previously mentioned, these energy budget terms were not available at every comparison site. To preserve consistency between measurement sites and be consistent with E adjustments for closure fraction, we decided to compute E_p using only R_n, while noting that this probably results in an overestimation of E_p.

2.7 Results and Discussion

2.7.1 Comparison between boreal forest sites

2.7.1.1 Energy budget

Figure 2.2 presents annual cycles of monthly-averaged energy budget terms for each study site, for daytime periods only (R_n > 0), as it is when the majority of fluxes occur. Each plot includes one curve for each term per study year to outline interannual variability. Note that H and L_vE are here shown without energy imbalance correction. All study sites are characterized by classical net radiation curves culminating during (Northern Hemisphere) summer months, with obviously a very slight tendency towards higher values at southernmost latitudes (*e.g.*, SP1907 at 67.36°N has maximum R_n ≈ 400 W m−2 vs. SP1962 at 61.85°N has maximum R_n ≈ 455 W m−2). All sites share similar annual trends: spring increases in Rn are counterbalanced by increasing

H at first, but L_vE fluxes eventually rise around June when the growing season (and transpiration) blooms. The main difference between sites lies in the magnitude of summer L_vE peaks and the proportion of R_n they account for.

Two behaviours are exhibited in Figure 2.2: pine stands (JP1915, JP1975, JP2002, SP1907, and SP1962) and some black spruce stands (BS1858, BS1880, BS1912, and BS1945) see L_vE increasing in the summer without usually exceeding *H*, while other sites show a clear dominance of L_vE in the energy budget at the summer onset of transpiration. These discrepancies can stem from three plausible sources: (i) tree species; (ii) age of the tree stand; and (iii) meteorological conditions governing direct water and energy availability. The first two sources represent land surface conditions including soil type and moisture conditions.

Differences in energy budget across tree species are clear: stands including a large proportion of deciduous species (AS1928 and MW1930) exhibit a more pronounced summer peak in L_vE, the upward inflection point coinciding with leaf emergence. Balsam firs and black spruces usually thrive in wet environments and generate substantial L_vE given adequate water availability (McCaughey, 1978b; Nijssen & Lettenmeier, 2002). On the contrary, pine stands grow in sandy well-drained soil and consequently produce lower L_vE fluxes (Nijssen & Lettenmeier, 2002; Mkhabela et al., 2009).

Pine stands appear to generate similar L_vE fluxes at different stages of maturity, as seen by comparing SP1907 with SP1962 or JP1915 with JP1975 and JP2002. The same can be said of balsam firs (BF1993 and BF2003), but black spruce stands from eastern Canada feature some differences. Indeed, the mature black spruces of BS1912 generate a notably lower summer peak of L_vE compared to the juvenile stands of BS1975 or the saplings of BS2000. This behaviour is more thoroughly inspected in the next section.

All surveyed sites are subject to non-closure of the annual energy budget. Closure fraction (*CF*) varies between 0.50 and 0.99, while the interannual site averages vary between 0.69 (BS1945) and 0.90 (JP1915). Wherever the inclusion of other important energy budget terms such as *G* and/or ΔQ was possible, yearly values of *CF* did not improve much, with variations between -0.01 and 0.08 and an average variation of 0.01. For this reason, it seems that adjusting annual *E* values for energy budget closure using only R_n as available energy is a reasonable decision. It creates minimal uncertainties in yearly *CF*, and hence yearly *E*, and it is the most coherent procedure to apply to all sites.

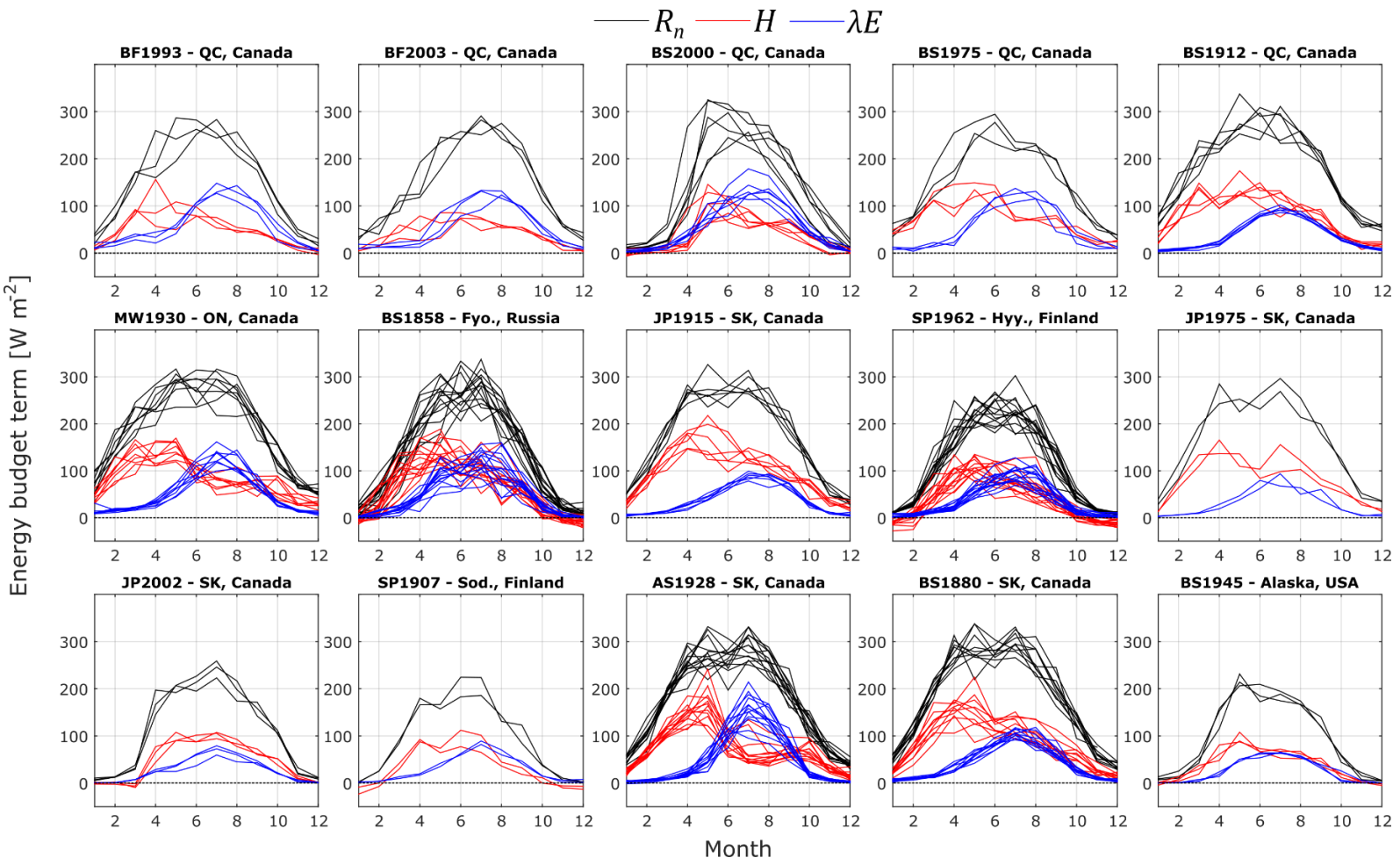

Figure 2.2: Annual cycles of monthly averaged (daytime only) net radiation (R_n) and sensible and latent heat fluxes (H and L_vE, uncorrected for energy imbalance) for all study sites, including only daytime observations, defined as when $R_n > 0$.. Each graph features one curve per study year for each variable. Sites are ordered by annual cumulative precipitation, from the site receiving most precipitation (BF1993) to the site receiving the least (BS1945).

2.7.1.2 Evapotranspiration and precipitation

Yearly-scale variations of E and P as well as site-dependent evaporative demands (E_p) are outlined in Figure 2.3 and described in details in Table 2.2. All values of E are corrected for energy imbalance. These results bring forward the trends outlined in the previous section: sites with higher summer peaks of L_vE (AS1928, BF1993, BF2003, BS1975, BS2000, and MW1930) evidently are the sites enduring the strongest yearly E rates. The latter fluctuate amongst sites, from 194 mm y^{-1} for JP2002 to 446 mm y^{-1} at the Montmorency Forest juvenile balsam fir stand (BF1993).

Precipitation rates, as a proxy of water availability, appear very influential in the distribution of E rates, as can be seen in Table 2.2. Montmorency Forest sites (BF1993 and BF2003) clearly stand out as the sites receiving the most precipitation by a large margin, and consequently returning the greatest amount of water back to the atmosphere. In general, ranking sites by E rates or by P rates yields similar results, aside from some notable outliers. For example, AS1928 and BS1880 evaporate 422 and 383 mm y^{-1}; good for 7^{th} and 9^{th} rank by E, respectively, despite receiving the second and third lowest yearly precipitation. These sites are however characterized by strong energy inputs, as demonstrated by their very high E_p rates (2014 and 1806 mm y^{-1}, good for 2^{nd} and 5^{th} rank by E_p, respectively). Note that these findings stand with or without energy imbalance corrections. Such similarities between ranks are not visible when ranking sites by E and E_p, which seems to imply that boreal forest E strongly depends on water availability.

However, there is an intricate relationship between E, water availability (P) and evaporative demand (E_p). Figure 2.4 summarizes that relationship for each study site, that is: yearly-summed evaporative index (E/P) as a function of yearly-summed aridity index (E_p/P). The figure emulates the classical Budyko framework (Budyko, 1958, 1974), but note that this framework usually applies to climatologic rather than yearly averages (Gentine et al., 2012). The Montmorency Forest sites again stand out (blue circles and triangles): the sites have very low values of evaporative index and the lowest values of aridity index. Even if they generate the largest yearly evaporative rates, the important precipitation still outweighs evaporative losses by a lot. Recurring precipitation also decreases sun exposure and increase air humidity, which limits the potential to evaporate, indicating that water availability is rarely an issue.

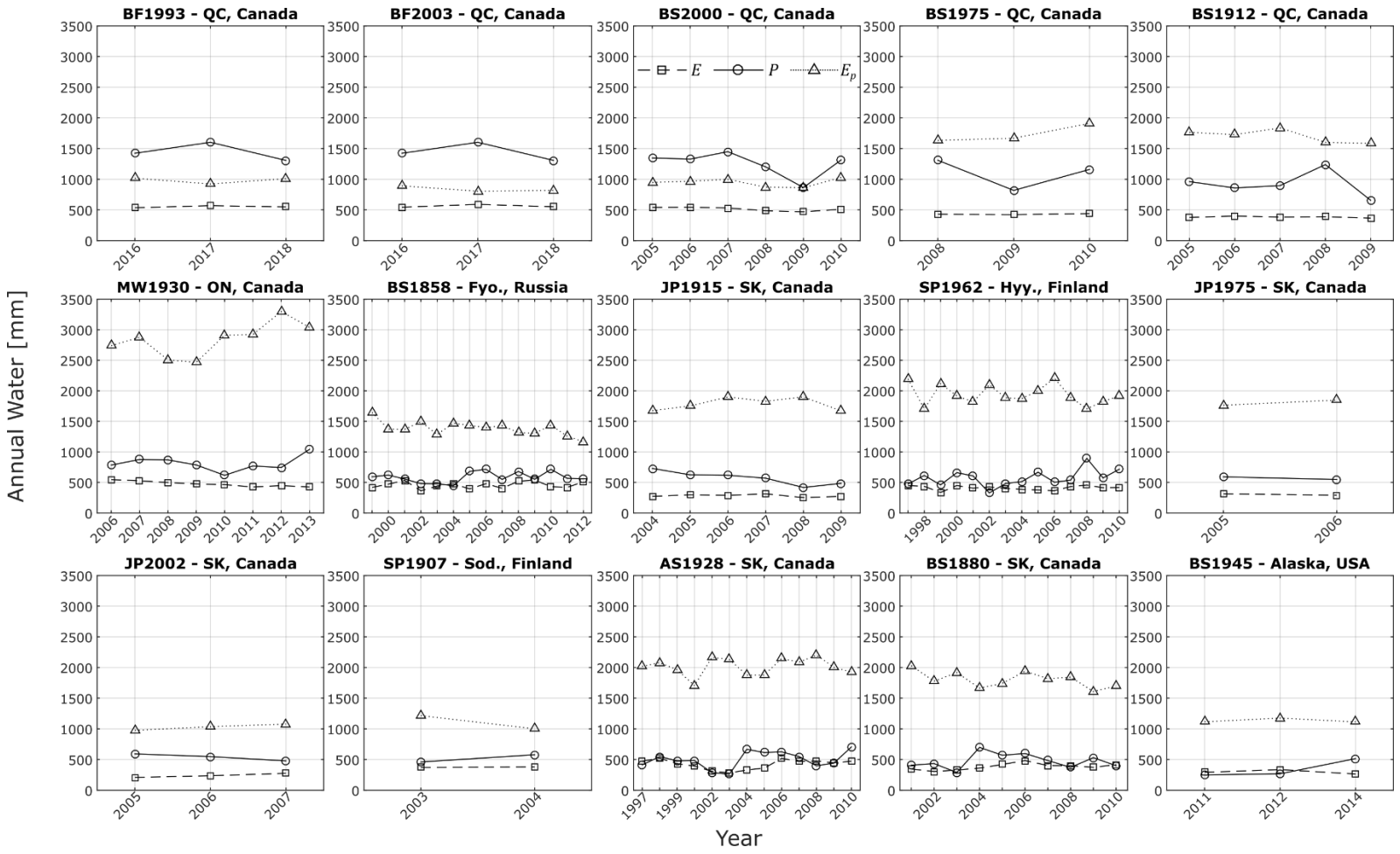

Figure 2.3: Interannual variations of annual cumulative precipitation *P* (full lines with circles), potential evapotranspiration E_p (dotted lines with triangles) and evapotranspiration *E* (dashed lines with squares) for each study site. Cumulatives are adjusted to account for missing values (see section 2.5). Sites are placed by annual precipitation rate ranking, from the site receiving most precipitation (BF1993) to the site receiving the least precipitation (BS1945).

Table 2.2: Interannual averages ± standard deviations of E, E^* (uncorrected for energy imbalance), P and E_p for each study site, for the number of years in the second column. P_{clim} is the climatological average of precipitation (from Table 2.1). Sites are ordered by annual precipitation rate, from the site receiving the most precipitation (BF1993) to the site receiving the less precipitation (BS1945).

Site ID	# of years	P_{clim} [mm y^{-1}]	E [mm y^{-1}]	E^* [mm y^{-1}]	P [mm y^{-1}]	E_p [mm y^{-1}]
BF1993	3	1583	552 ± 17	446 ± 33	1444 ± 149	983 ± 52
BF2003	3	1583	562 ± 25	403 ± 55	1444 ± 149	839 ± 47
BS2000	6	961	514 ± 31	425 ± 40	1251 ± 205	946 ± 68
BS1975	3	961	431 ± 9	382 ± 9	1096 ± 252	1737 ± 151
BS1912	5	961	383 ± 12	286 ± 13	922 ± 211	1703 ± 108
MW1930	8	831	476 ± 45	380 ± 44	811 ± 123	2845 ± 274
BS1858	14	711	457 ± 55	300 ± 48	585 ± 87	1384 ± 117
JP1915	6	467	283 ± 22	253 ± 15	574 ± 110	1788 ± 105
SP1962	14	709	411 ± 35	353 ± 51	574 ± 137	1940 ± 163
JP1975	2	467	303 ± 16	194 ± 25	569 ± 31	1806 ± 59
JP2002	3	467	240 ± 33	276 ± 11	539 ± 57	1030 ± 51
SP1907	2	527	375 ± 5	311 ± 22	536 ± 52	1012 ± 102
AS1928	13	467	422 ± 79	218 ± 1	498 ± 138	2014 ± 142
BS1880	10	467	383 ± 52	370 ± 59	479 ± 116	1806 ± 126
BS1945	3	275	297 ± 36	202 ± 8	344 ± 149	1135 ± 36

Figure 2.4 displays an obvious trend amongst study sites: increasing the aridity index usually results in larger evaporative indexes, *i.e.*, the more arid the environment, the greater the proportion of P that is returned to the atmosphere. Note that the featured linear regression is statistically significant (p-value < 0.05). If we rearrange the linear regression equation, we obtain that $E = 0.12E_p + 0.31P$. This equation cannot be used single-handedly as a model for predicting annual E, but it outlines nicely the contribution from evaporative demand (E_p) and water availability (P) to E in boreal forests of the world. It also corroborates previous results that seem to point out to a slightly larger impact of water availability, or precipitation, to annual E. These trends are similarly visible when using E without energy imbalance corrections (not shown). Figure 2.4 also depicts the large interannual variability of most sites as well as uncertainty issues regarding the estimation of E and E_p, *e.g.*, E/P are above 1 in some situations.

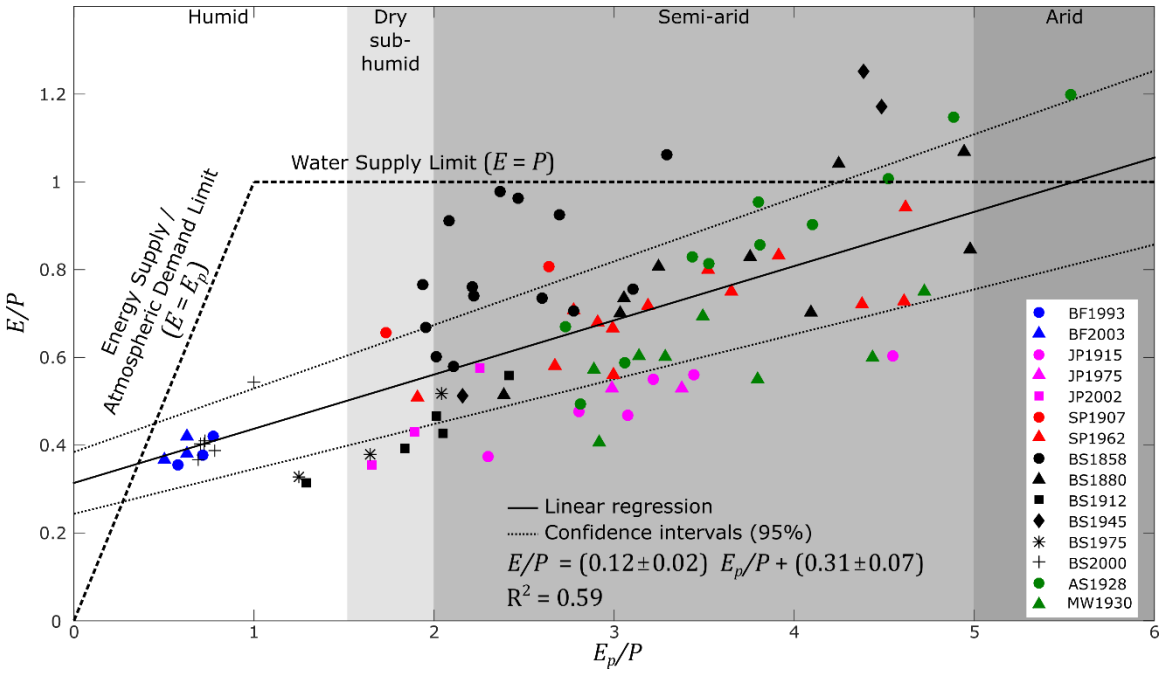

Figure 2.4: Evaporative index (evapotranspiration divided by precipitation *E/P*) vs. aridity index (potential evapotranspiration divided by precipitation E_p/P) for each study site. Each point represent one study year annual sums of *E*, *P* and E_p. Dashed lines show the demand limit (maximum possible *E* based on energy supply / atmospheric demand) and water supply limit (maximum *E* based on available water). Solid line is a least-squared linear regression with coefficients and R^2 introduced at the bottom of the graph, while dotted lines are the 95% confidence intervals lines corresponding to errors in linear regression coefficients.

We used multiple linear regressions to isolate the primary controls on annual evapotranspiration. The latter, for all sites and measurement years, was taken as the response variable, with predictors being annual precipitation (*P* [mm]), annual potential evapotranspiration (E_p [mm]), latitude (φ [°]), altitude (*z* [m]), and stand age (*A* [y]). The model took the following form:

$$E = 170\ \text{mm} + 0.21\frac{\text{mm}}{\text{mm}}P + 0.02\frac{\text{mm}}{\text{mm}}E_p + 0.73\frac{\text{mm}}{^\circ}\varphi - 0.04\frac{\text{mm}}{\text{m}}z + 0.49\frac{\text{mm}}{\text{y}}A \qquad (2.10)$$

and had an R^2 value of 0.40 while being statistically significant (p-value < 0.05). Interestingly, only *P* and *A* were significant contributors to the model (p-value < 0.05). These results highlight the high importance of annual precipitation on annual evapotranspiration. In addition, they identify stand age as an important predictor for annual *E*. Observations point towards minimal influences of latitude, altitude, and (more surprisingly) potential evapotranspiration. Latitude and annual precipitation are linked (R^2 = 0.37, p-value < 0.05) but not altitude and annual precipitation, primarily because all Saskatchewan sites (AS1928, BS1880, JP1915, JP1975, and JP2002) have relatively high altitude (~565 m AMSL) and low precipitation.

The analysis was repeated species by species, whenever the number of data points allowed for it (*i.e.* not for balsam firs only and jack pines only; grouping aspens with mixed woods as "deciduous"; and grouping jack pines with scots pines as "pines"). Table 2.3 presents the coefficient of determination for each of these subset models, along with the associated p-values.

Table 2.3: Summary of multiple linear regressions results. Coefficient of determination R^2 are shown for models found for each groups of study sites. p-values indicate the significance level of each variables in the model: values in bold are significant at the 5% confidence level. Dashes indicate that the intercept value of the particular model was zero. Whenever a model has no significant contributing variable, the one with lowest p-value is in italics.

		p-value					
Groups	R^2	Intercept	P	E_p	φ	z	A
All	0.40	0.41	**0.00**	0.20	0.78	0.49	**0.01**
Deciduous	0.24	-	*0.18*	0.77	0.27	0.71	0.47
Conifers	0.53	0.72	**0.00**	0.43	0.29	0.21	**0.00**
Black Spruce	0.55	**0.00**	0.14	**0.00**	0.06	0.82	**0.00**
Scots Pine	0.32	-	0.54	*0.37*	0.96	0.75	0.52
Pines	0.85	0.55	*0.12*	0.34	0.80	0.22	0.58

These results show quite well that annual precipitation is commonly a driving factor in annual evapotranspiration, except maybe for Scots pines, which is mostly the SP1962 site. Stand age is the second most important variable: particularly for black spruces. Potential evapotranspiration is particularly influential for black spruces, and mildly for Scots pines and pines in general. Latitude and altitude again do not appear to be of influence.

As was described in section 2.6, E_p combines the effects of available energy, air humidity and atmospheric water vapor holding capacity to obtain maximum possible E. In Table 2.4, we quantify these effects by computing linear regressions between monthly summed E and monthly summed R_n or monthly averaged D (vapor pressure deficit) for all study site. Results show that R_n and D are important drivers of E: R_n explains between 60% and 89% of E variance, while D explains between 62% and 94% of E variance. All described linear regressions and correlations are statistically significant (p-value < 0.05), and these results are also observed with E uncorrected for energy imbalance (not shown). Similar results were obtained by Brümmer et al. (2012) for various Canadian sites (including AS1928, BS1880, BS1912, JP1915, and MW1930).

For most sites, correlation between E and D is close to or higher than correlation between E and R_n. BS1858 is the outlier, with R^2 values at 0.82 and 0.62 for linear regressions between E and R_n or D, respectively. Conifer-dominated sites in Saskatchewan exhibit smaller $E - D$ and $E - R_n$ slopes than other sites, highlighting their tendency to limit E under low water availability conditions, even in times of high evaporative demand.

Table 2.4: Linear regression parameters (slope and intercept, with 95% confidence intervals) and coefficient of determination (R^2) between monthly summed E and: (i) monthly summed net radiation R_n; and (ii) monthly average 24-h vapour pressure deficit D.

Site ID	E vs. R_n			E vs. D		
	Slope [mm/(MJ m^{-2})]	Intercept [mm month^{-1}]	R^2	Slope [mm/Pa]	Intercept [mm month^{-1}]	R^2
AS1928	0.22 ± 0.03	0.30 ± 6.17	0.61	0.12 ± 0.01	-8.53 ± 6.37	0.66
BF1993	0.19 ± 0.05	13.46 ± 11.99	0.60	0.18 ± 0.04	8.32 ± 10.06	0.74
BF2003	0.25 ± 0.05	6.04 ± 9.85	0.77	0.19 ± 0.04	8.88 ± 10.57	0.72
BS1858	0.22 ± 0.02	1.16 ± 3.68	0.82	0.12 ± 0.01	4.58 ± 5.41	0.62
BS1880	0.15 ± 0.02	2.61 ± 4.41	0.72	0.09 ± 0.01	-0.03 ± 3.46	0.83
BS1912	0.16 ± 0.03	-0.16 ± 7.30	0.67	0.10 ± 0.01	2.50 ± 4.18	0.86
BS1945	0.15 ±0.02	5.04 ± 3.98	0.89	0.10 ± 0.01	-5.32 ± 5.39	0.87
BS1975	0.21 ± 0.04	-1.17 ± 9.61	0.74	0.13 ± 0.02	1.31 ± 7.39	0.82
BS2000	0.22 ± 0.02	8.43 ± 5.25	0.84	0.13 ± 0.01	0.40 ± 6.11	0.83
JP1915	0.12 ± 0.02	4.17 ± 4.48	0.66	0.07 ± 0.01	-0.51 ± 3.26	0.84
JP1975	0.15 ± 0.04	1.21 ± 8.28	0.75	0.08 ± 0.02	-2.90 ± 7.93	0.80
JP2002	0.13 ± 0.02	5.49 ± 3.19	0.87	0.06 ± 0.01	-1.64 ± 2.62	0.94
MW1930	0.20 ± 0.03	-0.90 ± 6.99	0.68	0.11 ± 0.01	0.29 ± 6.28	0.72
SP1907	0.18 ± 0.04	6.94 ± 8.74	0.77	0.13 ± 0.03	3.86 ± 8.00	0.82
SP1962	0.20 ± 0.01	5.09 ± 3.06	0.82	0.12 ± 0.01	1.08 ± 3.46	0.80

We must remind readers that E_p values calculated in this study are considered to be upper bounds, since the available energy used in the Penman formulation includes only R_n without G and ΔQ. However, as was seen in section 2.7.1.1, differences in available energy following the inclusion of G and/or ΔQ are fairly inconsequential on an annual basis. Plus, Penman E_p formulation in that form seems to include the proper drivers to describe E in the boreal forest, as E and E_p are highly correlated at all sites (R^2 between 0.50 and 0.89, average at 0.72).

This above analyses were performed using the simplest energy budget closure adjustment for E. Indeed, multiplying E by $1/CF$ preserves the Bowen ratio (H/L_vE) for missing fluxes, but studies have demonstrated that this can induce an overcorrection (*e.g.*, Mauder et al., 2018). Nevertheless, such variation in the Bowen ratio are probably site-dependent, meaning that the attribution of site-specific proportion of Bowen ratio for missing flux values could increase uncertainties in E. Note that all result-based conclusions in this section remain viable when using E uncorrected for energy imbalance.

Precipitation totals presented in this section are also tainted by probable uncertainties related to the common wind-induced undercatch problem, particularly with solid precipitation. However, these uncertainties depend on wind speed, and the latter does not vary much between sites (site-averaged wind speeds are between 1.72 and 3.48 m s^{-1}). Furthermore, differences in wind speed are more related to each site measurement height than

actual differing wind regimes. Since every site team was aware of the undercatch problem, every instrument deployment was done following diligent procedures (shielded gauges installed at ground-level in wide forest clearings). Considering these precautions as well as likely similar uncertainties between sites, we believe our results still stand.

Despite the aforementioned limitations, this section has thoroughly demonstrated that the Montmorency Forest is receiving the highest cumulative precipitation of all surveyed sites, by a fair margin. But much higher P does not fully translate into much higher E. To put this in perspective, E values go from 240 mm y^{-1} (JP2002) to 562 mm y^{-1} (BF2003), an increase by a factor 2.34, while P values go from 344 mm y^{-1} (BS1945) to 1444 mm y^{-1} (BF1993, BF2003), an increase by a factor 4.20. It appears that E has a maximum value (or an upper physical limit), a result observed before in the boreal forest (Brümmer et al., 2012), but not necessarily elsewhere (Zhang et al., 1999). Reasons behind this behaviour could be physiological (ecosystem limit) and/or meteorological (*e.g.*, limited net radiation due to high cloud cover or/and an important atmospheric moisture convergence), but more studies are needed to elucidate this feature. Nevertheless, the Montmorency Forest stand-scale water budget definitely generates an excess of water that can substantially recharge groundwater storage or create strong runoffs.

2.7.2 Water allocation of a humid boreal forest

The Montmorency Forest sites are ideal to ascertain the effects of high annual precipitation on boreal forest water budgets. Figure 2.5 presents cumulative curves of every measured water budget components for catchment AB. E is a weighted combination of measurements at the Juvenile and Sapling flux towers ($E_{AB} = (A_A/A_{AB})E_{Juvenile} + (A_B/A_{AB})E_{Sapling}$), where A_A, A_B and A_{AB} are the areas of catchments A, B and AB, respectively). $E_{Juvenile}$ and $E_{Sapling}$ are corrected for non-closure of the energy budget, using CF calculated for the hydrological year (starting in October) and including measurements of G and ΔQ in the available energy estimation. Note that results from measurements taken for sub-catchment A only (not shown) are almost identical to those shown here.

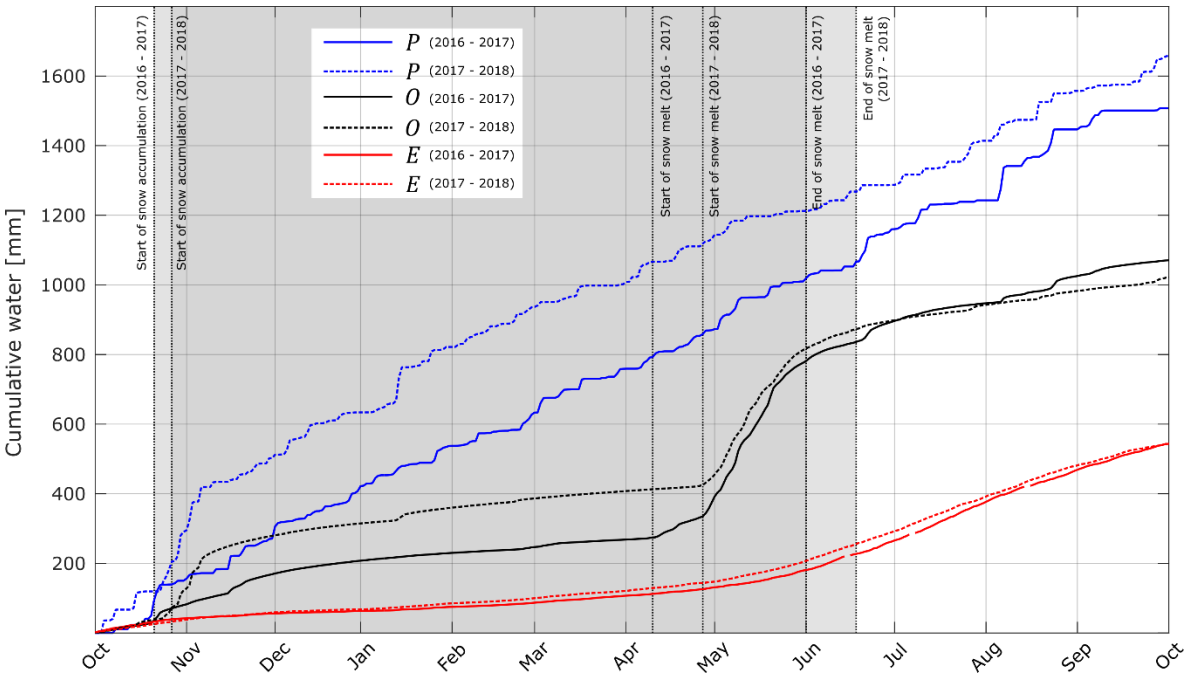

Figure 2.5: Cumulative precipitation *P* (blue), evapotranspiration *E* (red) and watershed outflow *O* (black) for hydrological years 2016-2017 (full lines) and 2017-2018 (dashed lines) for catchment AB. Hydrological years are defined from October 1 to September 30 to encompass winter snow-covered periods. The latter periods are illustrated using shades of grey on the graph.

As it is the case for most boreal watersheds, snow accumulation and melting are highly impactful on the Montmorency Forest water budget. During the two hydrological years of the study period, 44% and 33% of the annual precipitation fell in solid state, leading to a maximum seasonal snowpack depth of 213 cm and 180 cm for 2016-2017 and 2017-2018, respectively. Snowmelt generates a substantial proportion of annual watershed discharges: 503 mm and 456 mm, or 47% and 45% of total annual discharges in 2016-2017 and 2017-2018, respectively.

Throughout both years, *E* rates were maximized in summer, with 67% and 61% of annual *E* occurring from June to September inclusively in 2016-2017 and in 2017-2018, respectively. Instrument records show that 12% and 16% of annual *E* occurred as winter sublimation (when air temperature was below −2°C), in 2016-2017 and 2017-2018, respectively.

For both hydrological years, the water budget (Equation 2.2) did not fully close: subtracting annual *E* and *O* from annual *P* yielded residuals of −107 mm and 92 mm. These values correspond to 7% and 6% of annual precipitation for 2016-2017 and 2017-2018 respectively. Unfortunately, the ground water storage part of ΔS was not fully assessed. However, on a hydrological year time scale, storage variations in soil moisture and snowpack accumulation were not detected. Water table variations were not measured during the study period, but the small

residuals in the water budget suggest that ground water storage may not vary much from the start of 2016 to the end of 2018.

Results need to be put in perspective by stating the uncertainties associated with each measured water budget term. Precipitation measurements are known to be subject to wind-induced undercatch (Kochendorfer et al., 2017). However, the Montmorency Forest is also a site dedicated to study these issues (*e.g.*, Pierre et al., 2019), and the use of DFIR data during winter minimizes uncertainties. Note that when DFIR measurements were available, measured precipitation at the MELCC station accounted for 79% of DFIR measurements, and annual precipitation height increased from 1383 to 1508 mm y^{-1} and from 1482 to 1659 mm y^{-1} for 2016-2017 and 2017-2018, respectively. Undercatch is also a problem with liquid precipitation, and can amount to 4-6% (Sevruk et al., 2009).

Errors on *O* are minimal, since rating curves for the weirs have been constructed and verified frequently over 50 years, and include ice-cover periods. Overflow events seldom happen but are accounted for in the rating curves. It is hypothesized that some water flows underground out of the (head) AB watershed, and piezometers have recently been installed to verify underground water movement and storage. *E* errors are estimated using the random uncertainty method (Finkelstein & Sims, 2001), and they amount to 18% of annual *E* for each hydrological year (*e.g.*, the variability in Figure 2.4). Uncertainties also stem from the assumption of spatial representativeness of the flux towers *E* and the surface-weighted combination method. Watershed *E* is frequently the greatest source of uncertainties in watershed modeling (Donohue et al., 2010; Seiller & Anctil, 2014).

Despite these uncertainties, results paint a clear picture of the watershed. As was concluded in previous studies (*e.g.*, Barr et al., 2012; Brümmer et al., 2012), *E* rates are capped between 500 and 600 mm y^{-1} even in the presence of high precipitation height and maximum water availability. Excess precipitation then necessarily generates runoff and streamflow or recharge of ground water, which is quite beneficial to society. Water table recharge is plausible, considering that the immature canopy is unclosed, and hence water reaches and infiltrates the ground easily (Isabelle et al., 2018a). However, given the hilly topography of the site, subsurface flow to streams seems more probable. Nevertheless, it is clear that watershed discharge is the main water-evacuating process in place. This behaviour is typical for a mountainous headwater catchment.

2.8 Conclusion

The overarching goal of this study was to assess the effect of high precipitation height on the energy and water budgets of the boreal forest. First, we characterized the balsam fir – white birch stand of the Montmorency Forest in terms of energy and stand-scale water balance relative to 13 other boreal forest sites from around the world.

E and P were measured at all sites, while E_p was evaluated with net radiation and other meteorological measurements.

The Montmorency Forest vastly stands out as the site receiving the largest annual precipitation. All sites respond to increasing precipitation by generating more E fluxes, but dry environments tend to evaporate a larger proportion of annual precipitation because of higher evaporative demand. The Montmorency Forest thus provides supplemental information that complements the previously available (dryer) sites that were used in comparison. E appears to be capped at around 550 mm y^{-1}: this could be a physiological limit of boreal species and climate or because simultaneous increases in P and E_p are unlikely given that precipitation imply cloud cover (hence reduced net radiation), which decreases E_p. More studies partitioning E in its main components (transpiration, ground evaporation, and evaporation of intercepted precipitation) are needed to further our understanding of this observed ecohydrological limit.

Using precise measurements of watershed discharges at the Montmorency Forest sites, this study also outlined the watershed-scale (3.49 km^2) water budget of two hydrological years in a high-precipitation balsam fir boreal forest. Since E appears to be bounded by a maximum annual value (≈30% of P), excess water mostly becomes water discharge. This behaviour is typical of water budgets of headwater mountainous catchments. Water table measurements are still needed to thoroughly describe the watershed regime, but results are upcoming on this front.

To conclude, this study offers a precise experimental description of the catchment hydrological regime of a humid boreal forest typical of northeastern North America. Given the probable climate-change induced increase in precipitation, our results should be taken in consideration by hydroclimate modellers, especially those focused in the boreal zones of the world. In particular, they should expect that increases in precipitation will generate more watershed outflows than evapotranspiration rises.

2.9 Acknowledgments

The authors acknowledge all Montmorency Forest staff, especially Patrick Pineault and Charles Villeneuve, for their extremely valuable help in the field. We also would like to thank Annie-Claude Parent, Dany Crépault, Denis Jobin, Jean-Pierre Tatchegnon Gbegan, Benjamin Bouchard, Sophie Robitaille, Derek Jensen, Chaoxun Hang, Pascale Girard, Martin Pharand, Gabriel Hould Gosselin, Fabien Gaillard Blanca, Marie-Hélène Asselin, Audrey Combes, Bram Hadiwijaya and Achut Parajuli for their help installing the Juvenile and Sapling towers and instrumentation. This work was supported by the Natural Sciences and Engineering Research Council of Canada (NSERC), Ouranos Consortium, Hydro-Québec, Environment and Climate Change Canada, and Ministère de

l'Environnement et de la Lutte contre les Changements climatiques (MELCC), through NSERC project RDCPJ-477125-14, and by the the Fonds de recherche du Québéc - Nature et Technologies (FRQNT).

This work used eddy covariance data acquired and shared by the FLUXNET community, including these networks: AmeriFlux, AfriFlux, AsiaFlux, CarboAfrica, CarboEuropeIP, CarboItaly, CarboMont, ChinaFlux, Fluxnet-Canada, GreenGrass, ICOS, KoFlux, LBA, NECC, OzFlux-TERN, TCOS-Siberia, and USCCC. The ERA-Interim reanalysis data are provided by ECMWF and processed by LSCE. The FLUXNET eddy covariance data processing and harmonization was carried out by the European Fluxes Database Cluster, AmeriFlux Management Project, and Fluxdata project of FLUXNET, with the support of CDIAC and ICOS Ecosystem Thematic Center, and the OzFlux, ChinaFlux and AsiaFlux offices.

3 Application and evaluation of a two-wavelength scintillometry system to a complex shallow boreal-forested valley

3.1 Résumé

Les systèmes de scintillomètres à deux longueurs d'onde peuvent fournir des mesures indispensables des flux de chaleur sensible et latente à l'échelle régionale. Cependant, ces dispositifs ont rarement été déployés sur des terrains complexes recouverts de forêts et jamais dans la région boréale éloignée et inoccupée, où les flux à grande échelle sont essentiels pour les modélisateurs de l'hydrologie et du climat. Cette étude présente une comparaison des flux mesurés au-dessus d'une vallée en forêt boréale avec un système de scintillomètres à deux longueurs d'onde et un système de covariance des tourbillons. Les instruments ont été déployés à la fin de l'été 2017 et les données conservées pour l'analyse totalisent 19 jours complets. Le faisceau des scintillomètres mesurait 1347 m de long et se projetait dans la vallée à une hauteur entre 5 m et 100 m au-dessus du sol, avec une hauteur effective de ∼88 m. Les limites de la dérivation des flux de surface à l'aide de la scintillométrie en terrain complexe sont discutées et les effets des conditions atmosphériques sur la comparaison des flux entre les systèmes instrumentaux sont quantifiés. Les flux ont été calculés avec les scintillomètres uniquement et en utilisant certaines variables atmosphériques du système de covariance des tourbillons: les impacts de ces méthodes de calcul sur la corrélation entre les systèmes instrumentaux sont évalués. Malgré une faible concordance des paramètres de structure météorologiques entre les instruments, la comparaison des flux des scintillomètres et de la covariance des tourbillons donne une bonne corrélation (R^2 jusqu'à 0,87). La scintillométrie obtient la meilleure corrélation avec les données de covariance des tourbillons lorsque la hauteur de la couche de surface atmosphérique est supérieure à la hauteur effective du scintillomètre, mais R^2 ne diminue que très légèrement dans les autres cas (diminution moyenne de 0,11). La validité des flux des scintillomètres semble discutable pendant les périodes nocturnes et stables. Cette étude montre qu'il est possible de mesurer les flux à échelle régionale à l'aide de scintillomètres à deux longueurs d'onde dans des forêts non planes, mais d'autres études sont nécessaires pour déterminer le meilleur cadre méthodologique.

3.2 Abstract

Two-wavelength scintillometer systems can provide much needed measurements of area-averaged sensible and latent heat fluxes. However, these devices rarely have been deployed on canopy-covered complex terrain, and never in the circumpolar boreal biome, where large-scale fluxes are essential to hydroclimate modellers. This study presents a comparison of fluxes measured above a boreal-forested valley with a two-wavelength scintillometer and an eddy-covariance system. Instruments were deployed in late summer 2017, and 19 days of data were retained for the analysis. The scintillometer path was 1347-m long and projected across the valley

between 5 and 100 m above ground, with an effective height of ∼88 m. The limitations of deriving surface fluxes using scintillometry in complex terrain are discussed, and the effects of atmospheric conditions on flux comparison are quantified. Fluxes were calculated with the scintillometer only, and using certain atmospheric variables from the eddy-covariance system; impacts of these calculation methods on the correlation between instrumental systems are assessed. Despite a weak agreement of structure parameters between instruments, the comparison of scintillometer and eddy-covariance fluxes yields good correlation (R^2 up to 0.82). Scintillometry correlates best with eddy-covariance data when the atmospheric surface-layer height is above the scintillometer effective height, but R^2 only drops slightly otherwise (average decrease of 0.11). Validity of scintillometer fluxes appears dubious during night-time and stable periods. This study shows that area-averaged flux measurements using two-wavelength scintillometers are possible in non-flat forests, but more studies are needed to pinpoint the best methodological framework.

3.3 Introduction

The surface energy budget is crucial to meteorological and hydrological modeling since it determines the exchanges of heat and water between the surface and the atmosphere. Weather, climate, and hydrologic models are often set up on large-scale grids for numerical simplicity and speed. Their algorithms compute surface energy budgets at those scales, and large-scale flux measurements are required for development and validation. Remote-sensing products (e.g. Mapping Evapo-Transpiration at high spatial Resolution with Internalized Calibration, METRIC Allen et al. 2007b,a) can provide relevant information, but temporal resolutions are coarse, especially when considering frequent cloud cover. Ground-based measurement of turbulent fluxes are still necessary. The eddy-covariance (EC) measurement method has become the norm in that aspect, but it provides fluxes at a relatively small spatial scale (of the order of hectares). This warrants the installment of several flux towers to provide a basis that can be compared to large-scale grid points, but that is not always feasible.

This is especially true in northern latitudes, where the territory is vast and remote. The circumpolar boreal biome is of crucial importance to model weather in northern countries like Canada and climate in the northern hemisphere. Plus, the boreal regions encompass 30% of the world's forests (Brandt et al. 2013): it is the second largest vegetated area in extent (12–14 million km^2) behind tropical forests (Landsberg and Gower 1997). Furthermore, it sequesters 20% of the global forest carbon (Pan et al. 2011). The boreal forest is fairly heterogeneous, consisting of evergreen and deciduous forests, wetlands, and numerous lakes. Human exploitation of ligneous resources make it even patchier, with about two-thirds of its area being managed (Gauthier et al. 2015). Thus, ground-based large-scale measurements of turbulent fluxes in these heterogeneous landscapes are imperative, yet their deployments are rather complex.

Scintillometry is a relatively new measurement method that can provide an opportunity to take on the aforementioned challenges. With these devices, electromagnetic radiation of certain wavelengths travels between transmitters and receivers separated by a few kilometers, and fluctuations in the intensity of received light ("scintillations") can be linked to atmospheric turbulence. Source area for the fluxes causing these scintillations span several km^2, making the instruments ideal for obtaining spatial aggregates of turbulent fluxes over heterogeneous landscapes (Kleissl et al. 2009). Large-aperture scintillometers (LAS), using electromagnetic beams of infrared frequency, were the first to be introduced. They have been used to measure sensible heat fluxes (H), as temperature changes cause most of the scintillations in the infrared domain. Several studies have used such scintillometers to measure area-averaged turbulent fluxes, obtaining latent heat fluxes (LE) as the residual of the energy budget (*e.g.* Ezzahar et al. 2009a; Guyot et al. 2012) or by estimation of the Bowen ratio H/L_vE (*e.g.* Van Kesteren et al. 2013). Micro-wave scintillometer (MWS) have recently become commercially available and are particularly sensitive to humidity fluctuations. MWS are now used in combination with LAS to measure H and L_vE simultaneously, using the so-called "two-wavelength" and "bichromatic" methods, described thoroughly further in this paper.

Indeed, LAS, sometimes combined with MWS, have been successfully deployed over a variety of environments: mixed crop fields (*e.g.*, Meijninger et al., 2002a,b; Ezzahar and Chehbouni, 2009; Ezzahar et al., 2009b; Evans et al., 2012; Li et al., 2017), mixed forests, shrublands and agricultural fields in arid climates (*e.g.*, Kleissl et al., 2009; Zeweldi et al., 2010; Geli et al., 2012), pasture grasslands (*e.g.*, Yee et al., 2015) and semi or fully urban areas (*e.g.*, Samain et al., 2011; Ward et al., 2014; 2015a;b). Given the novelty of the instruments, these studies have mostly surveyed flat environments to validate the method in relatively simple conditions, usually by comparison with the EC method.

In her review of scintillometry deployed over complex terrain, Ward (2017) cites nine studies with scintillometers deployed over hilly forests (none of them in the boreal forest), six of which stem from the LITFASS experiment (Beyrich et al. 2002). Four more are located in complex topography (*e.g.* Rotach et al. 2017), and only two study sites featured the two-wavelength scintillometer system: the heterogeneous vegetated cover and moderate topography of the LITFASS experiment (Meijninger et al. 2006) and an urban site in Swindon, United Kingdom (Ward et al. 2015b,a). The latter study states that it is the first to present fluxes derived from the bichromatic method. In addition, few studies have deployed EC setups on sloping forested terrain (*e.g.* Geissbühler et al. 2000; Turnipseed et al. 2002; Aubinet et al. 2003; Goulden et al. 2012), and as far as we know, only one on slopes of the boreal forest (Isabelle et al. 2018). Known challenges regarding scintillometer deployments over complex terrain are many: applicability of Monin–Obukhov similarity theory, calculation of reliable footprints, acquisition of representative input for flux calculations, etc. (Ward 2017). Contrastingly, Rotach et al. (2014) estimates that easily over 50% of the land surfaces are comprised of complex topography. More studies are

needed on the surface energy budget over forested slopes, and more studies are definitely required using two-wavelength scintillometers; the present paper addresses both issues.

This study assesses the validity of a two-wavelength scintillometer for measuring turbulent fluxes in non-flat forested areas of the boreal region by comparison with the reference EC method. Both instrumental setups were installed in a shallow boreal-forested valley, making it the first study in such context, to the best of our knowledge. The specific interests of this paper are to compare: (i) structure parameters between measurement methods, as these are directly measured by the scintillometer, and (ii) turbulent fluxes obtained by both instrumental setups. Two methods are tested to obtain structure parameters from the scintillometer system: the two-wavelength (TW) and bichromatic (BC) methods. In addition, we explore two different methods to obtain turbulent fluxes from scintillometer structure parameters: an *independent method* using the stand-alone scintillometer, and a version combining input data from both scintillometer and the EC tower, called the *dependent method*. These methods feature some first-guess assumptions that may be violated at times given the complex nature of the study site; limitations of the scintillometer flux calculation methods are hence discussed carefully. The impacts of method choices and atmospheric conditions on comparison with EC are also assessed. The results are based on a two-month long field deployment of the two-wavelength scintillometer setup in the vicinity of an EC tower measuring fluxes continuously.

3.4 Scintillometer theory

3.4.1 Structure parameters: Two-wavelength method

Converting the scintillometer signal intensity to structure parameters can be done with the two-wavelength method (Hill et al., 1988; Andreas, 1989). As a first step, time variances of raw signal intensities are needed. In this paper, we use the notation where the variance of a signal intensity measured by a scintillometer *S* (LAS or MWS) is labeled as $\sigma_{S\,S}$. For the signal intensity, it is calculated as follows:

$$\sigma_{S\,S} = \overline{\left(\ln\left(\frac{I_S}{I_S^0}\right) - \overline{\ln\left(\frac{I_S}{I_S^0}\right)} \right)^2} \tag{3.1}$$

where overbars denote time averages over a certain variance integration period Ω [min]; I_S [mV] is the signal intensity of the scintillometer *S*; and I^0_S [mV], the scaling value of signal intensity for *S*, provided by a running average spanning a period ω [s]. Scaling the signal intensities with a running average acts as a high-pass filter that separates the scintillation signal from atmospheric absorption processes (Meijninger et al., 2006).

Then, the refractive index structure parameter $C_{n,S\,S}$ [$m^{-2/3}$] can be obtained as follows:

$$C_{n,SS} = \sigma_{SS} \Big/ \left[8.448\pi^2 k_S^2 \int_0^L W_S(x)\,dx \right] \tag{3.2}$$

where W_S [m$^{5/3}$] is the along-path weighing functions for scintillometer S; k_S [m^{-1}], the angular wavenumber ($2\pi / \lambda_S$); λ_S [m], the emitted wavelength of the signal from scintillometer S; x [m], the position along the scintillometer path; and L [m], the distance between transmitters and receivers. Note that to simplify notation, we apply $C_{n,S\,S} = C_{n,S}^2$ (*e.g.* $C_{n,LAS\,LAS} = C_{n,LAS}^2$). The W_S function depends on the geometrical aspects of the experimental setup: the aperture of the LAS or MWS antennas, the distance L, and the emitted wavelength λ_{LAS} [m] or λ_{MWS} [m]. The W_S-functions are thoroughly described in Lüdi et al. (2005).

$C_{n,S}^2$ at each wavelength is related to the structure parameters of temperature C_T^2 [K^2 m$^{-2/3}$] and humidity C_q^2 [kg^2 kg^{-2} m$^{-2/3}$], and to the cross-structure parameter of temperature-humidity C_{Tq} [K kg kg^{-1} m$^{-2/3}$], with the following equations:

$$C_{n,LAS^2} = \frac{A_{T,LAS}^2}{T^2} C_{T^2} + 2\frac{A_{T,LAS}A_{q,LAS}}{Tq} C_{Tq} + \frac{A_{q,LAS}^2}{q^2} C_{q^2} \tag{3.3}$$

$$C_{n,MWS^2} = \frac{A_{T,MWS}^2}{T^2} C_{T^2} + 2\frac{A_{T,MWS}A_{q,MWS}}{Tq} C_{Tq} + \frac{A_{q,MWS}^2}{q^2} C_{q^2} \tag{3.4}$$

where T is the air temperature [K]; q is the air specific humidity [kg kg^{-1}]; and $A_{T,LAS}$, $A_{T,MWS}$, $A_{q,LAS}$ and $A_{q,MWS}$, the wavelength-dependent structure parameter coefficients (dimensionless) for temperature T and specific humidity q for the LAS and MWS respectively.

With the TW method, C_{Tq} is not measured, and it is approximated using the temperature-humidity correlation coefficient R_{Tq}:

$$R_{Tq} = \frac{C_{Tq}}{\sqrt{C_{T^2} C_{q^2}}} \tag{3.5}$$

The latter varies between ±1 depending on stability conditions. When its value is assumed, C_T^2 and C_q^2 can be isolated from Equations 3.3 and 3.4:

$$C_{T^2} = \frac{A_{q,MWS}^2 C_{n,LAS^2} + A_{q,LAS}^2 C_{n,MWS^2} + 2R_{Tq}A_{q,LAS}A_{q,MWS}\sqrt{C_{n,LAS^2}C_{n,MWS^2}}}{\left(A_{T,MWS}A_{q,LAS} - A_{T,LAS}A_{q,MWS}\right)^2 T^{-2}} \tag{3.6}$$

$$C_{q^2} = \frac{A_{T,MWS}^2 C_{n,LAS^2} + A_{T,LAS}^2 C_{n,MWS^2} + 2R_{Tq}A_{T,LAS}A_{T,MWS}\sqrt{C_{n,LAS^2}C_{n,MWS^2}}}{\left(A_{T,MWS}A_{q,LAS} - A_{T,LAS}A_{q,MWS}\right)^2 q^{-2}} \tag{3.7}$$

Note that with the two-wavelength method, the sign and magnitude of R_{Tq} must be assumed a priori (see Section 3.6.1.2).

3.4.2 Structure parameters: Bichromatic method

Structure parameters can also be obtained via the bichromatic method (henceforth labeled BC, Lüdi et al., 2005). The basic assumption underlying this method is that both scintillometers are sampling the same air volume. This needs to be implemented in the setup of the scintillometers: (i) both transmitters and both receivers need to be mounted very close to one another, and (ii) LAS and MWS beams have to cross paths. Then, the covariance of both signals, labeled $\sigma_{LAS\,MWS}$ is calculated as follows:

$$\sigma_{LAS\,MWS} = \overline{\left(\ln\left(\frac{I_{LAS}}{I^0_{LAS}}\right) - \overline{\ln\left(\frac{I_{LAS}}{I^0_{LAS}}\right)} \right) \times \left(\ln\left(\frac{I_{MWS}}{I^0_{MWS}}\right) - \overline{\ln\left(\frac{I_{MWS}}{I^0_{MWS}}\right)} \right)} \tag{3.8}$$

Using this covariance, a third value of C_n can be obtained. We label it using the subscript OMS for Optical Microwave Scintillometer:

$$C_{n,OMS} = \sigma_{LAS\,MWS} \Big/ \left[8.448\pi^2 k_{LAS} k_{MWS} \int_0^L W_{OMS}(x)\,dx \right] \tag{3.9}$$

where W_{OMS} is also an along-path weighing function, described in Lüdi et al. (2005). The main differences between W_{OMS} and W_{LAS} or W_{MWS} is that it includes geometrical aspects of both the LAS and MWS, and it also depends on the separation d [m] between the LAS and MWS signal path.

Having a third value of the structure parameter of refractive index adds a third equation relating C_n^2 with C_T^2, C_q^2 and C_{Tq}:

$$C_{n,OMS} = \frac{A_{T,LAS} A_{T,MWS}}{T^2} C_{T^2} + 2\frac{A_{T,LAS} A_{q,MWS} + A_{T,MWS} A_{q,LAS}}{Tq} C_{Tq} + \frac{A_{q,LAS} A_{q,MWS}}{q^2} C_{q^2} \tag{3.10}$$

The combination of Equations 3.4, 3.5 and 3.10 can be solved via standard matrix resolution. This allows direct calculation of C_{Tq} and hence of R_{Tq}.

3.4.3 Flux calculations

The structure parameters of temperature C_T^2 and humidity C_q^2 can be related to sensible and latent heat fluxes via the Monin-Obukhov similarity theory (Monin and Yaglom, 1971; Wyngaard et al., 1971):

$$\frac{C_{T^2}\left(z_{m,eff} - d_0\right)^{2/3}}{T_*^2} = f_T(\zeta) \tag{3.11}$$

$$\frac{C_{q^2}\left(z_{m,eff}-d_0\right)^{2/3}}{q_*^2}=f_q\left(\zeta\right) \tag{3.12}$$

where $z_{m,eff}$ is the effective scintillometer measurement height [m]; d_0, the zero-plane displacement height [m]; T_* [K] and q_* [kg kg^{-1}], the scaling variables of temperature and humidity, respectively; f_T and f_q, similarity functions describing how changes in structure parameters with height are affected by atmospheric stability (expressed as the stability parameter $\zeta = (z_{m,eff} - d_0) / L_{Ob}$); and L_{Ob} [m], the Obukhov length, which is calculated as follows (Stull, 1988):

$$L_{Ob}=\frac{-u_*^3 T}{\kappa g\left(\frac{H}{\rho c_p}+0.61T\frac{L_vE}{\rho L_v}\right)} \tag{3.13}$$

where κ [-] is the Von Karmán constant (= 0.41); ρ [kg m^{-3}], the humid air density; H [W m^{-2}], the sensible heat flux; L_vE [W m^{-2}], the latent heat flux; g [m s^{-2}], the gravitational constant; c_p [J kg^{-1} K^{-1}], the specific heat of moist air; L_v [J kg^{-1}], the latent heat of vaporization of water; and u_* [m s^{-1}], the friction velocity, calculated as:

$$u_*=\frac{\kappa U}{\ln\left(\frac{z_{m,eff}-d_0}{z_0}\right)-\Psi_m\left(\zeta\right)+\Psi_m\left(\frac{z_0}{L_{Ob}}\right)} \tag{3.14}$$

where U [m s^{-1}] is the wind speed; z_0 [m], the roughness length; and Ψ_m, the stability correction functions for momentum (see Brutsaert (1982) for a complete description).

For unstable conditions ($\zeta < 0$), the stability function f_T and f_q are described as:

$$f_T\left(\zeta\right)=x_{T,1}\left(1-x_{T,2}\zeta\right)^{-2/3} \tag{3.15}$$

$$f_q\left(\zeta\right)=x_{q,1}\left(1-x_{q,2}\zeta\right)^{-2/3} \tag{3.16}$$

and for stable conditions ($\zeta > 0$), as:

$$f_T\left(\zeta\right)=x_{T,3}\left(1+x_{T,4}\zeta^{2/3}\right) \tag{3.17}$$

$$f_q\left(\zeta\right)=x_{q,3}\left(1+x_{q,4}\zeta^{2/3}\right) \tag{3.18}$$

where $x_{T,1}$, $x_{T,2}$, $x_{T,3}$, $x_{T,4}$, and $x_{q,1}$, $x_{q,2}$, $x_{q,3}$, and $x_{q,4}$ are fitting parameters taken from the literature (see Section 3.6.1.2).

The sensible and latent heat fluxes are then related to the temperature and humidity scales as follows:

$$H = T_* \rho c_p u_* \tag{3.19}$$

$$L_v E = q_* \rho L_v u_* \tag{3.20}$$

As the turbulent fluxes (H, L_vE), the scaling variables (u_*, T_*, q_*) and the Obukhov length are unknown, Equations 3.11 to 3.20 can be solved in one of two ways: iteratively (independent method) or by feeding stability and friction velocity from the EC tower (dependent method).

For the independent method, L_{Ob} is initially set at an arbitrary value used to calculate the stability functions f_T and f_q following Equations 3.15 to 3.18 and friction velocity u_* using Equation 3.14. We then obtain T_* and q_* using Equations 3.11 and 3.12 with the measured scintillometer measurements C_T^2 and C_q^2. Fluxes are calculated with Equations 3.19 and 3.20 and are used to calculate a new value of L_{Ob} to begin a new iteration. The process stops when the fluxes absolute differences between two iterations are under a certain threshold: in this study, we used 1 W m^{-2}.

With the dependent method, L_{Ob} is obtained from the EC tower data and used to compute f_T and f_q then T_* and q_* with Equations 3.11 and 3.12. Friction velocity u_* is also the value measured at the EC tower and fluxes are obtained from Equations 3.19 and 3.20.

Fluxes calculated using either the TW or BC structure parameters and obtained from either the independent or dependent calculation method are characterized by a sign ambiguity: the methods calculate the magnitude of the fluxes, but the signs are unknown. The theory however stipulates that the fluxes have the same sign when $R_{Tq} > 0$, and opposite sign otherwise. Positive R_{Tq} during the day usually implies that both H and L_vE are positive. At night, instances of negative R_{Tq} are often taken as implying negative H and positive L_vE, as dewfall indicated by the other combination are rarer. This assumption however leads to overestimation of L_vE. Section 3.6.1.2 details the procedure used to obtain flux signs in this study.

Technically, Monin-Obukhov similarity theory is applicable in the atmospheric surface layer (ASL), also labeled constant flux layer, and under horizontal homogeneity, stationary flow and negligible effect from processes above the ASL (Moene and Schüttemeyer, 2008). Evidently, these criteria can be transgressed at times, especially over complex terrain, where processes like horizontal advection, drainage flows and internal boundary layers further complicate matters. However, scintillometer systems can still be deployed in complex topography provided that special care is included in the data processing (Ward, 2017).

3.5 Study Site

The study was conducted in a 1.2-km^2 experimental watershed at the northern end of the “Bassin Expérimental du Ruisseau des Eaux-Volées” (Lavigne, 2007; Tremblay et al., 2008, 2009; Noël et al., 2014; Isabelle et al.,

2018), which lies in the Montmorency Forest¨ (47°17'18"N; 71°10'05.4"W), some 80 km north of Quebec City, Canada. The field site is part of the Laurentian Mountains and the watershed has a mean altitude of 860 m above mean sea level (AMSL) and hilltops at 1000 m AMSL. The watershed features a vegetation composed predominantly of balsam firs (*Abies balsamea* (L.) Mill), with sparse white spruces (*Picea glauca* (Moench) Voss) and white birches (*Betula papyrifera* Marsh). 85% of the watershed trees were logged in 1993 and natural regeneration occurred, the trees now stand 4-8 m tall. The Montmorency Forest is under the influence of a continental climate characterized by a short and cool growing season, while precipitation is frequent during the whole year. Environment and Climate Change Canada reports an average annual temperature of 0.5°C and an average annual precipitation of 1583 mm (40% as snow) during the period 1981-2010 (Station "Foret Montmorency", available at: http://climat.meteo.gc.ca/historical data/search_historic_data_f.html).

3.6 Materials and methods

3.6.1 Scintillometer Measurements

3.6.1.1 Instrumental setup

This study features a two-wavelength scintillometer system, meaning that two transmitters and two receivers were mounted at each end of the beam path outlined in Figure 3.1. The LAS was a BLS-900 (Scintec, Germany), sending a beam of wavelength λ_{LAS} = 0.880 µm through a 0.145 m aperture. The MWS was the RPG-MWSC-160 (RPG, Germany), with λ_{MWS} = 1860 µm and an aperture of 0.3 m.

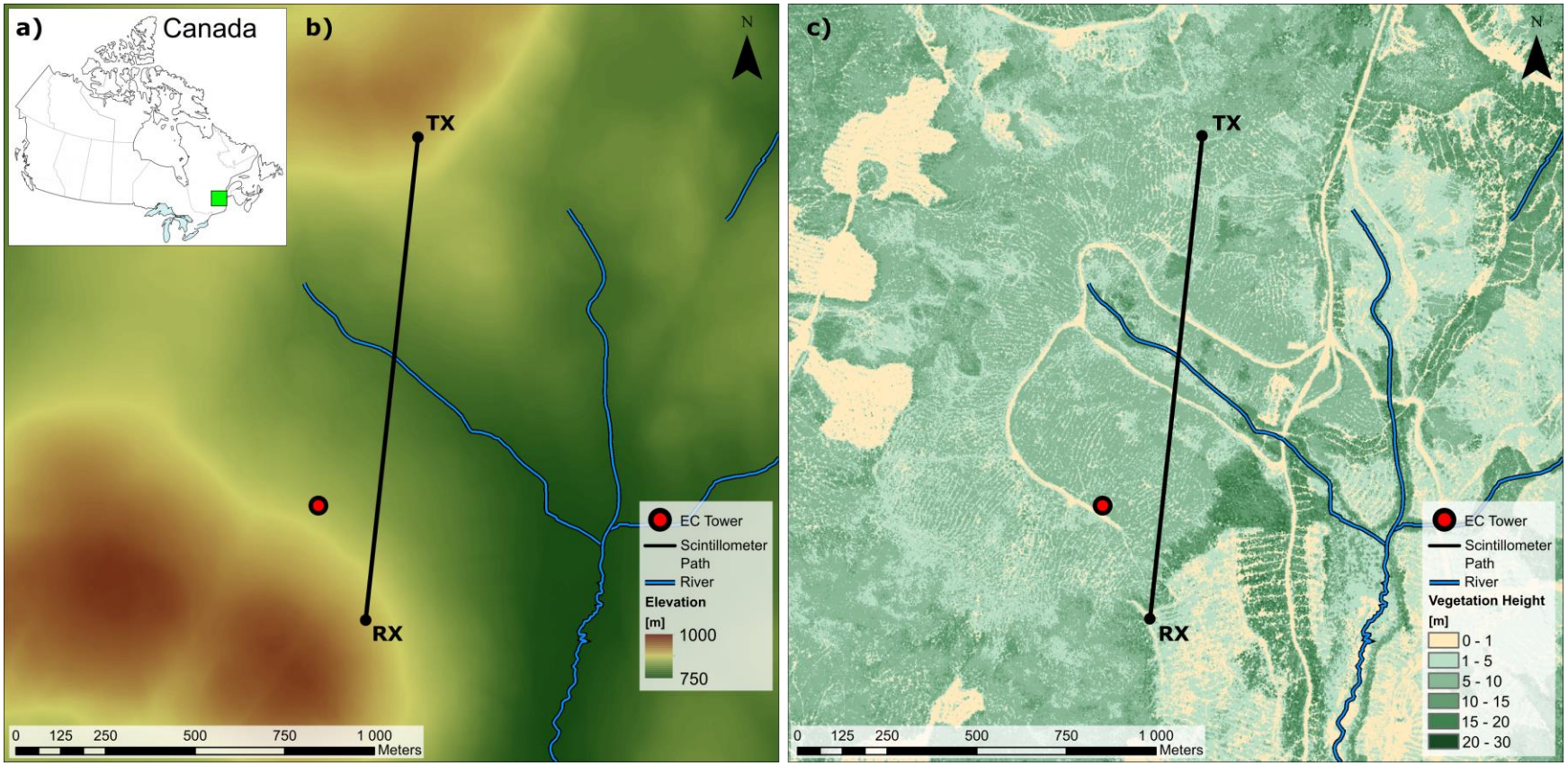

Figure 3.1: (a) Location of the Montmorency Forest (green square) in Canada. (b) Location of the EC tower and scintillometer transmitter (TX) and receiver (RX) towers, with topography; and (c) vegetation height in the background, as of 2016. Topography and vegetation height are computed from LIDAR surveys (Source: Ministère Forêts, Faune et Parcs du Québec).

Figure 3.2 shows an elevation view of the scintillometer paths and the underlying topography and vegetation. At the transmitter end, the MWS and LAS were mounted at heights of 5.19 m and 5.73 m, while they were at heights of 6.00 m and 5.17 m at the receiver end, respectively. This setup ensures that the LAS and MWS beams cross around the center of the scintillometer path. The path height z_m varies between ~5 and ~100 m, while the separation between LAS and MWS beams varies between 0 m and 0.83 m.

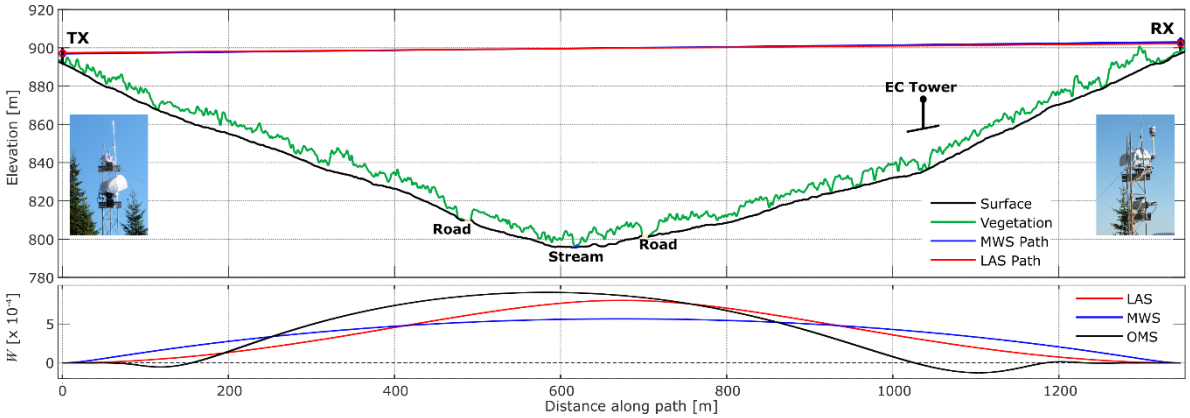

Figure 3.2: Elevation view of the scintillometer path from the transmitting (TX) tower to the receiving (RX) tower (left and right photographs, respectively, looking east). Surface and vegetation height from LIDAR surveys under the path are shown (Source: Ministère Forêts, Faune et Parcs du Québec). The EC tower is also shown: as the viewpoint of this figure is from northwest, the EC tower is ~165 m from the path towards the reader. Bottom panel shows the normalized weighing function W along the path.

Figure 3.2 also presents the shape of the weighting functions W_S (Equation 3.2), normalized over the whole path, that characterizes the scintillation contribution to the measured signal at position x along the path, for the LAS and MWS and the two-wavelength system (OMS). W_{LAS} and W_{MWS} are symmetric, but the W_{OMS} maximum contribution is slightly skewed towards the transmitter tower. This is caused by different spacing between the LAS and MWS at both towers (0.83 m at receiver, 0.54 m at transmitter). Using these functions and the method outlined by Hartogensis et al. (2003), we calculated an effective measurement height $z_{m,eff}$ of ≈88 m above the ground. Only few studies have taken scintillometer measurements at such heights, including Min et al. (2004); Samain et al. (2011); Braam et al. (2012); Jacobs et al. (2015); Crawford et al. (2017) and Rotach et al. (2017).

3.6.1.2 Data processing

The received signals of both LAS and MWS were sampled at a 1000 Hz. Raw signals were put through minimal filtering prior to variance calculations: obvious spikes, drop-outs and periods of power loss were removed. LAS and MWS spectra were visually inspected to detect any vibrational contamination from oscillating tower structures: none were found, by checking against expected spectra (Ward et al., 2015b). Running averaging

periods ω were set to values of 9 and 58 s for the LAS and MWS, respectively, following manufacturers recommendations (RPG, 2014). Variance integration period Ω was set to 10 min accordingly.

Values of C_n were subjected to very strict filtering. Saturation check was performed following standard methodology (Kleissl et al., 2010), but saturation never occurred during our study period, neither for the LAS nor the MWS. Instances of low power at transmitter end were detected when $C_{n,LAS}^2$ flatlined and the whole day was removed from the dataset. Rain and fog generated unrealistic spikes in $C_{n,MWS}^2$ and $C_{n,OMS}$ and these periods were discarded as well. $C_{n,LAS}^2$ and $C_{n,MWS}^2$ were scaled to the effective height of $C_{n,OMS}$ to account for the different effective heights of the three structure parameters (LAS: ≈83 m; MWS: ≈76 m; OMS: ≈88 m), caused by different weighing functions (see Figure 3.2). This was done following the stability-dependent method of Evans and DeBruin (2011).

The scintillometer system was installed at the site between 11 August 2017 and 28 September 2017 inclusively. Out of these 49 days, 30 had to be filtered out completely due to battery power issues that influenced the transmitted and/or received signal or to intense fog and/or rain events, leaving 19 days of optimal data (see Table 3.1).

Table 3.1: Meteorological conditions of each study day. PASL = percentage of time with $z_{ASL} > z_{m,eff}$; FVD = footprint vegetation height dissimilarity between EC and scintillometer; FRD = footprint daily-summed net radiation dissimilarity between EC and scintillometer; PRAD = percentage of maximum theoretical radiation; PUNS = percentage of unstable conditions ($\zeta < -0.05$); PNEU = percentage of near-neutral conditions ($|\zeta| < 0.05$); PSTA = percentage of stable conditions ($\zeta > 0.05$).

Date	Daily Rainfall [mm]	PASL [%]	FVD [-]	FRD [-]	PRAD [%]	PUNS [%]	PNEU [%]	PSTA [%]
11 Aug 2017	0.02	21	0.029	0.032	71	46	2	52
24 Aug 2017	0.53	88	0.013	0.007	32	13	69	19
25 Aug 2017	0.47	46	0.019	0.036	42	0	73	27
26 Aug 2017	0.06	38	0.015	0.031	79	29	17	54
27 Aug 2017	0.06	40	0.026	0.022	84	42	2	56
28 Aug 2017	0.02	40	0.015	0.031	96	50	2	48
29 Aug 2017	0.06	40	0.013	0.026	93	48	0	52
30 Aug 2017	0.00	38	0.016	0.035	79	40	4	56
12 Sept 2017	0.00	29	0.021	0.025	87	23	23	54
13 Sept 2017	0.02	31	0.019	0.022	99	31	10	58
14 Sept 2017	0.02	29	0.026	0.036	95	29	10	60
15 Sept 2017	0.00	19	0.019	0.037	85	48	6	46
16 Sept 2017	0.00	2	0.018	0.015	61	29	19	52
21 Sept 2017	0.00	25	0.030	0.032	100	44	4	52
22 Sept 2017	0.00	0	0.016	0.032	100	38	4	58
23 Sept 2017	0.08	23	0.030	0.038	77	25	17	58
24 Sept 2017	0.02	4	0.022	0.043	64	17	27	56
25 Sept 2017	0.28	25	0.028	0.026	98	31	8	60
28 Sept 2017	1.07	92	0.013	0.039	57	0	81	19

*: Footprints calculated in all stability situations since PUNS = 0.

For these 19 days, C_T^2, C_q^2 and C_{Tq} were calculated using both TW and BC methods. Coefficients $A_{T,LAS}$, $A_{T,MWS}$, $A_{q,LAS}$ and $A_{q,MWS}$ were computed following Ward et al. (2013) (see the formulas in their Table 2). Air temperature T and specific humidity q were measured at the EC tower to reflect meteorological conditions as close as possible to the center of the scintillometer path.

With the TW method, R_{Tq} has to be assumed: we used values of ±0.8. The chosen value of R_{Tq}, positive for unstable conditions and negative for stable conditions, was also used by Evans (2009), recommended by Ward (2017) and is consistent with observed EC tower data (see section 3.7.1). Stability transitions, and hence switching points between positive and negative R_{Tq}, were determined to occur at twice-daily instances of $C_{n,LAS}^2$ minima, in the morning and late-afternoon, following Samain et al. (2012). Figure 3.3 presents a typical daily cycle of the three values of C_n, illustrating the stability transitions.

During flux calculations, the values of U, c_p, ρ and L_v were measured (or derived from measured T and q) at the EC tower. d_0 and z_0 were set to (2 / 3) h_v and $z_0 = h_v / 10$, respectively, where h_v is the mean vegetation height (Brutsaert, 1982). From LIDAR images (see Figure 3.1b) and ground surveys, h_v = 6 m was applied. These parameters make the final measurement height of the scintillometer ($z_{m,eff} - d_0$) $\approx$ 84 m.

This considerable measurement height warrants carefulness in the analysis of scintillometer fluxes. Indeed, in such conditions, the measurement beam might lie outside the ASL, where Monin-Obukhov similarity theory is technically inapplicable and scintillometer flux measurements are less reliable (Braam et al., 2012). Section 3.6.5 describes the method used to evaluate ASL height z_{ASL} and describes how it is included in our comparison analysis.

Special care also has to be taken when choosing the similarity functions f_T and f_q (Ward et al., 2015a; Ward, 2017). Even over a "perfect" homogeneous surface, these functions are known to average a large scatter of observations, and are hence large sources of uncertainties. Fit parameters for stability functions $x_{T,1}$, $x_{T,2}$, $x_{T,3}$, $x_{T,4}$, and $x_{q,1}$, $x_{q,2}$, $x_{q,3}$, $x_{q,4}$ were given values recommended by Kooijmans and Hartogensis (2016), which is the most diligent procedure according to Ward (2017).

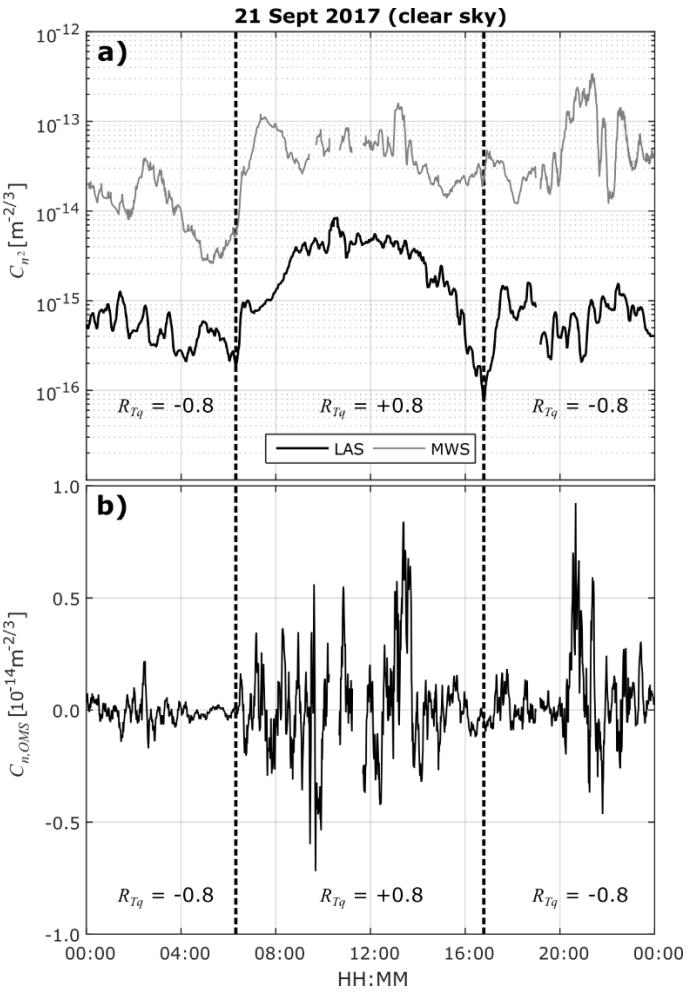

Figure 3.3: Daily cycle of (a) $C_{n,S}^2$ from LAS and MWS and of (b) $C_{n,OMS}$ on 21 September 2017. The vertical dashed lines mark the time where R_{Tq} is switched from −0.8 to +0.8 and conversely, coinciding with morning and evening minima of $C_{n,LAS}^2$, at 06:18 and 16:48 local standard time (LST = UTC – 5), respectively. Note that local sunrise and sunset occur at 05:31 and 17:44 LST, respectively.

For this study, we calculated fluxes with structure parameters obtained with TW and BC methods, and using both independent (subscript *i*) and dependent (subscript *d*) variations. For TW_i and BC_i, signs of fluxes were attributed using the sign of R_{Tq}: if positive, both fluxes were positive, whereas when $R_{Tq} < 0$, H was negative and L_vE was positive. With TW_d and BC_d, fluxes were given the same sign as that from the EC tower measurements.

3.6.2 Eddy-covariance measurements

3.6.2.1 Instrumental setup

Since October 2015, a flux tower has been continuously monitoring sensible and latent heat fluxes at the study site using the EC technique. The latter is executed using two sets of sonic anemometers and CO_2/H_2O gas analyzers (IRGASONs, Campbell Scientific, USA). The setup was installed at a height of 14.63 m on a 15-m

scaffolding, ~8 m above the top of the canopy. The two devices face opposite directions (303°, northwest; and 118°, southeast): by combining both time series, we avoid wind interference by the scaffolding and devices; hence ensuring optimal fluxes quality. Both devices were mounted parallel to the local slope (inclination: 12°; aspect: 30°). This alignment can increase the contributions of horizontal flows to slope-normal fluxes (Oldroyd et al., 2016), but is still deemed necessary to reduce flow distortion (Geissbühler et al., 2000; Oldroyd et al., 2016) and, hence, for the EC method to be applicable on sloped terrain (Turnipseed et al., 2002; Hammerle et al., 2007; Hiller et al., 2008; Goulden et al., 2012; Nadeau et al., 2013; Stiperski and Rotach, 2016). Measurements were taken using a 10-Hz sampling frequency and logged separately on two CR3000 dataloggers (Campbell Scientific, USA).

3.6.2.2 Data processing

The processing of raw 10-Hz measurements was done using EddyPro ®, version 6.0 (LICOR Biosciences, USA). The procedure included linear detrending, covariance maximization, correction of low-pass (Moncrieff et al., 1997) and high-pass (Moncrieff et al., 2004) filtering effects, density fluctuations compensation with the Webb correction (Webb et al., 1980) and coordinate rotation of wind speed. The latter was performed using a sector-wise planar fit (Wilczak et al., 2001), as this method is recommended for EC setups on slopes (Ono et al., 2008; Oldroyd et al., 2016). The statistical tests of Vickers and Mahrt (1997) allowed for the detection and removal of spikes, amplitude resolution artifacts, unrealistic drop-outs, outliers and discontinuities, as well as other artifacts in the measurements. The averaging period used to compute turbulent fluxes was 30 min. Flux errors were assessed following the random uncertainty method of Finkelstein and Sims (2001).

Data runs with poor quality according to the 0-1-2 criteria described in Mauder and Foken (2011) were filtered out. The same treatment was applied to data segments during rainfall events that can obstruct the path of the open gas analyzer light signal, and for periods where winds were blowing from a 120° sector centered on the back of the devices, as these conditions imply that the flow of air is distorted by the tower structure. A meticulous visual inspection of the 30-min averaged time series of all measured and computed variables allowed for the detection of periods of clear malfunction, they were also removed. This filtering procedure was rigorous, but once the data from both EC setups were combined by wind direction, 17% and 21% of the sensible and latent heat flux data, respectively, ended up missing for the whole study period (11 August 2017 to 28 September 2017 inclusively). Considering only the 19 days of optimal scintillometer data (see Table 3.1), these percentages drop to 9% and 6% of the sensible and latent heat flux data, respectively.

3.6.2.3 Structure parameter calculation

The EC system does not directly provide temperature and humidity structure parameters. However, using Taylor frozen turbulence hypothesis, a time lag ε in the EC raw 10-Hz measurements of temperature, humidity and

wind speed can be converted to a spatial lag δ with wind speed. Namely, we used the method outlined in Ward et al. (2015b) to convert the temporal structure function $D_{yy\,t}$, given as:

$$D_{yy\_t}(\varepsilon) = \overline{\left[y(t+\varepsilon) - y(t)\right]^2} \tag{3.21}$$

to the spatial structure function $D_{yy\,x}$ using (Bosveld et al., 1999):

$$D_{yy\_x}(\delta) = \frac{D_{yy\_t}(\delta / U)}{\left(1 - \frac{\sigma_u^2}{9U^2} + \frac{\sigma_v^2}{3U^2} + \frac{\sigma_w^2}{3U^2}\right)} \tag{3.22}$$

where overbars indicate a temporal average over one minute; $y(t)$, the value of temperature or humidity at time t; U, the mean wind speed; and σ_u^2, σ_v^2 and σ_w^2, the variances of the three-dimensional wind components u, v, and w, respectively. Structure parameters are then calculated as follows:

$$C_{y^2} = D_{yy\_x}(\delta)\delta^{-2/3} \tag{3.23}$$

Note that C_{Tq} is calculated by modifying Equation 3.21 to:

$$D_{yy\_t}(\varepsilon) = \overline{\left[T(t+\varepsilon) - T(t)\right]\left[q(t+\varepsilon) - q(t)\right]} \tag{3.24}$$

In this study, we aimed at finding the $D_{yy\,x}$ for definite values of δ: ε was adjusted using minute-averaged wind speed values. We duplicated calculations for several δ values (1, 2, 3, 4 and 5 m), which allows us to assess the magnitude of uncertainties on the structure parameters. Periods when the 5 values of meteorological structure parameters diverged by a coefficient of variation (standard deviation divided by average) over 0.4 were discarded, as they indicated non-inertial behavior. Final values of C_T^2 and C_q^2 were taken as the average of their values at the 5 δ length. To make sure the identity described in Equation 3.5 was conserved, the arithmetic mean of the 5 values of R_{Tq} was used to obtain the final EC values of C_{Tq}. Using this method, relative uncertainties averaged at 20%, 13% and 6% for C_T^2, C_q^2 and C_{Tq}, respectively.

Structure parameters vary significantly with height as shown in Equations 3.11 and 3.12. Thus, comparison between EC and scintillometer structure parameters necessitates the application of a scaling procedure on the former to convert from the 14.63-m EC tower height to the scintillometer $z_{m,eff}$ = 88 m. This is done using the aforementioned Equations 3.11 and 3.12 assuming uniform T_* and q_* and taking the same fit parameters in the stability functions f_T and f_q. Note that as this scaling procedure is based on Monin-Obukhov similarity theory functions, it is affected by uncertainties related to the validity of Monin-Obukhov similarity theory (see sections 3.6.1.2 and 3.8).

3.6.3 Footprint calculation

In this study, footprint estimates were calculated using the Flux Footprint Prediction (FFP) parameterization of Kljun et al. (2015). The method capitalizes on a very efficient footprint parameterization validated by a great number of Lagrangian stochastic particle dispersion simulations. Notably, the FFP method has been used widely over a large range of applicability regarding atmospheric conditions ($z_m / L_{Ob} > -15.5$) and measurement heights ($20\ z_0 < z_m < 0.8 z_{BL}$), but only above ideal flat grounds.

To calculate flux footprints, the method needs seven input variables: (i) the measurement height z_m; (ii) the roughness length z_0, which can also be estimated with mean wind speed U and the diabatic surface-layer wind speed profile (Stull, 1988); (iii) the boundary-layer height z_{BL}; (iv) the standard deviation of crosswind velocity fluctuations σ_v; (v) the friction velocity u_*; (vi) the Obukhov length L_{Ob}; and (vii) the wind direction WD to rotate the footprint around the tower.

For the EC tower footprint calculations, U, σ_v, u_*, L_{Ob} and WD are measured directly. z_m is fixed at 10.36 m, which is the 14.36 m setup height minus the zero-displacement height d_0, set to $(2 / 3)\ h_v$ where $h_v \approx 6$ m around the EC tower. z_0 is estimated as $0.1 h_v = 0.6$ m, while z_{BL} is obtained via the ERA-Interim reanalysis (Dee et al. 2011).

To estimate the scintillometer footprint, the parameterisation scheme of Kljun et al. (2015) was also used, this time on a discretized number of points following the measurement path (271 points 5 m apart). Each point calculation generated a footprint surface, and the total footprint of the scintillometer system was taken as the sum of all surfaces weighted by the OMS weighing function value at the point location. We tested a 2-m resolution of footprint calculation point along the scintillometer path, but it did not significantly modify the footprint. The 5-m resolution was hence chosen as the calculations were already quite computationally expensive.

For the scintillometer footprint calculations, σ_v, u_*, WD and z_{BL} were the same values used for the EC tower calculations. The latter comes from ERA-Interim, which has a resolution that encloses both the EC tower and the scintillometer system (0.75°). The wind-related values are the best we can use in our experimental context since the tower is relatively close to the path center. Note however that in its procedure, FFP approximates wind speed at beam height using z_0 and the diabatic log-wind profile, which is only applicable in the surface-layer. For this reason, we compute footprints only during unstable periods. z_m and z_0 were derived from h_v which was derived from the same LIDAR data used to generate Figure 3.1 and Figure 3.2, using the same approximations as with the EC tower with the values of elevation and vegetation height directly under the path.

Figure 3.4 presents the averaged footprint of both instrumental setups over the whole study period, considering only times when the atmosphere is unstable (see Table 3.1).

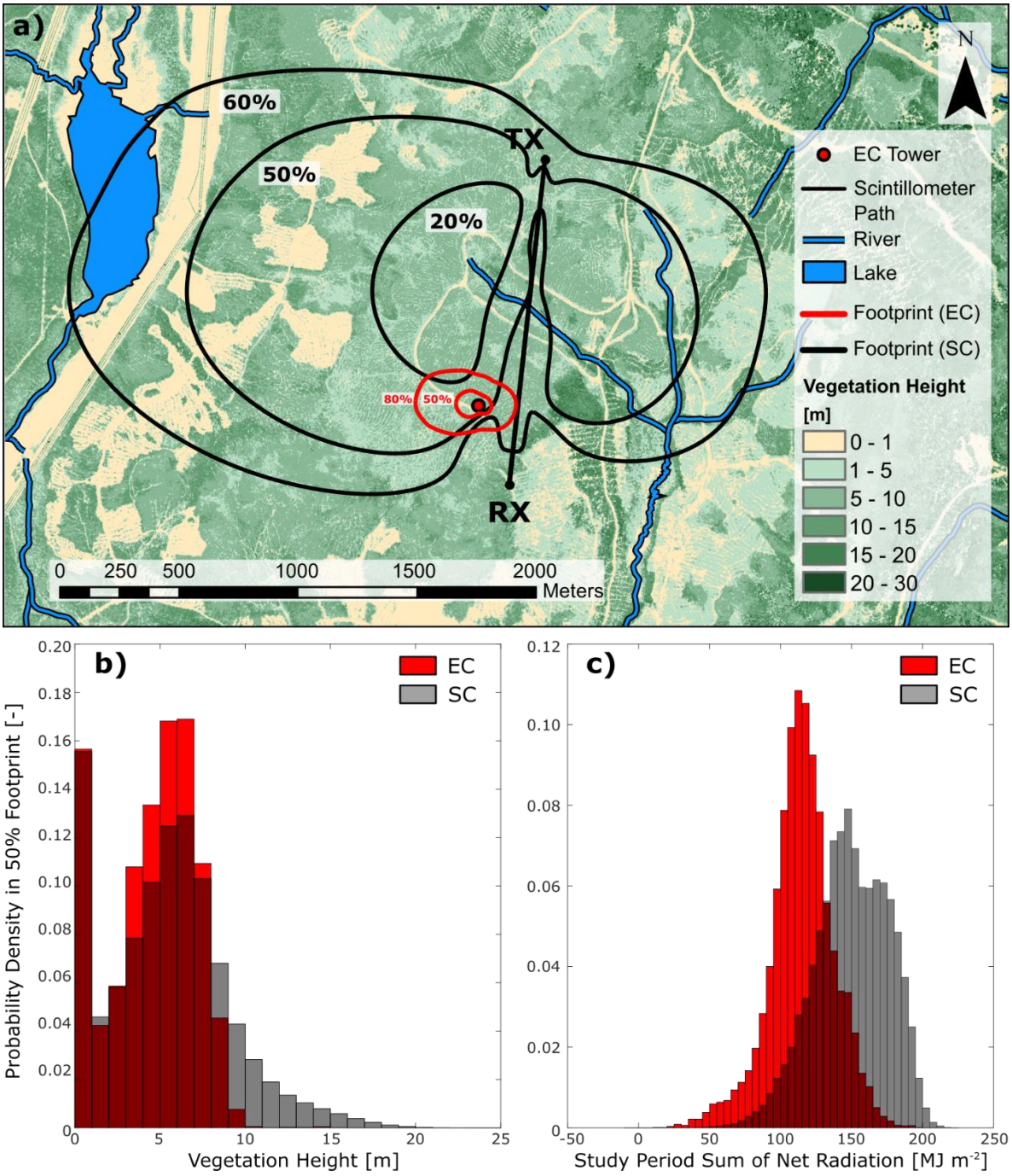

Figure 3.4: (a) Contour lines of the footprint contributions of the EC tower (red) and scintillometer systems (black), where the footprint is averaged over the 19 days of the study period, considering only unstable 30-min intervals. Each line delimits the source-area for an associated percentage of the total fluxes measured during the whole study period, *e.g.*, 80% of the EC fluxes during the 19 days came from the largest red zone. Footprints are shown over LIDAR derived vegetation height (Source: Ministère Forêts, Faune et Parcs du Québec). Bottom panels present probability density in the 50% footprint contribution contour lines of (b) vegetation height and (c) study-period (19 days) summed net radiation, for the EC tower (red) and scintillometer systems (black).

3.6.4 Complementary meteorological measurements

The four components of above-canopy radiation were measured at the EC tower by two net radiometers (CNR4, Kipp and Zonen, The Netherlands) installed at 15 and 10 m above the surface. Both devices were mounted parallel to the local ground slope (12° inclination and 30° aspect) to match the inclination of the EC system.

Storage of sensible and latent heat fluxes in the air between the ground and the EC system (ΔQ_H and ΔQ_{LvE}) were evaluated using a vertical profile of four temperature/humidity shielded probes (HC2S3 and HMP45C, Campbell Scientific, USA) installed at height 3.29, 5.68, 10.77 and 14.96 m above ground. Storage is calculated at each height and integrated over the whole vertical profile with equations:

$$\Delta Q_H = \sum_{i=1}^{4} c_{p,i}\rho_i \frac{\Delta T_i}{\Delta t}\Delta z_i \tag{3.25}$$

$$\Delta Q_{LvE} = \sum_{i=1}^{4} L_{v,i}\rho_i \frac{\Delta q_i}{\Delta t}\Delta z_i \tag{3.26}$$

where subscript i applies to the four measurement height for each variable; ΔT_i [K] and Δq_i [kg kg^{-1}] are the differences in T or q at height i between two timesteps of length Δt [s]; and Δz_i [m] is the air layer thickness associated with each measurement probe (*i.e.*, 4.49 m, 3.74 m, 4.64 m and 1.50 m from bottom to top probe, respectively). This method is derived from the generalized scalar conservation equation, by neglecting all terms except storage and flux divergence and assuming constant flux with height (Aubinet et al. (2012), see their equation 1.24). ΔQ_H and ΔQ_{LvE} were added to fluxes measured by the EC system.

Storage fluxes were also added to measured scintillometer fluxes to account for flux divergence with height: they were obtained by linearly scaling the EC tower storage fluxes to $z_{m,eff}$. This approximation was deemed plausible since it is generally assumed that fluxes decrease linearly with height in the boundary-layer. Furthermore, at the EC tower, temporal temperature and humidity gradients did not vary significantly with height. Indeed, storage fluxes calculated using only the bottom probe or only the top probe (the rest equal) varied by ≈1 W m^{-2} at the EC level or ≈8 W m^{-2} at $z_{m,eff}$, on average. Evidently, since both EC and scintillometer storage fluxes assume a constant flux layer, they are subject to the same uncertainties related to the validity of Monin-Obukhov similarity theory (see section 3.6.1.2 and 3.8).

For scintillometer fluxes and footprint calculations, measurements of T, q, U and WD were needed at the flux tower. A complete time series of T and q was obtained by merging the data from the four probes used to obtain EC storage fluxes. U and WD were obtained by merging EC measurements with values measured by wind vanes (05103, RM Young, U.S.A) installed at 8.53 m and 14.63 m on the EC tower.

3.6.5 Comparison scheme

Atmospheric conditions necessarily impact the comparison of fluxes measured by the EC tower and the scintillometer system. To quantify these effects, we calculated indicators that described the atmospheric conditions at the site and focus on surface-layer height, footprint similarity between setups in terms of vegetation height and solar radiation, and atmospheric stability. Values of these metrics for each day of the study period are presented in Table 3.1.

When the atmospheric surface-layer height is below the scintillometer path, it is expected that scintillometer measurements of fluxes are less reliable (Braam et al. 2012). To pinpoint these occurrences of $z_{m,eff} > z_{ASL}$, we evaluate the height of ASL with the common estimation $z_{ASL} = 0.1 z_{BL}$, where z_{BL} is the boundary-layer height. The former is obtained via the ERA-Interim reanalysis (Dee et al. 2011) every 3 hours and then linearly interpolated to a 30-min time step. This method is a coarse approximation of the actual z_{ASL}, probably unapplicable at times over the valley, but is a decent option in the absence of direct measurements. Table 1 presents the percentage of 30-min periods per day with $z_{m,eff} < z_{ASL}$ (PASL). In this study, we use the $z_{m,eff} < z_{ASL}$ criterion to ascertain performances of the scintillometer system compared to the EC system in evaluating surface fluxes in or outside the ASL.

To compare footprint between instrumental setups, we evaluate the footprint dissimilarity between the EC tower and the scintillometer systems based on vegetation height and solar radiation distribution inside each footprint area. Spatially-distributed vegetation height, slope inclination and aspect are obtained from a LIDAR survey performed in 2016 (see Figure 3.1). We isolate every 1-m pixels inside the 50% contribution contour line of both the scintillometer and EC daily-averaged footprints to create two system-specific distributions of vegetation height, slope inclination and slope aspect.

The vegetation height distributions are grouped into 30 1-m vegetation bins from heights of 0 m to 30 m and normalized into probability distribution functions by dividing each bin count by the total number of pixels in the total footprint area. An example of these probability distribution function is presented in Figure 3.4b.

Footprint vegetation dissimilarity (FVD) is then evaluated by comparing vegetation height probability distribution in the scintillometer and EC footprints ($P_{v,\mathrm{SC}}$ and $P_{v,\mathrm{EC}}$, respectively) using the following:

$$\mathrm{FVD} = \frac{1}{n}\sum_{i=1}^{n}\left|P_{v,\mathrm{SC},i} - P_{v,\mathrm{EC},i}\right| \tag{3.27}$$

where the *i* subscript refers to the vegetation height bin and *n* to the total number of bin, equal here to 30. In other words, FVD is the sum of probability deviations between systems in each vegetation height classes, meaning that lower values imply more comparable footprints. FVD is technically a relativized Manhattan distance

(Sokal and Michener 1967), particularly robust to differentiate ecological distributions (Faith et al. 1987). Values of daily FVD are presented in Table 3.1. In subsequent analyses, we contrast comparisons of instrumental systems between periods of low FVD (good footprint match) and high FVD (poor footprint match). The threshold between low and high FVD is taken as the 50th percentile of all 19 values of FVD (0.019).

The slope inclination and aspect distributions are used to assess the amount of solar radiation received over the footprint areas of each instrumental system. Theoretical cloudless solar radiation reaching each 1-m pixel is calculated with the radiation model of Whiteman and Allwine (1986). Net radiation measured at the EC tower is then rotated to the inclination and aspect of every 1-m pixel in the footprints using the method of Matzinger et al. (2003). With this method, measured solar radiation is split into diffuse and direct radiation using the model of Skartveit et al. (1998), specifically designed for northern latitudes. Only the direct proportion of radiation is rotated using the ratio between each 1-m pixel theoretical solar radiation and EC tower theoretical solar radiation. Diffuse fraction of solar radiation, albedo and upwelling and downwelling longwave radiation are assumed as constant over the whole study region. Site-specific net radiation is next summed over each days of the study period.

Daily-summed net radiation for all days, and over all 1-m pixels of both EC and scintillometer footprints varied between 0 and 17 MJ m^{-2}; distributions were hence grouped in 34 bins of 0.5 MJ m^{-2}. Footprint radiation dissimilarity (FRD) is then evaluated by comparing daily-summed radiation probability distribution in the scintillometer and EC footprints ($P_{r,\mathrm{SC}}$ and $P_{r,\mathrm{EC}}$, respectively) using the following:

$$\mathrm{FRD} = \frac{1}{n}\sum_{i=1}^{n}\left|P_{r,\mathrm{SC},i} - P_{r,\mathrm{EC},i}\right| \tag{3.28}$$

where the i subscript refers to the daily-summed radiation bin and n is the total number of bins equal to 34. Values of daily-averaged FRD are presented in Table 3.1. As for FVD, comparison between instrumental systems is made for low and high FRD, the threshold value being here at 0.032.

We also classified the radiation regime of a given day by the percentage of potential radiation (PRAD), defined as the daily sum of solar radiation measured at the site divided by the maximum potential solar radiation at the site calculated using the procedure developed by Whiteman and Allwine (1986). We arbitrarily define a clear-sky day with PRAD > 90%, a partially clouded day with 70% < PRAD < 90% and an overcast day with PRAD < 70%.

Atmospheric stability was assessed using the stability parameter $\zeta = (z_m - d_0) / L_{Ob}$ measured at the EC tower. For a given day, 30-min periods were flagged stable if $\zeta > 0.05$, unstable if $\zeta < -0.05$ and near-neutral otherwise. Percentages of unstable (PUNS), near-neutral (PNEU) and stable (PSTA) periods were taken as the number of periods falling in a given stability regime over the 48 30-min periods of the day. As L_{Ob} is sometimes unavailable

at the EC tower, PUNS + PNEU + PSTA is not always equal to one. Comparison between the scintilometer and EC systems calculated fluxes are then contrasted by atmospheric stability.

To compare fluxes measured with the scintillometer with those from the EC tower, we use the coefficient of determination R^2. This metric allows respecting the particularities of the instrumental setup: namely, fluxes from both systems were not measured on the same plane of reference (horizontal for scintillometer, inclined on a 12° northeast slope for EC). In this situation, metrics assessing the bias between methods are not strictly relevant, but correlation should still point to valid scintillometer fluxes.

3.7 Results

3.7.1 Structure parameter comparison

Figure 3.5 presents daily cycles of meteorological structure parameters and temperature-humidity correlations, measured with the EC and scintillometer systems, calculated using TW and BC for three days of the study period. Note that 26 August, 16 September and 21 September were partially clouded, overcast and cloud-free, respectively. Logarithmic-scale determination coefficient R^2 between structure parameters from the EC tower and from TW for the whole dataset is 0.21 and 0.54 for C_T^2 and C_q^2, respectively. These determination coefficients are low compared to other studies (*e.g.*, Ward et al., 2015b). However, they still indicate a correlation between systems, even with the substantial height difference, uncertainties associated with scaling of EC structure parameters, and the inclination of the EC instruments.

Atmospheric conditions are crucial when comparing meteorological structure parameters between different instrument systems. Correlation between EC and TW is maximized during near-neutral periods (R^2 is 0.39 and 0.63 for C_T^2 and C_q^2 respectively), but is worse when the atmosphere is stable (R^2 is 0.08 and 0.20 for C_T^2 and C_q^2, respectively), though not as worse under unstable conditions (R^2 is 0.31 and 0.41 for C_T^2 and C_q^2, respectively). Concisely, EC values of C_T^2 and C_q^2 track more closely with scintillometer values on 16 September 2017, an overcast day with frequent occurrences of near-neutral conditions. Those conditions are notably characterized by scaling coefficients closer to unity when adjusting EC structure parameters to $z_{m,eff}$.

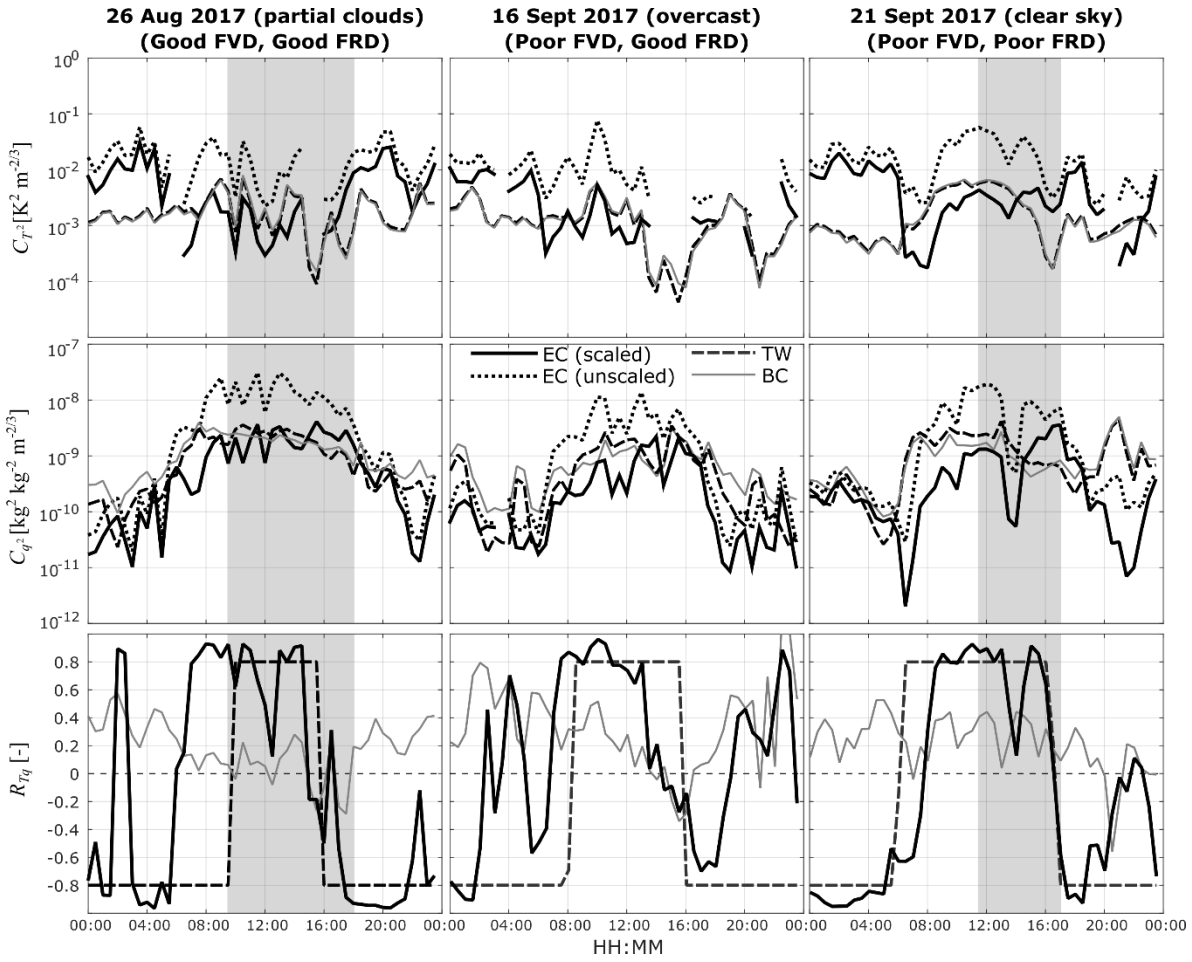

Figure 3.5: Daily cycles of C_T^2, C_q^2 and R_{Tq} (first, second and third row, respectively) for 26 August, 16 September and 21 September 2017 (first, second and third column, respectively). Different line types present variables measured with the EC tower, unscaled (dotted thick) or scaled to $z_{m,eff}$ (full thick), and calculated with the two-wavelength (TW, dashed) and bichromatic methods (BC, thin grey). Shaded zones means that $z_{m,eff} < z_{ASL}$. Footprint agreement is indicated on top of each rows based on footprint vegetation height dissimilarity (FVD) and footprint daily-summed net radiation dissimilarity (FRD), according to criteria from section 3.6.5.

Figure 3.5 also presents daily cycles of R_{Tq} for the EC tower and both scintillometer methods. The plots clearly show the relevance of the choice of $R_{Tq} = \pm 0.8$ for TW, as the EC tower data follow that trend quite well during the day. Oddly, R_{Tq} is almost always positive with BC, with a mean value of 0.08 during the day and 0.23 at night for the whole study period. Instances of nighttime positive temperature-humidity correlations at the EC tower happened 8% of the time, but agreement with BC was weak even then ($R^2 = 0.08$). Lüdi et al. (2005) mentions that values of R_{Tq} diminish at lower Bowen ratio values. This could explain lower daylight R_{Tq} values, since the Bowen ratio is under 0.5 for 52% of daylight hours at the site.

Ward et al. (2015b) point out that instances of weak winds crossing the scintillometer path can lead to poor performances of BC. In these cases, reduced temporal correlation for successive samples of scintillations are caused by an unapplicable frozen turbulence hypothesis (Poggio et al., 2000). This creates uncertainties in C_n

values, especially $C_{n,OMS}$, and hence also R_{Tq}. During our study, crosswind speed measured at the EC tower was under 2 m s^{-1} ~70% of the time. If we scale these crosswind speeds to $z_{m,eff}$ by inverting Equation 3.14, this number drops to ~19%. However, since the beam height was variable, more than 30% of its length experiences weak crosswind velocities a quarter of the time.

Nevertheless, average relative differences between meteorological structure parameters from TW and BC amount to 7% and 32%, while R^2 is 0.99 and 0.89 for C_T^2 and C_q^2, respectively, over the whole study period. As these relatively weak differences and strong correlations between methods extends to calculated fluxes, we elected to present only the fluxes obtained with TW. The choice was made considering the good agreement of R_{Tq} from TW with that of the EC tower.

3.7.2 Comparison of fluxes

Table 3.2 summarizes determination coefficients R^2 obtained by comparing scintillometer fluxes from the four calculation methods with EC fluxes, for several subsets of measurement periods. For all situations, a better correlation is obtained for TW_d, followed by BC_d, TW_i and BC_i, in that order. The generally good agreement of the fluxes can appear surprising, given the aforementioned discrepancies between meteorological structure parameters. It seems that the sensitivity of fluxes to other variables (L_{Ob}, u_*) can offset differences in C_T^2 or C_q^2.

As mentioned earlier, only TW fluxes are plotted for the scintillometer system because their structure parameters are more correlated with EC. Note however that fluxes calculated with BC structure parameters and the dependent method are very similar to those calculated with TW: comparison of values of fluxes from TW_d and BC_d yields R^2 values of 0.88 for H and 0.98 for L_vE. With the independent method, the sign and magnitude of fluxes are dictated by R_{Tq}: positive values indicate an unstable atmosphere, positive H and larger fluxes (via larger f_T and f_q) while negative values of R_{Tq} indicate stable atmosphere, negative H and weaker fluxes. Incidentally, the important differences of R_{Tq} calculated with TW or BC lead to numerous instances of fluxes with opposite signs, especially with H, and hence to poor correlation between TW and BC. As R_{Tq} from EC is better reproduced by TW, fluxes of the latter method correlate better than BC with EC (see Table 3.2).

Table 3.2: Correlation coefficient R^2 yielded by the statistical comparison of sensible and latent heat fluxes (including storage terms) measured by the EC tower versus that obtained by the four different scintillometer calculation methods (TW: two-wavelength; BC: bichromatic; each declined in its dependent (*d*) and independent (*i*) versions). Statistics are calculated for all periods and for specific complementary subsets: $z_{ASL} > z_{m,eff}$ or $z_{ASL} < z_{m,eff}$, good FVD (FVD < 0.019) or poor FVD otherwise, good FRD (FRD < 0.032) or poor FRD otherwise. Optimal conditions are the intersection of periods of $z_{ASL} > z_{m,eff}$, good FVD and good FRD, and non-optimal periods are all others. Results are also shown for unstable, near-neutral and stable conditions.

H				
Conditions	TW_i	TW_d	BC_i	BC_d
All	0.73	0.87	0.34	0.83
Optimal	0.81	0.90	0.73	0.88
Non-Optimal	0.73	0.86	0.31	0.82
$z_{ASL} > z_{m,eff}$	0.82	0.90	0.69	0.84
$z_{ASL} < z_{m,eff}$	0.70	0.84	0.27	0.82
Good FVD	0.72	0.85	0.42	0.80
Poor FVD	0.75	0.88	0.29	0.85
Good FRD	0.72	0.86	0.32	0.84
Poor FRD	0.75	0.88	0.36	0.82
Unstable	0.60	0.74	0.52	0.69
Near-Neutral	0.68	0.86	0.30	0.82
Stable	0.10	0.29	0.01	0.12
L_vE				
Conditions	TW_i	TW_d	BC_i	BC_d
All	0.73	0.83	0.39	0.79
Optimal	0.82	0.82	0.64	0.80
Non-Optimal	0.72	0.83	0.37	0.79
$z_{ASL} > z_{m,eff}$	0.81	0.79	0.63	0.77
$z_{ASL} < z_{m,eff}$	0.71	0.86	0.39	0.82
Good FVD	0.70	0.81	0.38	0.76
Poor FVD	0.77	0.85	0.41	0.81
Good FRD	0.74	0.83	0.43	0.79
Poor FRD	0.73	0.83	0.35	0.79
Unstable	0.49	0.64	0.29	0.56
Near-Neutral	0.65	0.71	0.31	0.65
Stable	0.02	0.32	0.06	0.34

In Figure 3.6, we plot side-by-side comparisons of TW_i and TW_d fluxes with EC fluxes, with associated linear regressions. The attribution of the EC flux sign to scintillometer fluxes is certainly the most beneficial feature of the dependent method for correlation between measurement systems. Before the addition of storage terms, the independent method never obtains negative L_vE fluxes by design, while the sum of negative storage-less L_vE_{EC} amounts to −1.45 MJ m^{-2} or 0.59 mm of dew deposition. Regarding *H*, there are numerous instances of TW_i and EC fluxes of opposite signs. If those were removed, R^2 would jump from 0.73 to 0.79, which is still below the 0.87 value obtained using atmospheric stability and friction velocity from the EC tower in calculations.

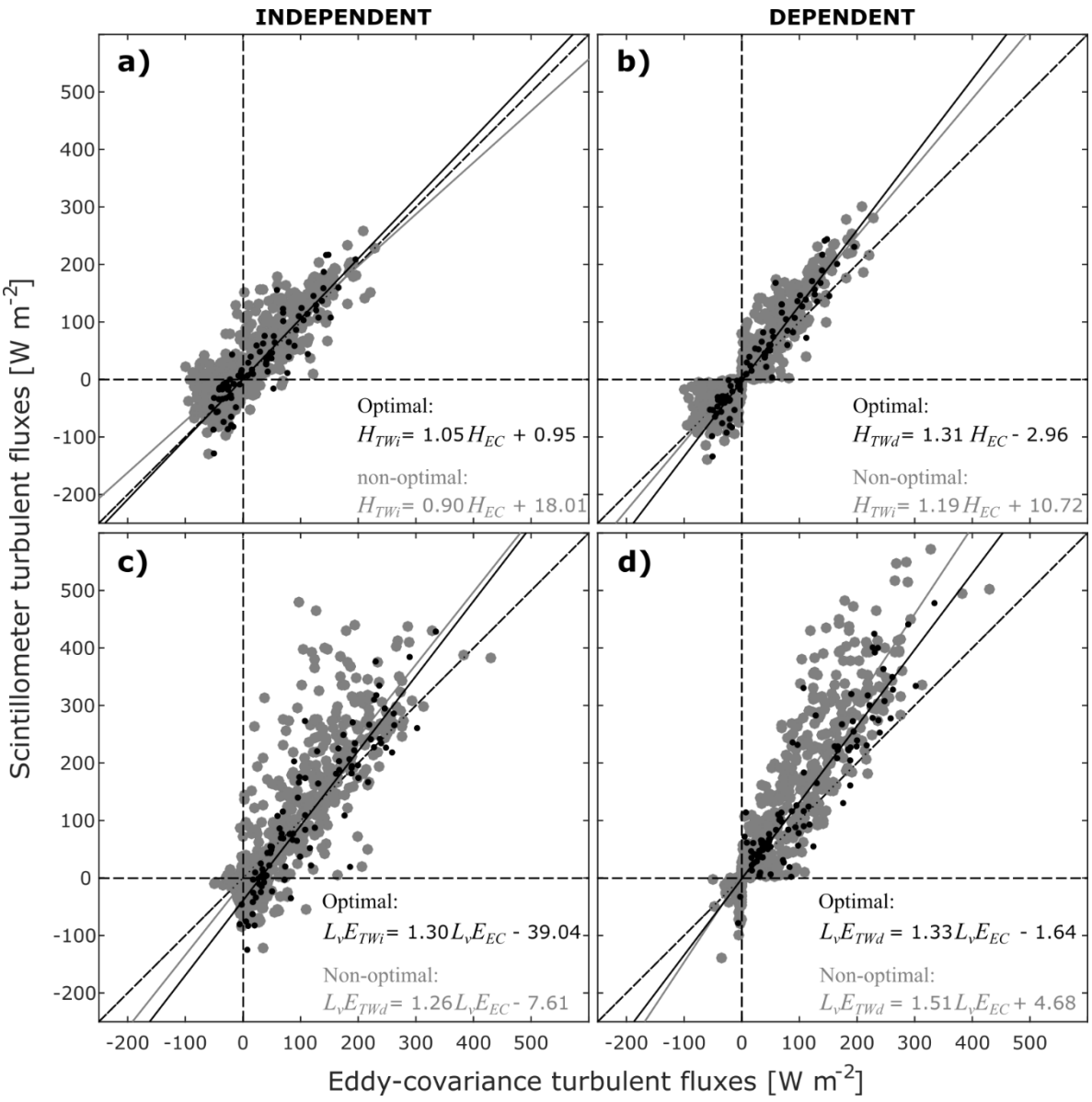

Figure 3.6: Side-by-side comparison between EC tower sensible heat fluxes H_{EC} and scintillometer sensible heat fluxes calculated with (a) the two-wavelength independent method H_{TWi}; (b) the two-wavelength dependent method H_{TWd}; and between EC tower latent heat fluxes L_vE_{EC} and scintillometer sensible heat fluxes calculated with (c) the two-wavelength independent method L_vE_{TWi}; (d) the two-wavelength dependent method L_vE_{TWd}. All presented fluxes include system-specific storage terms ΔQ_H and ΔQ_{LvE} (see section 3.6.4). Data are separated between optimal comparison periods, when $z_{m,eff} < z_{ASL}$ and footprints are similar, *i.e.* when FVD < 0.019 and FRD < 0.032 (black points and lines) or non-optimal comparison periods, *i.e.* when one of the aforementioned criteria is not met (grey points and lines). Each plot features the 1:1 line (dotted black) and linear regression lines (full lines), with associated equations.

Table 3.2 and Figure 3.6 also highlight the impact of comparing fluxes between EC and the scintillometer during optimal conditions, when $z_{ASL} > z_{m,eff}$ and footprints from both systems are in good agreement. Correlation improvements during optimal conditions however appear to be mostly attributable to the scintillometer beam being in the ASL. Regardless of the scintillometer flux calculation method used, correlation of fluxes with EC

always improves when $z_{ASL} > z_{m,eff}$, except with L_vE from dependent methods. We note, however, that with any fluxes, correlation is not much lower when $z_{ASL} < z_{m,eff}$, especially with dependent methods.

Surprisingly, comparison of fluxes from EC and scintillometer is not consistently affected by footprint similarity between instrumental systems. In terms of vegetation height, correlation of fluxes usually decreases from poor FVD to good FVD, except for H with the BC_i method. Regarding net radiation variability, days of good FRD have a slightly positive impact on L_vE fluxes comparison, but induces a decrease in correlation values for H, except for the BC_d method. We however note that correlation systematically increases with BC methods when going from conditions when $z_{ASL} > z_{m,eff}$ only to total optimal conditions. Also noteworthy is that in optimal conditions, the correlation difference between TW_d and BC_d is fairly weak (R^2 difference of 0.02).

In general, the scintillometer fluxes are larger in magnitude than the EC fluxes: the average values of the ratio of scintillometer fluxes to EC fluxes, including only periods when both fluxes are above 50 W m^{-2}, are 1.43 and 1.23 for H and 1.64 and 1.36 for L_vE using TW_d and TW_i, respectively. These ratios decrease during optimal conditions (1.36 and 1.20 for H and 1.36 and 1.19 for L_vE using TW_d and TW_i, respectively) while they usually increase otherwise (1.44 and 1.23 for H and 1.70 and 1.39 for L_vE with TW_d and TW_i, respectively).

Figure 3.7 presents daily cycles of TW_i, TW_d and EC turbulent fluxes, for the same three days of interest depicted in Figure 3.5. Scintillometer fluxes follow the EC fluxes quite well when $z_{m,eff} < z_{ASL}$ while larger values are reported in any conditions, especially with L_vE under unstable conditions (*e.g.* afternoon of 26 August and 21 September). With TW_i, scintillometer measurements generate important differences at night, with H being more negative and L_vE being more positive.

Correlation between instrumental systems are also highly related to atmospheric stability (measured at the EC tower), as can be seen inTable 3.2. All scintillometer flux calculation methods correlate better with EC under near-neutral circumstances (except H from BC_i), and are at their worst under stable conditions. When the atmosphere is stable, it is highly probable that the scintillometer measurement height is above the surface-layer height: in 85% of the stable 30-min periods, $z_{m,eff} > z_{ASL}$. Moreover, in 43% of the stable 30-min periods, the boundary-layer height estimated with ERA-Interim reanalysis is under $z_{m,eff}$. Under these conditions, the scintillometer effective height technically falls beyond the applicability range of Monin-Obukhov similarity theory. It is also well-known that applying Monin-Obukhov similarity theory in stable boundary layers is more challenging due to the presence of internal gravity waves, intermittent turbulence, low-level jets and other events (Cheng et al., 2005). Scintillometer-derived fluxes should therefore be considered with caution when the atmosphere is stable.

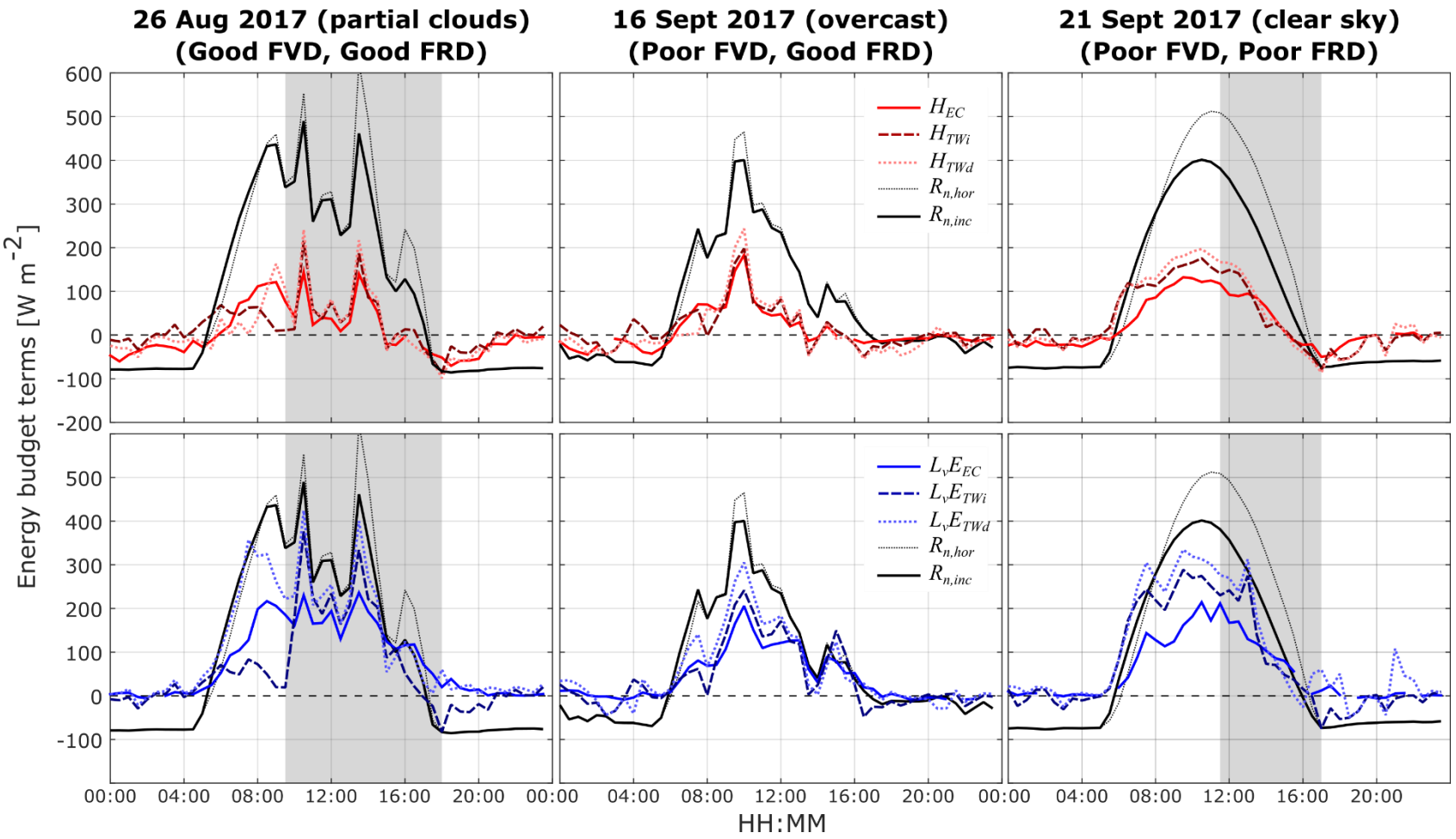

Figure 3.7: Daily cycles of H and L_vE (first and second rows, respectively) for 26 August, 16 September and 21 September (first, second and third columns, respectively). Different line types present variables measured with the EC tower (H_{EC} and L_vE_{EC}, thick lines) and calculated with the two-wavelength independent (H_{TWi} and L_vE_{TWi}, dashed lines) and two-wavelength dependent methods (H_{TWd} and L_vE_{TWd}, dotted lines). All presented fluxes include system-specific storage terms ΔQ_H and ΔQ_{LvE} (see section 3.6.4). Net radiation is presented on each graph: $R_{n,inc}$ (black lines) is measured at the EC tower, parallel to the 12° northeast slope, while $R_{n,hor}$ (dotted black lines) is $R_{n,inc}$ rotated to an horizontal surface using the method of Matzinger et al. (2003). Shaded zones mean that $z_{m,eff} < z_{ASL}$, and footprint agreement is indicated on top of each rows based on footprint vegetation height dissimilarity (FVD) and footprint daily-summed net radiation dissimilarity (FRD), according to criteria from section 3.6.5.

Table 3.2 also quantifies the impact of feeding friction velocity, atmospheric stability and flux sign from EC to scintillometer flux calculations (the so-called dependent method) on the correlation between both setups for different stability classes. With TW, under stable conditions, H and L_vE correlations increase by a substantial margin, from R^2 values of 0.10 to 0.29 and 0.02 to 0.32, respectively. Given that scintillometer fluxes are often questionable during stable conditions, it is expected that inputs from a reliable method like EC improves fluxes comparison. Yet, the dependent method still increases correlation under unstable conditions, when both setups are theoretically reliable.

The comparison between EC and the scintillometer setup also appears to be influenced by the type of radiation regime of a given day. Indeed, a weak correlation is detectable between the ratio of TW to EC daily-summed sensible heat fluxes (under daylight) and PRAD (R^2 equals 0.41 and 0.29 for the comparison between EC and TW_i or TW_d, respectively). Namely, when measured radiation on a given day increases, H_{TWi}/H_{EC} also increases, with ratios between 0.72 (at PRAD = 0.57) and 2.09 (at PRAD = 0.95). Similar, but weaker, trends are seen with latent heat fluxes (TW_i: R^2 = 0.34, TW_i: R^2 = 0.00).

3.8 Discussion

Our results show that fluxes measured by a scintillometer and by EC tower are more correlated when the electromagnetic beam travels in the atmospheric surface-layer. This is not surprising, as Braam et al. (2012) have shown that scintillometer measurements above z_{ASL} may not be coupled with surface fluxes. The authors especially point to the morning transition, when it takes time for the ASL to thicken, meaning that $z_{m,eff}$ might be below z_{ASL} even if conditions are unstable. Even so, the correlation between methods in our study does not decrease much with shallow ASL, which is intriguing.

Our results show that fluxes measured by a scintillometer and by EC tower are more correlated when the electromagnetic beam travels in the atmospheric surface-layer. This is not surprising, as Braam et al. (2012) have shown that scintillometer measurements above z_{ASL} may not be coupled with surface fluxes. The authors especially point to the morning transition, when it takes time for the ASL to thicken, meaning that $z_{m,eff}$ might be below z_{ASL} even if conditions are unstable. Even so, the correlation between methods in our study does not decrease much with shallow ASL, which is intriguing.

Some hypotheses may explain such behaviour. First, the highly variable electromagnetic beam height is probably very influential. Even when $z_{m,eff} > z_{ASL}$, a certain proportion of the scintillometer path is still within the ASL. In fact, the average percentage of the beam within the ASL when $z_{m,eff} > z_{ASL}$ is $\sim$ 20%, and varies between 0% and $\sim$ 74%. In addition, boundary-layer height, and thus ASL height, is obtained from a regional reanalysis.

Uncertainties stem from the ERA-Interim model and from its spatial and temporal representativeness. Despite its importance, it appears the $z_{m,eff} > z_{ASL}$ scintillometer applicability condition has to be enforced with flexibility.

Weak –or even negative– influence of footprint similarity on correlation between EC and scintillometer fluxes appears counterintuitive. Several causes can be listed for this behavior. First, considerable difference in footprint area can make the comparison between scintillometer and only one EC tower difficult. Evans et al. (2012) showed that comparison between scintillometer fluxes and aggregation of several EC fluxes was much better than comparison with individual EC fluxes. Also, our footprint characterization scheme, however detailed, can overlook some important variables (*e.g.* transition between heterogeneities, moisture sources at the bottom of the valley, higher weight of the fluxes near peak footprint value, etc.).

In addition, several uncertainties are tied with the footprint calculation methodology. First, some inputs to the FFP method have to be extrapolated from the EC tower to the scintillometer system (U or z_0, σ_v, u_*, L_{Ob}, and WD). Each can vary significantly with height and horizontally across the valley. Second, the FFP method itself was obtained using Lagrangian stochastic particle dispersion simulations that were all over flat and homogeneous grounds. Given the on-site complex topography, it is probable that the larger extent of the footprint contour lines are erroneous. We try to avoid this by focusing on the 50% contribution lines, but uncertainties still remains. Finally, the choice of using daily-averaged footprints, which was done to reduce computational time, can possibly hide the footprint influence if wind direction is highly variable during the day. Note however that this is rare: during our study period, the wind came from between 225° and 315° for 65% of the time.

Other sources of uncertainties have to be mentioned regarding scintillometer fluxes. The largest is probably induced by the choice of similarity functions f_T and f_q used to obtain the temperature and humidity scales (T_* and q_*). Kooijmans and Hartogensis (2016) specified uncertainties associated with the coefficients they provide: over our study period, they amount to ≈2% of scintillometer fluxes. It is however well-known that these functions are much less reliable and can induce large scatter during neutral and stable conditions (Ward et al., 2015a), and also over complex terrain in general (*e.g.*, Nadeau et al., 2013; Sfyri et al., 2018). Promising studies addressing this problem exist (*e.g.*, Sfyri et al., 2018; Stiperski et al., 2019), but for now, we followed the methodology recommended by (Ward, 2017).

Uncertainties also arise from the determination of $z_{m,eff}$, d_0 and z_0. First, the effective height is calculated using the stability-independent formula of Hartogensis et al. (2003). However, we tested their stability-dependent formulation, and for the range of ζ observed during the study period, $z_{m,eff}$ varies only by about 2%. As for d_0 and z_0, they vary strongly along the scintillometer path if we calculate them using only vegetation height under the beam. Indeed, d_0 varies between 0.05 and 8.6 m while z_0 is between 0.007 and 1.29 m. However, these discrepancies translate only in H and L_vE increasing by 4% or decreasing by 3%. Clearly, these uncertainties

are small, as was the case with previous studies (Hartogensis et al., 2003; Ward et al., 2014; 2015a), and average values are amply suitable.

Comparing independent and dependent scintillometer flux calculation methods, it is clear that the input of some EC tower data improves correlations between both measurement systems. This result is also not surprising given the strong relationship between fluxes and friction velocity or Obukhov length. Even then, scintillometer fluxes still differ from EC, and these discrepancies may be caused by differing source areas. Scintillometers are meant to be stand-alone devices to measure area-averaged fluxes, but the inputs of nearby EC tower may improve their measurements. More studies are needed to confirm this.

Caution is required when feeding EC data to scintillometer flux calculations. Friction velocity is well-correlated between measurement systems (R^2 =0.61 between TW_i and EC), but its measured amplitude is about twice as high at the EC tower, close to the rough boreal forest surface. Atmospheric stability is also different at the scintillometer level, with $|\zeta_{EC}| < |\zeta_{TW}|$. These differences may very well be the result of differing measurement heights or source-areas rather than limitations of the scintillometer setup.

Moreover, instances of opposite sign stability occurred ~13% of the time, often during the morning transition from a stable to an unstable atmosphere. The attribution of EC flux sign to scintillometer fluxes during morning transitions might be incorrect. Indeed, EC fluxes are measured on a northeast-facing slope, while the scintillometer measures fluxes from the whole valley, which includes the flat portion and the southwest-facing slope. This leads to quite different sums of net radiation received over the whole study period (see Figure 3.4c). At the sub-daily time scale, because of its exposure, the northeast slope net radiation starts to rise earlier than the rest of the valley (Whiteman and Allwine, 1986; Holst et al., 2005). It is entirely possible that sensible heat fluxes measured with both systems follow that trend, where H_{EC} begins to increase before the scintillometer counterpart. This would lead to actual fluxes of opposite signs between instrumental setups, an effect the dependent method would erase.

Even if EC fluxes are taken as the benchmark in this study, uncertainties still exist. Random uncertainties evaluated using the Finkelstein and Sims (2001) method amount to ~12% of total H or L_vE fluxes over the 19-day study period. It is also worth remembering that EC fluxes are measured normal to the 12° northeast-facing slope, and that a direct comparison with the basically flat buoyancy-driven fluxes of the scintillometer warrants discussion. Using Oldroyd et al. (2016) methodology, we compared our slope-normal measured fluxes with calculated vertical fluxes. Ratios of vertical to slope-normal fluxes took average values of 0.98 with standard deviation of 0.02, meaning that the EC slope-normal fluxes are highly comparable to vertical fluxes. Nevertheless, we specifically compared fluxes based on correlation, because biases or other indicators might vary solely because of different reference frames. However, even decreases in correlation might be physically

explainable and attributed to differing measurement angles (*e.g.*, the aforementioned differential heating of the valley by net radiation at the morning transition). Also, the energy budget did not fully close during our study period, as is commonly the case (Foken, 2008). The sum of turbulent fluxes amount to 58% of available energy on average over the study period (78% during daylight, 36% during nighttime).

Considering all this, results presented in this study provide some very valuable insights on the behaviour of scintillometer measurements across a boreal-forested valley. First, "surface" EC fluxes and higher altitude scintillometer measurements correlate to a higher standard when the scintillometer beam travels in the ASL. However, the scintillometer still provides realistic flux magnitudes in other circumstances, with mean absolute differences for all fluxes and methods between 26 and 53 W m^{-2}. Nevertheless, nighttime scintillometer measurements should be handled with extreme care, as they often yield unrealistic fluxes. During the day, sensible heat fluxes appear to be well-quantified by the scintillometer, but latent heat fluxes are subject to overestimation. In light of this study, we put forward that scintillometers can provide reliable fluxes above boreal-forested valleys, especially during the day when the ASL rises above all or parts of the scintillometer light-beam.

3.9 Conclusion

This study featured measurements of turbulent fluxes above a shallow boreal-forested valley using a two-wavelength scintillometer setup and an EC tower. Data were compared for 19 days between 11 August and 28 September 2017. Two methods were tested to obtain structure parameters from scintillometer measurements: the two-wavelength method, with fixed temperature-humidity correlation (R_{Tq} = ±0.8), and the bichromatic method that uses the covariance between LAS and MWS to obtain temperature-humidity correlations. Also, two methods were used to compute turbulent fluxes from structure parameters: the independent method used only scintillometer data, while the dependent method included atmospheric stability, friction velocity and flux sign taken from the EC tower. The comparison was performed to validate the use of two-wavelength scintillometry in non-flat forested topography, and the impacts of calculation methods and atmospheric conditions on turbulent fluxes.

Results show that the scintillometer provides coherent measurements despite the unorthodox instrumental setup. The comparison of structure parameters between measurement methods yields positive weak correlation, but the instruments height difference made that predictable. Temperature-humidity correlation from the two-wavelength (TW) method has a much better agreement with EC than the bichromatic (BC) method. Despite weak correlations between instruments at the structure parameter level, comparison of turbulent fluxes yields good determination coefficients. Coherently with structure parameter results, the two-wavelength method fluxes agree best with EC fluxes.

The comparison of instrumental setups produces better correlation when the effective height of the scintillometer path is fully in the atmospheric surface-layer than otherwise, but the improvements are not large. Variable beam height along the path means that lots of time, even if the effective height is not within the ASL, parts of the scintillometer measurement volume still are. This may explain the good agreement when shallow ASL are reported. Correlation between EC and scintillometer is best during near-neutral and unstable periods, but is very weak during stable periods. In fact, during nighttime, turbulent fluxes from scintillometers are often unrealistic.

Naturally, scintillometer fluxes are more in line with EC fluxes with dependent methods, when atmospheric variables measured at the EC tower are input in the scintillometer flux calculations. This could prove quite helpful to obtain realistic fluxes during stable/nighttime conditions, but more studies are needed to ascertain the validity of such methods. At morning transition periods, dependent methods could well be flawed with our instrumental setup, where the EC tower is on a northeast-exposed slope hit by solar radiation before the rest of the valley. This feature made it difficult to evaluate the relevance of dependent methods on sunny mornings.

To conclude, this study proved that scintillometer measurements are relevant for evaluating fluxes above forested valleys. Fluxes definitely appear to be reliable during days with deep atmospheric surface-layer, and often otherwise during daylight. More studies are definitely needed to further our understanding of the atmospheric behaviour.

3.10 Acknowledgments

The authors acknowledge all Montmorency Forest staff, especially Patrick Pineault and Charles Villeneuve, for their extremely valuable help in the field. We also would like to thank Annie-Claude Parent, Dany Crépault, Denis Jobin, Gonzalo Leonardini, Bram Hadiwijaya, Achut Parajuli, Laurie Migneault, Carine Poncelet, Antoine Thiboult, Guillaume Frédéric Hazemann, Jonas Götte and Julie-Anne Pelletier-Bergeron for their help installing and maintaining the scintillometer towers. This work was supported by the Natural Sciences and Engineering Research Council of Canada (NSERC), Ouranos Consortium, Hydro-Québec, Environment and Climate Change Canada, and Ministère de l'Environnement et de la Lutte contre les Changements climatiques (MELCC), through NSERC project RDCPJ-477125-14, by the Canadian Foundation for Innovation - John R. Evans Leaders Fund #33869, and by the the Fonds de recherche du Québec - Nature et Technologies (FRQNT).

Conclusion générale

Cette thèse a porté sur l'analyse du bilan d'énergie de surface d'une forêt boréale humide aux échelles ponctuelles, locales et régionales. Chaque chapitre répond à un objectif lié à une échelle spatiale de mesure du bilan d'énergie. Le fil conducteur de la thèse est cette gradation de l'échelle spatiale pour une compréhension accrue du bilan d'énergie et de l'évapotranspiration en milieu boréal. Ce type d'étude est fait pour la première fois dans une sapinière à bouleau blanc, un sous-domaine bioclimatique à la limite sud du milieu boréal et caractérisé par des précipitations plus fréquentes. Plus encore, le site d'étude principal, la forêt Montmorency, reçoit un des volumes annuels de précipitation les plus importants au pays. De plus, les installations se trouvent au sein d'une topographie prononcée, fait rare dans les études de bilan énergétique. De ce fait, les résultats de cette thèse, portant sur le bilan d'énergie et l'évapotranspiration dans une forêt boréale humide accidentée sont très novateurs.

Dans le premier chapitre, nous étudions l'effet de l'hétérogénéité spatiale du couvert forestier à l'échelle ponctuelle sur le bilan d'énergie et l'évapotranspiration. Vingt (20) stations mesuraient le rayonnement solaire sous-canopée à la fin de l'été 2016. La mesure continue du rayonnement solaire au-dessus de la canopée à la tour à flux Juvénile permettait ensuite de calculer la transmission du rayonnement en 20 points. Nous avons quantifié l'hétérogénéité spatiale du couvert forestier à l'échelle ponctuelle : pour la saison, la transmission du rayonnement solaire varie entre 7% et 69%, ce qui permet de calculer un indice de surface foliaire variant entre 1,11 et 6,29 $m^2\ m^{-2}$. La variabilité temporelle de la transmission est liée à la position des trouées dans la canopée et à la nébulosité. La position des trouées crée une variabilité importante à l'échelle temporelle demi-horaire, puisque le rayonnement direct peut être obstrué par les branches et aiguilles, mais aussi traverser librement le couvert. La nébulosité annule en partie ou totalement le rayonnement direct, ne laissant que le rayonnement diffus, qui sous la canopée ne dépend que de la fraction ouverte du ciel.

Dans ce contexte, les résultats montrent qu'un modèle simple de transmission du rayonnement, la loi de Beer-Lambert, permet de bien reproduire les observations saisonnières. Ceci est possible, car la couverture nuageuse fréquente rend le rayonnement solaire fortement diffus. Il est intéressant de constater que la comparaison de la moyenne spatiale des 20 observations concorde très bien avec le modèle de Beer-Lambert paramétré avec la moyenne des indices foliaires. Également, il appert que l'indice foliaire moyen des 20 stations (3.37 $m^2\ m^{-2}$) est très près de la valeur obtenue par approximations satellitaires MODIS (3.36 $m^2\ m^{-2}$). Ces résultats sont de bon augure pour le modélisateur qui souhaite représenter une forêt boréale juvénile très hétérogène à petite échelle spatiale comme une moyenne spatiale de plus grande échelle.

Étant donné la bonne performance de la loi de Beer-Lambert, les valeurs d'indices foliaires obtenues à chacune des 20 stations ont été utilisées pour paramétrer le schéma de surface CLASS et ainsi évaluer la variation d'évapotranspiration et de ses composantes de point en point. Les résultats de modélisation montrent qu'une végétation plus dense mène à plus d'évapotranspiration totale, car on note une plus grande évaporation des précipitations interceptées et une plus grande transpiration. Notons que cette végétation plus dense mène toutefois à une réduction de l'évaporation au sol.

Durant les périodes plus sèches, ce dernier phénomène conduit à un sol plus humide avec une végétation plus dense. Cependant, nos résultats semblent montrer qu'avec assez de jours de sécheresse, une végétation plus dense assècherait plus le sol par la transpiration. Il est toutefois impossible de conclure sur ce point, car la forêt Montmorency se retrouve rarement en longue période sans précipitations. Lors d'épisodes de précipitations intenses, les effets de la densité de végétation sur l'humidité du sol sont annulés, puisque les stockages d'eau dans les arbres et dans le sol sont comblés. Ainsi, un paramétrage juste du couvert forestier semble plus important en milieu sec que dans une forêt boréale humide.

Dans le deuxième chapitre, nous étudions l'effet des hauts volumes de précipitations enregistrés à la forêt Montmorency sur le bilan énergétique et l'évapotranspiration mesurés à l'échelle locale. Au site d'étude, deux tours à flux appliquent la covariance des tourbillons et mesurent les autres termes dominants du bilan d'énergie depuis l'automne 2015, pour trois années complètes de données (2016-2018). Dans un premier temps, nous comparons le bilan d'énergie et l'évapotranspiration et la précipitation au site principal avec ceux de 13 autres sites situés en forêt boréale dans le monde (10 en Amérique du Nord, 3 en Europe). Les sites de comparaison incluent cinq types de végétation parmi les plus dominants de la forêt boréale mondiale : les épinettes noires (six sites), les pins gris (trois sites), les pins sylvestres (deux sites), les peupliers faux-trembles (un site) et une végétation mixte (un site).

Au niveau du bilan d'énergie, tous les sites montrent une tendance claire pour la forêt boréale : lorsque la fonte de la neige démarre, les flux de chaleurs sensibles croissent avec le rayonnement net. Puis, lorsque la saison de croissance démarre, les flux de chaleur latente occupent une part variable du bilan d'énergie : les sites occupés par des pins ne génèrent pratiquement jamais des flux de chaleur latente dépassant ceux de chaleur sensible ($Bo > 1$), alors que les sites couverts de feuillus et de sapins baumiers produisent plus de flux de chaleur latente que de chaleur sensible ($Bo < 1$). Les sites avec des épinettes noires vont varier entre les deux comportements, dépendant du volume de précipitations reçu.

La forêt Montmorency se distingue nettement des autres sites de par la quantité importante de précipitations reçues. Une tendance claire se dessine où l'augmentation du volume de précipitation annuel est habituellement accompagnée d'une augmentation du volume d'évapotranspiration annuel. Les climats plus secs vont toutefois

causer une évapotranspiration qui occupe une plus grande proportion des précipitations, puisque la demande évaporatoire de l'atmosphère est plus substantielle. La forêt Montmorency évapore ainsi le plus grand volume d'eau, mais dans une des plus faibles proportions de la précipitation reçue. Il semble qu'une limite écohydrologique est présente à ~550 mm a^{-1}, celle-ci causée soit par la capacité de croissance biologique des espèces jumelée à une courte saison de croissance, soit par le fait que l'augmentation des précipitations implique une couverture nuageuse plus fréquente qui réduit ainsi la demande évaporatoire de l'atmosphère.

Grâce aux tours à flux de la forêt Montmorency, aux mesures de précipitations d'une station gouvernementale et aux mesures de débits à l'exutoire du bassin versant de 3,5 km^2, un bilan hydrologique sommaire a pu être établi pour les deux années hydrologiques à l'étude (2016-2017 et 2017-2018, octobre à octobre). Les précipitations atteignent environ 1600 mm a^{-1}, alors que l'évapotranspiration compte pour environ 550 mm a^{-1}, et approximativement 14% de ce volume serait de la sublimation. L'excès d'eau amené par les précipitations quitte le bassin majoritairement sous forme de débit dans les cours d'eau : le débit sortant est d'environ 1050 mm a^{-1}. Ce comportement est typique des bassins de tête en région montagneuse, et comme pour la plupart des bassins boréaux, la majorité de ce débit est durant la fonte de la neige. Ce type de bassin est crucial pour les sections en aval de ces grandes rivières, où se trouvent habituellement les populations humaines.

Dans le troisième chapitre, nous avons comparé des mesures du bilan d'énergie et de l'évapotranspiration à l'échelle locale avec un dispositif de scintillomètres à deux longueurs d'onde pour obtenir des mesures à l'échelle régionale. Ces instruments ont été déployés en août et septembre 2017, et 19 journées ont été retenues pour l'analyse. Le trajet des ondes électromagnétiques surplombait la vallée à des hauteurs entre 5 et 100 m, avec une hauteur effective de 88 m. Ce montage expérimental était en soit un défi important, mais notre analyse des données était extrêmement rigoureuse et selon les règles de l'art. Nous avons testé deux méthodes pour obtenir les paramètres de structure météorologiques : la méthode des deux longueurs d'onde et la méthode bichromatique. Également, deux méthodes d'obtention des flux turbulents ont été mises de l'avant : une méthode indépendante utilisant seulement les données des scintillomètres, et une méthode dépendante utilisant quelques données mesurées à la tour à flux (stabilité atmosphérique, vitesse de friction, signe des flux). Les scintillomètres et la tour à flux ont été comparés sur la base de la corrélation entre leurs flux turbulents, puisque toute autre métrique d'erreur absolue ou relative pourrait être non applicable étant donné des différences importantes entre les montages.

Les résultats montrent que la comparaison des paramètres de structure météorologique entre les deux montages donne une corrélation positive, mais faible. Ce résultat était attendu étant donné la différence importante de hauteur entre les instruments. Les flux turbulents mesurés avec les deux montages expérimentaux présentent toutefois une bonne corrélation. Au final, la méthode à deux longueurs d'onde a été

choisie comme la plus adéquate pour obtenir les paramètres de structure météorologiques, puisqu'elle génère une corrélation température-humidité plus cohérente avec celle de la tour à flux, et une meilleure corrélation avec les flux turbulents de la tour à flux.

En général, les flux turbulents mesurés avec les scintillomètres corrèlent mieux avec ceux de la tour à flux lorsque le faisceau électromagnétique est entièrement dans la couche de surface atmosphérique, mais les résultats ne sont pas désastreux autrement. La hauteur variable du faisceau peut être en cause, puisque même si le faisceau n'est pas entièrement dans la couche de surface atmosphérique, une certaine proportion du volume de mesure y est toujours. Les scintillomètres mesurent toutefois des flux beaucoup moins réalistes en périodes où l'atmosphère est stable, particulièrement la nuit.

Naturellement, la méthode dépendante de calcul des flux procure une meilleure corrélation entre les deux montages expérimentaux. Ce fait pourrait être très utile lorsque les scintillomètres seuls donnent des résultats douteux, comme la nuit. Il est toutefois important de considérer que l'injection de données provenant de la tour à flux peut être un choix erroné dans certaines situations, comme à la transition matinale sur notre site. En effet, la tour à flux est installée sur une pente faisant face au nord-est, et elle est donc illuminée plus tôt que le reste de la vallée. Ainsi, il est fort probable qu'elle passe d'une atmosphère stable à instable avant le reste de la vallée, auquel cas utiliser sa valeur de stabilité mesurée pour les scintillomètres pourrait engendrer des erreurs.

La combinaison des résultats des trois chapitres permet de tirer quelques conclusions sur le passage d'une échelle spatiale à une autre, un sujet de haute importance pour les modélisateurs du climat et de l'hydrologie. Le premier chapitre est particulièrement éloquent sur la conversion de plusieurs points de mesure à l'échelle ponctuelle vers l'échelle locale. Nos mesures à l'échelle ponctuelle permettent d'obtenir un PAI pour modéliser l'évapotranspiration. Or, la moyenne de ces valeurs d'évapotranspiration corrèle très bien avec les observations à l'échelle locale. De plus, l'adéquation presque parfaite entre la moyenne des 20 valeurs de PAI obtenues indirectement par nos mesures et la valeur obtenue par mesures satellitaires, bien que possiblement due au hasard, est très encourageante. En effet, elle semble valider l'aggrégation spatiale faite par le satellite et permet de croire qu'une moyenne spatiale de modélisation ponctuelle de l'évapotranspiration peut représenter des échelles plus larges. Ceci dit, il est évident que ces conclusions sont probablement possibles en terrain homogène seulement. De plus, il semble que la forte proportion de périodes nuageuses au site d'étude est cruciale, puisqu'elle légitimise l'applicabilité de la loi de Beer-Lambert et donc de l'évaluation des indices foliaires.

Le passage entre les échelles locales et régionales est moins clairement défini du fait que les résultats du troisième chapitre sont très exploratoires. Les mesures des flux turbulents sont faites aux échelles locales et régionales. L'empreinte de mesure des deux appareils est relativement semblable au niveau de la végétation,

mais diffère en termes d'ensoleillement. Au final, les scintillomètres semblent obtenir des flux turbulents plus élevés que la tour à flux. Ces différences peuvent s'expliquer par l'ensoleillement plus grand pour les scintillomètres, et aussi par la non-fermeture du bilan d'énergie avec la tour à flux. En effet, pour l'année 2017, la fraction de fermeture (*i.e. CF*, voir chapitre 2) est d'environ 86%. Ainsi, nos mesures à l'échelle locale ne sont probablement pas assez représentatives de la région pour être extrapolée spatialement. Néanmoins, il est possible d'imaginer qu'une extrapolation soit possible pour un territoire homogène et commun aux deux échelles spatiales.

Plusieurs aspects restent à explorer dans les trois chapitres de la thèse. Le premier chapitre présente la variabilité de l'évapotranspiration et de ses composantes sur la base de résultats de modélisation avec CLASS seulement. Dans l'idéal, d'autres schémas de surface devraient être testés pour confirmer la validité des conclusions. Il serait également intéressant de visualiser la performance de ces schémas de surface sur de plus longues périodes, notamment sur plusieurs années. De plus, il serait adéquat d'obtenir des mesures précises du partitionnement de l'évapotranspiration. Des mesures de la transpiration sont possibles avec des mesures de flux de sève. Des instruments utilisant la covariance des tourbillons, installés sous la canopée, pourraient permettre la mesure de l'évaporation au sol, tout comme des lysimètres.

Le deuxième chapitre présente parfois des bilans énergétiques ou hydriques incomplets, et la mesure des termes manquants serait souhaitable. Pour les sites de comparaison, les mesures du flux de chaleur dans le sol ou du stockage d'énergie dans l'air et dans la canopée étaient souvent manquantes dans les données obtenues sur Fluxnet. L'inclusion de ces termes pourrait permettre un meilleur ajustement de la fermeture du bilan d'énergie, quoique l'amélioration ne soit pas immense quand ces termes sont disponibles. Pour le bilan d'eau du bassin versant de la forêt Montmorency, la mesure du stockage d'eau dans le sol est aussi manquante, mais des travaux sont en cours pour rectifier cela. Comme il est mentionné dans l'article, sur une base annuelle, ce terme doit toutefois être négligeable, puisque les précipitations abondantes laissent peu de place à une variation du stockage en eau dans le sol, qui reste près de son maximum année après année.

Le troisième chapitre présentait une phase exploratoire de la méthode de la scintillométrie à deux longueurs d'onde dans un contexte de vallée couverte d'une forêt boréale humide. Des limitations techniques n'ont pas permis d'accumuler autant de données que prévu, ce qui aurait été appréciable et aurait permis des conclusions plus soutenues. Les résultats sont néanmoins encourageants dans les circonstances. L'ajout d'une ou plusieurs tours à flux sur les autres versants de la vallée aurait complété notre étude avec brio, mais les défis techniques de tels montages sont non négligeables. Une prochaine étude sur une topographie moins accidentée, mais un couvert forestier semblable, mais incluant des hétérogénéités, pourrait permettre de statuer sur la possible mise à l'échelle supérieure des flux mesurés avec une tour à flux en milieu boréal typique.

Dans son entièreté, cette thèse analyse en profondeur le bilan d'énergie de surface d'une forêt boréale humide à plusieurs échelles spatiales. Les avancées scientifiques sont substantielles de par le type de forêt étudié, la topographie sous-jacente et pour la variation de l'échelle spatiale dans la description des termes du bilan énergétique. Ces résultats seront certainement utiles aux modélisateurs des échanges sol-atmosphère, aux hydrologues travaillant sur des bassins inclus en tout ou en partie dans le milieu boréal, et aux modélisateurs du climat en général.

Bibliographie

Aguilar, C., Herrero, J. & Polo, M. J. (2010) Topographic effects on solar radiation distribution in mountainous watersheds and their influence on reference evapotranspiration estimates at watershed scale. *Hydrol. Earth Syst. Sci*., *14,* 2479-2494. doi :10.5194/hess-14-2479-2010.

Allen, R. G., Tasumi, M., Morse, A., Trezza, R., Wright, J. L., Bastiaanssen, W., Kramber, W., Lorite, I., & Robison, C. W. (2007a). Satellite-based energy balance for mapping evapotranspiration with internalized calibration (METRIC)—Applications. *J. Irrig. Drain. Eng.*, *133*, 395–406. doi:10.1061/(ASCE)0733-9437(2007)133: 4(395).

Allen, R. G., Tasumi, M., & Trezza, R. (2007b). Satellite-based energy balance for mapping evapotranspiration with internalized calibration (METRIC)—Model. *J. Irrig. Drain. Eng.*, *133*, 380–394. doi:10.1061/(ASCE)0733-9437(2007)133: 4(380).

Amiro, B. D., Barr, A. G., Black, T. A., Iwashita, H., Kljun, N., McCaughey, J. H., Morgenstern, K., Murayama, S., Nesic, Z., Orchansky, A. L. & Saigusa, N. (2006) Carbon, energy and water fluxes at mature and disturbed forest sites, Saskatchewan, Canada. *Agric. For. Meteorol*., *136*, 237-251. doi:10.1016/j.agrformet.2004.11.012.

Andreas, E. (1989). Two-wavelength method of measuring path-averaged turbulent surface heat fluxes. *J. Atmos. Ocean. Tech.*, *6*, 280–292.

Asdak, C., Jarvis, P. G., & Gardingen, P. V. (1998). Evaporation of intercepted precipitation based on an energy balance in unlogged and logged forest areas of central Kalimantan, Indonesia. *Agric. For. Meteorol.*, *92*, 173–180. doi:10.1016/S0168-1923(98)00097-5.

Aubin, I., Beaudet, M., & Messier, C. (2000). Light extinction coefficients specific to the understory vegetation of the southern boreal forest, Quebec. *Can. J. For. Res.*, *30*, 168–177. doi:10.1139/x99-185.

Aubinet, M., Chermanne, B., Vandenhaute, M., Longdoz, B., Yernaux, M., & Laitat, E. (2001). Long term carbon dioxide exchange above a mixed forest in the Belgian Ardennes. *Agric. For. Meteorol.*, *108*, 293–315. doi:10.1016/S0168-1923(01) 00244-1.

Aubinet, M., Heinesch, B., & Yernaux, M. (2003). Horizontal and vertical CO_2 advection in a sloping forest. *Boundary-Layer Meteorol.*, *108*, 397–417.

Aubinet, M., Vesala, T., & Papale, D. (2012). *Eddy covariance: a practical guide to measurement and data analysis*. Springer, Dordrecht, Heidelberg, London, New York.

Bailey, W. G., Oke, T. R. & Rouse, W. (1997) *Surface Climates of Canada.* McGill-Queen's University Press, Montréal, Canada.

Balandier, P., Sonohat, G., Sinoquet, H., Varlet-Grancher, C., & Dumas, Y. (2006). Characterisation, prediction and relationships between different wavebands of solar radiation transmitted in the understorey of even-aged oak (Quercus petraea, Q. robur) stands. *Trees*, *20*, 363–370. doi:10.1007/s00468-006-0049-3.

Baldocchi, D. D., Vogel, C. A., & Hall, B. (1997). Seasonal variation of energy and water vapor exchange rates above and below a boreal jack pine forest canopy. *J. Geophys. Res. Atmos.*, *102*, 28939–28951. doi:10.1029/96JD03325.

Baldocchi, D. D., Falge, E., Gu, L., Olson, R., Hollinger, D., Running, S., Anthoni, P., Bernhofer, C., Davis, K., Evans, R., Fuentes, J., Goldstein, A., Katul, G., Law, B., Lee, X., Malhi, Y., Meyers, T., Munger, W., Oechel, W., Paw U, K. T., Pilegaard, K., Schmid, H. P., Valentini, R., Verma, S., Vesala, T., Wilson, K. & Wofsy, S. (2001). FLUXNET: A new tool to study the temporal and spatial variability of ecosystem-scale carbon dioxide, water vapor, and energy flux densities. *Bull. Am. Meteorol. Soc., 82*, 2415-2434. doi:10.1175/1520-0477(2001)082<2415:FANTTS>2.3.CO;2

Barber, V. A., Juday, G. P., & Finney, B. P. (2000). Reduced growth of Alaskan white spruce in the twentieth century from temperature-induced drought stress. *Nature*, *405*, 668. doi:10.1038/35015049.

Barr, A. G., Betts, A. K., Black, T. A., McCaughey, J., & Smith, C. (2001). Intercomparison of BOREAS northern and southern study area surface fluxes in 1994. *J. Geophys. Res. Atmos.*, *106*, 33543–33550. doi:10.1029/2001JD900070.

Barr, A., Morgenstern, K., Black, T. A., McCaughey, J., & Nesic, Z. (2006). Surface energy balance closure by the eddy-covariance method above three boreal forest stands and implications for the measurement of the CO2 flux. *Agric. For. Meteorol.*, *140*, 322–337. doi:10.1016/j.agrformet.2006.08.007.

Barr, A., Griffs, T., Black, T. A., Lee, X., Staebler, R., Fuentes, J., Chen, Z., & Morgenstern, K. (2002). Comparing the carbon budgets of boreal and temperate deciduous forest stands. *Can. J. For. Res., 32*, 813–822. doi:10.1139/x01-131.

Barr, A., Van der Kamp, G., Black, T. A., McCaughey, J., & Nesic, Z. (2012). Energy balance closure at the BERMS flux towers in relation to the water balance of the White Gull Creek watershed 1999–2009. *Agric. For. Meteorol.*, *153*, 3–13. doi:10. 1016/j.agrformet.2011.05.017.

Bellisario, L. M., Boudreau, L. D., Verseghy, D. L., Rouse, W. R., & Blanken, P. D. (2000). Comparing the performance of the Canadian land surface scheme for two subarctic terrain types. *Atmos. Ocean*, *38*, 181–204. doi:10.1080/07055900. 2000.9649645.

Beniston, M. & Rebetez, M. (1996). Regional behavior of minimum temperatures in Switzerland for the period 1979-1993. *Theor. Appl. Climatol*., *53,* 231-244. doi:10.1007/BF00871739.

Berbigier, P., & Bonnefond, J. (1995). Measurement and modelling of radiation transmission within a stand of maritime pine (Pinus pinaster Ait). *Ann. For. Sci.*, *52*, 23–42.

Bergeron, O., Margolis, H. A., Black, T. A., Coursolle, C., Dunn, A. L., Barr, A. G., & Wofsy, S. C. (2007). Comparison of carbon dioxide fluxes over three boreal black spruce forests in Canada. *Glob. Change Biol.*, *13*, 89–107. doi:10.1111/j. 1365-2486.2006.01281.x.

Beyrich, F., De Bruin, H., Meijninger, W., Schipper, J., & Lohse, H. (2002). Results from one-year continuous operation of a large aperture scintillometer over a heterogeneous land surface. *Boundary-Layer Meteorol.*, *105*, 85–97.

Blanken, P., Black, T. A., Neumann, H., Den Hartog, G., Yang, P., Nesic, Z., Staebler, R., Chen, W., & Novak, M. (1998). Turbulent flux measurements above and below the overstory of a boreal aspen forest. *Boundary-Layer Meteorol.*, *89*, 109–140. doi:10.1023/A:1001557022310.

Blanken, P., Black, T. A., Yang, P., Neumann, H., Nesic, Z., Staebler, R., Den Hartog, G., Novak, M., & Lee, X. (1997). Energy balance and canopy conductance of a boreal aspen forest: partitioning overstory and understory components. *J. Geophys. Res. Atmos.*, *102*, 28915–28927. doi:10.1029/97JD00193.

Bosveld, F., van der Vliet, J., & Monna, W. (1999). *The KNMI Garderen experiment: micro-meteorological observations 1988-1989*. Technical Report, KNMI, the Netherlands.

Bourque, C.-A., & Arp, P. (1994). Dawn-to-dusk evolution of air turbulence, temperature and sensible and latent heat fluxes above a forest canopy: Concepts, model and field comparisons. *Atmos. Ocean*, *32*, 299–334. doi:10.1080/07055900.1994. 9649500.

Braam, M., Bosveld, F. C., & Moene, A. F. (2012). On Monin-Obukhov scaling in and above the atmospheric surface layer: the complexities of elevated scintillometer measurements. *Boundary-Layer Meteorol.*, *144*, 157–177. doi:10.1007/ s10546-012-9716-7.

Brandt, J. P. (2009). The extent of the North American boreal zone. *Environ. Rev.*, *17,* 101-161. doi:10.1139/A09-004

Brandt, J., Flannigan, M., Maynard, D., Thompson, I., & Volney, W. (2013). An introduction to Canada's boreal zone: ecosystem processes, health, sustainability, and environmental issues. *Environ. Rev.*, *21*, 207–226. doi:10.1139/er-2013-0040.

Bréda, N. J. (2003). Ground-based measurements of leaf area index: a review of methods, instruments and current controversies. *J. Exp. Bot.*, *54*, 2403–2417. doi:10.1093/jxb/erg263.

Breshears, D. D., Nyhan, J. W., Heil, C. E., & Wilcox, B. P. (1998). Effects of woody plants on microclimate in a semiarid woodland: soil temperature and evaporation in canopy and intercanopy patches. *Int. J. Plant Sci.*, *159*, 1010–1017. doi:10.1086/ 314083.

Brown, S., Petrone, R., Chasmer, L., Mendoza, C., Lazerjan, M., Landhäusser, S., Silins, U., Leach, J., & Devito, K. (2014). Atmospheric and soil moisture controls on evapotranspiration from above and within a Western Boreal Plain aspen forest. *Hydrol. Process., 28*, 4449–4462. doi:10.1002/hyp.9879.

Brümmer, C., Black, T. A., Jassal, R. S., Grant, N. J., Spittlehouse, D. L., Chen, B., Nesic, Z., Amiro, B. D., Arain, M. A., & Barr, A. G. (2012). How climate and vegetation type influence evapotranspiration and water use efficiency in Canadian forest, peatland and grassland ecosystems. *Agric. For. Meteorol.*, *153*, 14–30. doi:10.1016/j.agrformet.2011.04.008.

Brutsaert, W. (1982). *Evaporation into the Atmosphere: Theory, History, and Applications*. Reidel, Dordrecht, the Netherlands.

Brutsaert, W. (2005). *Hydrology: an Introduction*. Cambridge University Press, Cambridge, USA.

Budyko, M. (1958). *The heat balance of the earth's surface*. Springer, Washington, DC, USA.

Budyko, M. I. (1974). *Climate and life*. Academic, New York, USA.

Burba, G. (2013). *Eddy Covariance Method for Scientific, Industrial, Agricultural and Regulatory Applications: A Field Book on Measuring Ecosystem Gas Exchange and Areal Emission Rates.* LI-COR Biosciences, Lincoln, Nebraska, USA.

Burba, G. (2019). Email correspondence on the Fluxnet mailing list, February 18-21 2019.

Cheng, Y., Parlange, M. B., & Brutsaert, W. (2005). Pathology of Monin-Obukhov similarity in the stable boundary layer. *J. Geophys. Res. Atmos.*, *110*. doi:10.1029/ 2004JD004923.

Christen, A., Van Gorsel, E., Vogt, R., Andretta, M. & Rotach, M. W. (2001). Ultrasonic anemometer instrumentation at steep slopes wind tunnel study-field intercomparison-measurements. *MAP Newsletter*, *15*, 164-167.

Comer, N. T., Lafleur, P. M., Roulet, N. T., Letts, M. G., Skarupa, M., & Verseghy, D. (2000). A test of the Canadian Land Surface Scheme (CLASS) for a variety of wetland types. *Atmos. Ocean*, *38*, 161–179. doi:10.1080/07055900.2000.9649644.

Coursolle, C., Margolis, H. A., Barr, A. G., Black, T. A., Amiro, B. D., Mc-Caughey, J. H., Flanagan, L. B., Lafleur, P. M., Roulet, N. T., Bourque, C. P.-A. et al. (2006). Late-summer carbon fluxes from Canadian forests and peatlands along an east west continental transect. *Can. J. For. Res., 36*, 783–800. doi:10.1139/x05-270.

Crawford, B., Grimmond, C. S. B., Ward, H. C., Morrison, W., & Kotthaus, S. (2017). Spatial and temporal patterns of surface-atmosphere energy exchange in a dense urban environment using scintillometry. *Q. J. Roy. Meteorol. Soc.*, *143*, 817–833. doi:10.1002/qj.2967.

Daly, C., Neilson, R. P. & Phillips, D. L. (1994). A statistical-topographic model for mapping climatological precipitation over mountainous terrain. *J. Appl. Meteorol*., *33,* 140-158. doi:10.1175/1520-0450(1994)033<0140:ASTMFM>2.0.CO;2.

Dee, D. P., Uppala, S. M., Simmons, A., Berrisford, P., Poli, P., Kobayashi, S., Andrae, U., Balmaseda, M., Balsamo, G., Bauer, d. P. et al. (2011). The ERA-Interim reanalysis: Configuration and performance of the data assimilation system. *Q. J. Roy. Meteorol. Soc.*, *137*, 553–597. doi:10.1002/qj.828.

Donohue, R. J., McVicar, T. R., & Roderick, M. L. (2010). Assessing the ability of potential evaporation formulations to capture the dynamics in evaporative demand within a changing climate. *J. Hydrol.*, *386*, 186–197. doi:10.1016/j.jhydrol. 2010.03.020.

D'Orangeville, L., Duchesne, L., Houle, D., Kneeshaw, D., Côté, B., & Pederson, N. (2016). Northeastern North America as a potential refugium for boreal forests in a warming climate. *Science*, *352*, 1452–1455. doi:10.1126/science.aaf4951.

El Maayar, M., & Chen, J. M. (2006). Spatial scaling of evapotranspiration as affected by heterogeneities in vegetation, topography, and soil texture. *Remote Sens. Environ.*, *102*, 33-51. doi:10.1016/j.rse.2006.01.017.

Ellis, C. R., & Pomeroy, J. W. (2007). Estimating sub-canopy shortwave irradiance to melting snow on forested slopes. *Hydrol. Process.*, *21*, 2581–2593. doi:10.1002/ hyp.6794.

Essery, R. (2003a). Aggregated and distributed modelling of snow cover for a high-latitude basin. *Global Planet. Change*., *38,* 115-120. doi:10.1016/S0921-8181(03)00013-4.

Essery, R., Pomeroy, J., Parviainen, J., & Storck, P. (2003b). Sublimation of snow from coniferous forests in a climate model. *J. Climate*, *16*, 1855–1864. doi:10.1175/ 1520-0442(2003)016<1855:SOSFCF>2.0.CO;2.

Evans, J. G. (2009). *Long-path scintillometry over complex terrain to determine areal-averaged sensible and latent heat fluxes*. Ph.D. thesis, University of Reading, Reading, United Kingdom.

Evans, J. G., & DeBruin, H. A. R. (2011). The effective height of a two-wavelength scintillometer system. *Boundary-Layer Meteorol.*, *141*, 165–177.

Evans, J. G., McNeil, D. D., Finch, J. W., Murray, T., Harding, R. J., Ward, H. C., & Verhoef, A. (2012). Determination of turbulent heat fluxes using a large aperture scintillometer over undulating mixed agricultural terrain. *Agric. For. Meteorol.*, *166167*, 221–233.

Ezzahar, J., & Chehbouni, A. (2009). The use of scintillometry for validating aggregation schemes over heterogeneous grids. *Agric. For. Meteorol.*, *149*, 2098–2109. doi:10.1016/j.agrformet.2009.09.004.

Ezzahar, J., Chehbouni, A., Er-Raki, S., & Hanich, L. (2009a). Combining a large aperture scintillometer and estimates of available energy to derive evapotranspiration over several agricultural fields in a semi-arid region. *Plant Biosystems.*, (pp. 209– 221). doi:10.1080/11263500802710036.

Ezzahar, J., Chehbouni, A., Hoedjes, J., Ramier, D., Boulain, N., Boubkraoui, S., Cappelaere, B., Descroix, L., Mougenot, B., & Timouk, F. (2009b). Combining scintillometer measurements and an aggregation scheme to estimate area-averaged latent heat flux during the AMMA experiment. *J. Hydrol.*, *375*, 217–226. doi:10.1016/j.jhydrol.2009.01.010.

Faith, D. P., Minchin, P. R., Belbin, L. (1987). Compositional dissimilarity as a robust measure of ecological distance. *Vegetatio, 69*, 57–68, doi:10.1007/BF00038687

Finkelstein, P. L., & Sims, P. F. (2001). Sampling error in eddy correlation flux measurements. *J. Geophys. Res.*, *106*, 3503–3509. doi:10.1029/2000JD900731.

FLUXNET–Canada (2016). *FLUXNET Canada Research Network - Canadian Carbon Program Data Collection, 1993-2014*. ORNL DAAC, Oak Ridge, Tennessee, USA. doi:10.3334/ORNLDAAC/1335.

Foken, T. (2008). The energy balance closure problem: An overview. *Ecol. Appl.*, *18*, 1351–1367. doi:10.1890/06-0922.1.

Foken, T., Mauder, M., Liebethal, C., Wimmer, F., Beyrich, F., Leps, J.-P., Raasch, S., DeBruin, H. A. R., Meijninger, W. M. L., & Bange, J. (2010). Energy balance closure for the LITFASS-2003 experiment. *Theor. Appl. Climatol.*, *101*, 149–160.

Ford, T. W., & Quiring, S. M. (2013). Influence of MODIS-derived dynamic vegetation on VIC-simulated soil moisture in Oklahoma. *J. Hydrometeorol.*, *14*, 1910–1921. doi:10.1175/JHM-D-13-037.1.

Fritschen, L. & Qian, P. (1990). Net radiation, sensible and latent heat flux densities on slopes computed by the energy balance method. *Boundary-Layer Meteorol.*, *53,* 163-171. doi:10.1007/BF00122468.

Gao, Y., Markkanen, T., Aurela, M., Mammarella, I., Thum, T., Tsuruta, A., Yang, H., Aalto, T. et al. (2017). Response of water use efficiency to summer drought in a boreal Scots pine forest in Finland. *Biogeosciences, 14*, 4409–4422. doi:10.5194/bg-14-4409-2017.

Garai, A., Kleissl, J., & Smith, S. G. L. (2010). Estimation of biomass heat storage using thermal infrared imagery: application to a walnut orchard. *Boundary-Layer Meteorol.*, *137*, 333–342. doi:10.1007/s10546-010-9524-x.

Gauthier, S., Bernier, P., Kuuluvainen, T., Shvidenko, A., & Schepaschenko, D. (2015). Boreal forest health and global change. *Science*, *349*, 819–822. doi:10.1126/ science.aaa9092.

Geissbühler, P., Siegwolf, R., & Eugster, W. (2000). Eddy covariance measurements on mountain slopes: the advantage of surface-normal sensor orientation over a vertical set-up. *Boundary-Layer Meteorol.*, *96*, 371–392. doi:10.1023/A:1002660521017.

Gelfan, A., Pomeroy, J., & Kuchment, L. (2004). Modeling forest cover influences on snow accumulation, sublimation, and melt. *J. Hydrometeorol.*, *5*, 785–803. doi:10.1175/1525-7541(2004)005<0785:MFCIOS>2.0.CO;2.

Geli, H. M., Neale, C. M., Watts, D., Osterberg, J., De Bruin, H. A., Kohsiek, W., Pack, R. T., & Hipps, L. E. (2012). Scintillometer-based estimates of sensible heat flux using lidar-derived surface roughness. *J. Hydrometeorol.*, *13*, 1317–1331. doi:10.1175/JHM-D-11-085.1.

Gentine, P., D'Odorico, P., Lintner, B. R., Sivandran, G., & Salvucci, G. (2012). Interdependence of climate, soil, and vegetation as constrained by the Budyko curve. *Geophys. Res. Lett.*, *39*. doi:10.1029/2012GL053492.

Giasson, M.-A., Coursolle, C., & Margolis, H. A. (2006). Ecosystem-level CO_2 fluxes from a boreal cutover in eastern Canada before and after scarification. *Agric. For. Meteorol.*, *140*, 23–40. doi:10.1016/j.agrformet.2006.08.001.

Gigante, V., Iacobellis, V., Manfreda, S., Milella, P., & Portoghese, I. (2009). Influences of Leaf Area Index estimations on water balance modeling in a Mediterranean semi-arid basin. *Nat. Haz. Earth Syst. Sci.*, *9*, 979–991. doi:10.5194/ nhess-9-979-2009.

Giorgi, F., Hurrell, J. W., Marinucci, M. R. & Beniston, M. (1997). Elevation dependency of the surface climate change signal: a model study. *J. Climate, 10,* 288-296. doi:10.1175/1520-0442(1997)010<0288:EDOTSC>2.0.CO;2.

Goudriaan, J. (1988). The bare bones of leaf-angle distribution in radiation models for canopy photosynthesis and energy exchange. *Agric. For. Meteorol.*, *43*, 155–169.

Goulden, M., Anderson, R., Bales, R., Kelly, A., Meadows, M., & Winston, G. (2012). Evapotranspiration along an elevation gradient in California's Sierra Nevada. *J. Geophys. Res. Biogeosci.*, *117*. doi:10.1029/2012JG002027.

Gouttevin, I., Lehning, M., Jonas, T., Gustafsson, D., & Mölder, M. (2015). A two-layer canopy model with thermal inertia for an improved snowpack energy balance below needleleaf forest (model SNOWPACK, version 3.2. 1, revision 741). *Geosci. Model Dev.*, *8*, 2379. doi:10.5194/gmd-8-2379-2015.

Gower, S. T., Kucharik, C. J., & Norman, J. M. (1999). Direct and indirect estimation of leaf area index, fAPAR, and net primary production of terrestrial ecosystems. *Remote Sens. Environ.*, *70*, 29–51. doi:10.1016/S0034-4257(99)00056-5.

Grant, R F. (2004). Modelling topographic effects on net ecosystem productivity of boreal black spruce forest. *Tree Physiol*., *24*, 1-18. doi:10.1093/treephys/24.1.1.

Guyot, A., Cohard, J.-M., Anquetin, S., & Galle, S. (2012). Long-term observations of turbulent fluxes over heterogeneous vegetation using scintillometry and additional observations: A contribution to AMMA under Sudano-Sahelian climate. *Agric. For. Meteorol.*, *154*, 84–98. doi:10.1016/j.agrformet.2011.10.008.

Haddeland, I., Matheussen, B. V. & Lettenmaier, D. P. (2002). Influence of spatial resolution in a macroscale hydrologic model. *Water Resour. Res., 38*, 1124-1133. doi:10.1029/2001WR000854.

Hammerle, A., Haslwanter, A., Schmitt, M., Bahn, M., Tappeiner, U., Cernusca, A., & Wohlfahrt, G. (2007). Eddy covariance measurements of carbon dioxide, latent and sensible energy fluxes above a meadow on a mountain slope. *Boundary-Layer Meteorol.*, *122*, 397–416. doi:10.1007/s10546-006-9109-x.

Hardy, J., Melloh, R., Koenig, G., Marks, D., Winstral, A., Pomeroy, J., & Link, T. (2004). Solar radiation transmission through conifer canopies. *Agric. For. Meteorol.*, *126*, 257–270. doi:10.1016/j.agrformet.2004.06.012.

Hartogensis, O., Watts, C., Rodriguez, J., & De Bruin, H. (2003). Derivation of an effective height for scintillometers: La Poza experiment in Northwest Mexico. *J. Hydrometeorol.*, *4*, 915–928. doi:10.1175/1525-7541(2003)004<0915: DOAEHF>2.0.CO;2.

Hedstrom, N., & Pomeroy, J. (1998). Measurements and modelling of snow interception in the boreal forest. *Hydrol. Process.*, *12*, 1611–1625. doi:10.1002/(SICI)1099-1085(199808/09)12:10/11<1611::AID-HYP684>3.0.CO;2-4.

Hill, R. J., Bohlander, R. A., Clifford, S. F., McMillan, R. W., Priestly, J., & Schoenfeld, W. (1988). Turbulence-induced millimeter-wave scintillation compared with micrometeorological measurements. *IEEE T. Geosci. Remote Sci.*, *26*, 330–342. doi:10.1109/36.3035.

Hiller, R., Zeeman, M. J., & Eugster, W. (2008). Eddy-covariance flux measurements in the complex terrain of an alpine valley in Switzerland. *Boundary-Layer Meteorol.*, *127*, 449–467. doi:10.1007/s10546-008-9267-0.

Hoerling, M. P., Eischeid, J. K., Quan, X. W., Diaz, H. F., Webb, R. S., Dole, R. M. & Easterling, D. R. (2012). Is a transition to semipermanent drought conditions imminent in the US Great Plains? *J. Climate., 25*, 8380-8386. doi:10.1175/JCLI-D-12-00449.1.

Holst, T., Rost, J., & Mayer, H. (2005). Net radiation balance for two forested slopes on opposite sides of a valley. *Int. J. Biometeorol.*, *49*, 275–284. doi:10.1007/ s00484-004-0251-1.

Huber, A., & Iroumé, A. (2001). Variability of annual rainfall partitioning for different sites and forest covers in Chile. *J. Hydrol.*, *248*, 78–92. doi:10.1016/ S0022-1694(01)00394-8.

Ikawa, H., Nakai, T., Busey, R. C., Kim, Y., Kobayashi, H., Nagai, S., Ueyama, M., Saito, K., Nagano, H., Suzuki, R. et al. (2015). Understory CO_2, sensible heat, and latent heat fluxes in a black spruce forest in interior Alaska. *Agric. For. Meteorol.*, *214*, 80–90. doi:10.1016/j.agrformet.2015.08.247.

Ilvesniemi, H., Pumpanen, J., Duursma, R., Hari, P., Keronen, P., Kolari, P., Kulmala, M., Mammarella, I., Nikinmaa, E., Rannik, Ü. et al. (2010). Water balance of a boreal Scots pine forest. *Boreal Environ. Res.*, *15*, 375–396.

IPCC (2013). Contribution of working group I to the fifth assessment report of the intergovernmental panel on climate change. In *Climate Change 2013: The Physical Science Basis*. Cambridge University Press, Cambridge, USA.

Isabelle, P.-E., Nadeau, D. F., Asselin, M.-H., Harvey, R., Musselman, K. N., Rousseau, A. N., & Anctil, F. (2018a). Solar radiation transmittance of a boreal balsam fir canopy: Spatiotemporal variability and impacts on growing season hydrology. *Agric. For. Meteorol.*, *263*, 1–14. doi:10.1016/j.agrformet.2018.07.022.

Isabelle, P.-E., Nadeau, D. F., Rousseau, A. N., & Anctil, F. (2018b). Water budget, performance of evapotranspiration formulations, and their impact on hydrological modeling of a small boreal peatland-dominated watershed. *Can. J. Earth Sci.*, *55*, 206–220. doi:10.1139/cjes-2017-0046.

Itier, B. & Brunet, Y. (1996). Recent developments and present trends in evaporation research: A partial survey. In *Evapotranspiration and irrigation scheduling: Proceedings of the International Conference ASAE*, Camp C, Sadler E & Yoder R, Eds., pp. 1-20.

Jacobs, C., Elbers, J., Brolsma, R., Hartogensis, O., Moors, E., Márquez, M. T. R.-C., & van Hove, B. (2015). Assessment of evaporative water loss from Dutch cities. *Build. Environ.*, *83*, 27–38. doi:10.1016/j.buildenv.2014.07.005.

Jarvis, P., Massheder, J., Hale, S., Moncrieff, J., Rayment, M., & Scott, S. (1997). Seasonal variation of carbon dioxide, water vapor, and energy exchanges of a boreal black spruce forest. *J. Geophys. Res. Atmos.*, *102*, 28953–28966. doi:10.1029/ 97JD01176.

Joiner, D. W., McCaughey, J. H., Lafleur, P. M. & Bartlett, P. A. (1999). Water and carbon dioxide exchange at a boreal young jack pine forest in the BOREAS northern study area. *J. Geophys. Res. Atmos*., *104*, 27641-27652. doi:10.1029/1999JD900368.

Jonckheere, I., Fleck, S., Nackaerts, K., Muys, B., Coppin, P., Weiss, M., & Baret, F. (2004). Review of methods for in situ leaf area index determination: Part I. Theories, sensors and hemispherical photography. *Agric. For. Meteorol.*, *121*, 19–35. doi:10.1016/j.agrformet.2003.08.027.

Kang, S., Lee, D. & Kimball, J. S. (2004). The effects of spatial aggregation of complex topography on hydroecological process simulations within a rugged forest landscape: Development and application of a satellite-based topoclimatic model. *Can. J. For. Res*., *34*, 519-530. doi:10.1139/x03-213.

Katul, G. G., & Parlange, M. B. (1992). A Penman-Brutsaert model for wet surface evaporation. *Water Resour. Res.*, *28*, 121–126. doi:10.1029/91WR02324.

Kauppi, P. E., Posch, M., & Pirinen, P. (2014). Large impacts of climatic warming on growth of boreal forests since 1960. *PLoS One*, *9*, e111340. doi:10.1371/ journal.pone.0111340.

Kelliher, F. M., Lloyd, J., Arneth, A., Byers, J. N., McSeveny, T. M., Milukova, I., Grigoriev, S., Panfyorov, M., Sogatchev, A., Varlargin, A., Ziegler, W., Bauer, G. & Schulze, E. D. (1998). Evaporation from a central Siberian pine forest. *J. Hydrol*., *205*, 279-296. doi:10.1016/S0022-1694(98)00082-1.

Kellomaki, S., & Wang, K.-Y. (1999). Short-term environmental controls of heat and¨ water vapour fluxes above a boreal coniferous forest: model computations compared with measurements by eddy correlation. *Ecol. Model.*, *124*, 145–173. doi:10.1016/ S0304-3800(99)00159-3.

Klaassen, W., Bosveld, F., & De Water, E. (1998). Water storage and evaporation as constituents of rainfall interception. *J. Hydrol.*, *212*, 36–50. doi:10.1016/ S0022-1694(98)00200-5.

Kleissl, J., Hartogensis, O., & Gomez, J. (2010). Test of scintillometer saturation correction methods using field experimental data. *Boundary-Layer Meteorol.*, *137*, 493–507. doi:10.1007/s10546-010-9540-x.

Kleissl, J., Hong, S.-H., & Hendrickx, J. M. (2009). New Mexico scintillometer network: supporting remote sensing and hydrologic and meteorological models. *Bull. Amer. Meteorol. Soc.*, *90*, 207–218. doi:10.1175/2008BAMS2480.1.

Kljun, N., Calanca, P., Rotach, M., & Schmid, H. P. (2015). A simple two-dimensional parameterisation for Flux Footprint Prediction (FFP). *Geosci. Model Dev.*, *8*, 3695– 3713. doi:10.5194/gmd-8-3695-2015.

Kneeshaw, D. D., & Bergeron, Y. (1998). Canopy gap characteristics and tree replacement in the southeastern boreal forest. *Ecology*, *79*, 783–794. doi:10.1890/ 0012-9658(1998)079[0783:CGCATR]2.0.CO;2.

Kochendorfer, J., Rasmussen, R., Wolff, M., Baker, B., Hall, M. E., Meyers, T., Landolt, S., Jachcik, A., Isaksen, K., Brækkan, R. et al. (2017). The quantification and correction of wind-induced precipitation measurement errors. *Hydrol. Earth Syst. Sci.*, *21*, 1973–1989. doi:10.5194/hess-21-1973-2017.

Koivusalo, H., & Kokkonen, T. (2002). Snow processes in a forest clearing and in a coniferous forest. *J. Hydrol.*, *262*, 145–164. doi:10.1016/S0022-1694(02) 00031-8.

Kooijmans, L. M., & Hartogensis, O. K. (2016). Surface-layer similarity functions for dissipation rate and structure parameters of temperature and humidity based on eleven field experiments. *Boundary-Layer Meteorol.*, *160*, 501–527. doi:10.1007/ s10546-016-0152-y.

Kothavala, Z., Arain, M. A., Black, T. A., & Verseghy, D. (2005). The simulation of energy, water vapor and carbon dioxide fluxes over common crops by the Canadian Land Surface Scheme (CLASS). *Agric. For. Meteorol.*, *133*, 89–108. doi:10.1016/j.agrformet.2005.08.007.

Kurbatova, J., Li, C., Varlagin, A., Xiao, X., & Vygodskaya, N. (2008). Modeling carbon dynamics in two adjacent spruce forests with different soil conditions in Russia. *Biogeosciences*, *5*, 969–980. doi:10.5194/bg-5-969-2008.

Landsberg, J. J., & Gower, S. T. (1997). *Applications of physiological ecology to forest management*. Academic Press, New York.

Lavigne, M.-P. (2007). *Modélisation du régime hydrologique et de l'impact des coupes forestières sur l'écoulement du ruisseau des Eaux-Volées à l'aide d'HYDROTEL*. Master's thesis, Institut national de la recherche scientifique - Centre Eau Terre Environnement, Québec, Canada.

Lawler, R. R., & Link, T. E. (2011). Quantification of incoming all-wave radiation in discontinuous forest canopies with application to snowmelt prediction. *Hydrol. Process.*, *25*, 3322–3331. doi:10.1002/hyp.8150.

Leroyer, S., Bélair, S., Mailhot, J. & Strachan, I. B. (2011). Microscale numerical prediction over Montreal with the Canadian external urban modeling system. *J. Appl. Meteorol. Clim.*, *50*, 2410-2428. doi:10.1175/JAMC-D-11-013.1.

Leuning, R., Van Gorsel, E., Massman, W. J., & Isaac, P. R. (2012). Reflections on the surface energy imbalance problem. *Agric. For. Meteorol.*, *156*, 65–74. doi:10.1016/j.agrformet.2011.12.002.

Li, X., Gao, Z., Li, Y., & Tong, B. (2017). Comparison of sensible heat fluxes measured by a large aperture scintillometer and eddy covariance system over a heterogeneous farmland in East China. *Atmosphere*, *8*, 101. doi:10.3390/atmos8060101.

Li, X., Strahler, A. H., Woodcock, C. E. et al. (1995). A hybrid geometric optical-radiative transfer approach for modeling albedo and directional reflectance of discontinuous canopies. *IEEE T. Geosci. Remote Sens.*, *33*, 466–480.

Liu, P., Black, T. A., Jassal, R. S., Zha, T., Nesic, Z., Barr, A. G., Helgason, W. D., Jia, X., Tian, Y., Stephens, J. J. et al. (2019). Divergent long-term trends and interannual variation in ecosystem resource use efficiencies of a southern boreal old black spruce forest 1999–2017. *Glob. Change Biol.* doi:10.1111/gcb.14674.

Lloyd, A. H., & Bunn, A. G. (2007). Responses of the circumpolar boreal forest to 20th century climate variability. *Environ. Res. Lett.*, *2*, 045013. doi:10.1088/ 1748-9326/2/4/045013.

Lofgren, B. M., Hunter, T. S. & Wilbarger, J. (2011). Effects of using air temperature as a proxy for potential evapotranspiration in climate change scenarios of Great Lakes basin hydrology. *J. Great Lakes Res., 37*, 744-752. doi:10.1016/j.jglr.2011.09.006.

Lüdi, A., Beyrich, F., & Mätzler, C. (2005). Determination of the turbulent temperature–humidity correlation from scintillometric measurements. *Boundary-Layer Meteorol.*, *117*, 525–550.

Lundberg, A., Eriksson, M., Halldin, S., Kellner, E., & Seibert, J. (1997). New approach to the measurement of interception evaporation. *J. Atmos. Ocean. Tech.*, *14*, 1023–1035. doi:10.1175/1520-0426(1997)014<1023:NATTMO>2.0.CO;2.

Lundberg, A., & Halldin, S. (2001). Snow interception evaporation. Review of measurement techniques, processes, and models. *Theor. Appl. Climatol.*, *70*, 117–133. doi:10.1007/s007040170010.

Lundberg, A., & Koivusalo, H. (2003). Estimating winter evaporation in boreal forests with operational snow course data. *Hydrol. Process.*, *17*, 1479–1493. doi:10.1002/ hyp.1179.

Mahrt, L. (1998). Flux sampling errors for aircraft and towers. *J. Atmos. Ocean. Tech., 15*, 416-429. doi:10.1175/1520-0426(1998)015<0416:FSEFAA>2.0.CO;2.

Mahrt, L. (2010). Computing turbulent fluxes near the surface: Needed improvements. *Agric. For. Meteorol., 150*, 501-509. doi:10.1016/j.agrformet.2010.01.015.

Matzinger, N., Andretta, M., Van Gorsel, E., Vogt, R., Ohmura, A., & Rotach, M. (2003). Surface radiation budget in an alpine valley. *Q. J. Roy. Meteorol. Soc.*, *129*, 877–895. doi:10.1256/qj.02.44.

Mauder, M., & Foken, T. (2011). Documentation and instruction manual of the eddy-covariance software package TK3. Technical Report, Universität Bayreuth, Bayreuth, Germany.

Mauder, M., Genzel, S., Fu, J., Kiese, R., Soltani, M., Steinbrecher, R., Zeeman, M., Banerjee, T., De Roo, F., & Kunstmann, H. (2018). Evaluation of energy balance closure adjustment methods by independent evapotranspiration estimates from lysimeters and hydrological simulations. *Hydrol. Process.*, *32*, 39–50. doi:10.1002/hyp.11397.

McCaughey, J. H. (1978a). Estimation of net radiation for a coniferous forest, and the effects of logging on net radiation and the reflection coefficient. *Can. J. For. Res.*, *8*, 450-455. doi:10.1139/x78-066.

McCaughey, J. H. (1978b). Energy balance and evapotranspiration estimates for a mature coniferous forest. *Can. J. For. Res.*, *8*, 456–462. doi:10.1139/x78-067.

McCaughey, J., Pejam, M., Arain, M., & Cameron, D. (2006). Carbon dioxide and energy fluxes from a boreal mixedwood forest ecosystem in Ontario, Canada. *Agric. For. Meteorol.*, *140*, 79–96. doi:10.1016/j.agrformet.2006.08.010.

McVicar, T. R., Van Niel, T. G., Li, L., Hutchinson, M. F., Mu, X. & Liu, Z. (2007). Spatially distributing monthly reference evapotranspiration and pan evaporation considering topographic influences. *J. Hydrol*., *338*, 196-220. doi:10.1016/j.jhydrol.2007.02.018.

Meijninger, W., Beyrich, F., Lüdi, A., Kohsiek, W., & Bruin, H. D. (2006). Scintillometer-based turbulent fluxes of sensible and latent heat over a heterogeneous land surface–a contribution to LITFASS-2003. *Boundary-Layer Meteorol.*, *121*, 89–110.

Meijninger, W., Green, A., Hartogensis, O., Kohsiek, W., Hoedjes, J., Zuurbier, R., & De Bruin, H. (2002a). Determination of area-averaged water vapour fluxes with large aperture and radio wave scintillometers over a heterogeneous surface – Flevoland field experiment. *Boundary-Layer Meteorol.*, *105*, 63–83.

Meijninger, W., Hartogensis, O., Kohsiek, W., Hoedjes, J., Zuurbier, R., & De Bruin, H. (2002b). Determination of area-averaged sensible heat fluxes with a large aperture scintillometer over a heterogeneous surface – Flevoland field experiment. *Boundary-Layer Meteorol.*, *105*, 37–62.

MELCC (2019). *Données du programme de surveillance du climat*. Direction générale de la surveillance du climat, Ministère de l'Environnement et de la Lutte contre les Changements Climatiques, Québec, Canada.

Min, W., Chen, Z., Sun, L., Gao, W., Luo, X., Yang, T., Pu, J., Huang, G., & Yang, X. (2004). A scheme for pixel-scale aerodynamic surface temperature over hilly land. *Adv. Atmos. Sci.*, *21*, 125–131. doi:10.1007/BF02915686.

Mkhabela, M., Amiro, B., Barr, A., Black, T. A., Hawthorne, I., Kidston, J., McCaughey, J., Orchansky, A., Nesic, Z., Sass, A., Shashkov, A., & Zhab, T. (2009). Comparison of carbon dynamics and water use efficiency following fire and harvesting in Canadian boreal forests. *Agric. For. Meteorol.*, *149*, 783–794. doi:10.1016/j. agrformet.2008.10.025.

Moene, A. F., & Schüttemeyer, D. (2008). The effect of surface heterogeneity on the temperature-humidity correlation and the relative transport efficiency. *Boundary-Layer Meteorol.*, *129*, 99–113. doi:10.1007/s10546-008-9312-z.

Moffat, A. M., Papale, D., Reichstein, M., Hollinger, D. Y., Richardson, A. D., Barr, A. G., Beckstein, C., Braswell, B. H., Churkina, G., & Desai, A. R. (2007). Comprehensive comparison of gap-filling techniques for eddy covariance net carbon fluxes. *Agric. For. Meteorol.*, *147*, 209–232.

Molotch, N. P., Blanken, P. D., Williams, M. W., Turnipseed, A. A., Monson, R. K., & Margulis, S. A. (2007). Estimating sublimation of intercepted and sub-canopy snow using eddy covariance systems. *Hydrol. Process.*, *21*, 1567–1575. doi:10.1002/ hyp.6719.

Moncrieff, J., Clement, R., Finnigan, J., & Meyers, T. (2004). Averaging, detrending, and filtering of eddy covariance time series. In X. Lee, W. Massman, & B. Law (Eds.), *Handbook of micrometeorology: a guide for surface flux measurement and analysis* (pp. 7–31). Springer, Dordrecht, The Netherlands.

Moncrieff, J. B., Massheder, J., De Bruin, H., Elbers, J., Friborg, T., Heusinkveld, B., Kabat, P., Scott, S., Søgaard, H., & Verhoef, A. (1997). A system to measure surface fluxes of momentum, sensible heat, water vapour and carbon dioxide. *J. Hydrol.*, *188*, 589–611.

Monin, A. S., & Yaglom, A. M. (1971). *Statistical fluid mechanics* volume I. MIT Press, Cambridge, USA.

Monsi, M., & Saeki, T. (1953). Uber den Lichtfaktor in den Pflanzengesellschaften und seine Bedeutung fur die Stoffproduktion. *Jpn. J. Bot*, *14*, 22–52.

Montaldo, N., Rondena, R., Albertson, J. D., & Mancini, M. (2005). Parsimonious modeling of vegetation dynamics for ecohydrologic studies of water-limited ecosystems. *Water Resour. Res.*, *41*. doi:10.1029/2005WR004094.

Montesi, J., Elder, K., Schmidt, R., & Davis, R. E. (2004). Sublimation of intercepted snow within a subalpine forest canopy at two elevations. *J. Hydrometeorol.*, *5*, 763–773. doi:10.1175/1525-7541(2004)005<0763:SOISWA>2.0.CO;2.

Montgomery, R., & Chazdon, R. (2002). Light gradient partitioning by tropical tree seedlings in the absence of canopy gaps. *Oecologia*, *131*, 165–174. doi:10.1007/ s00442-002-0872-1.

Morais, A., Fortin, V., & Anctil, F. (2015). Modelling of seasonal evapotranspiration from an agricultural field using the Canadian Land Surface Scheme (CLASS) with a pedotransfer rule and multicriteria optimization. *Atmos. Ocean*, *53*, 161–175. doi:10.1080/07055900.2014.999745.

Mottus, M., & Sulev, M. (2006). Radiation fluxes and canopy transmittance: Models and measurements inside a willow canopy. *J. Geophys. Res. Atmos.*, *111*. doi:10. 1029/2005JD005932.

Musselman, K. N., Margulis, S. A., & Molotch, N. P. (2013). Estimation of solar direct beam transmittance of conifer canopies from airborne LiDAR. *Remote Sens. Environ.*, *136*, 402–415. doi:10.1016/j.rse.2013.05.021.

Musselman, K. N., Molotch, N. P., Margulis, S. A., Kirchner, P. B., & Bales, R. C. (2012a). Influence of canopy structure and direct beam solar irradiance on snowmelt rates in a mixed conifer forest. *Agric. For. Meteorol.*, *161*, 46–56. doi:10.1016/j.agrformet.2012.03.011.

Musselman, K. N., Molotch, N. P., Margulis, S. A., Lehning, M., & Gustafsson, D. (2012b). Improved snowmelt simulations with a canopy model forced with photoderived direct beam canopy transmissivity. *Water Resour. Res.*, *48*. doi:10.1029/2012WR012285.

Musselman, K. N., Pomeroy, J. W., & Link, T. E. (2015). Variability in shortwave irradiance caused by forest gaps: Measurements, modelling, and implications for snow energetics. *Agric. For. Meteorol.*, *207*, 69–82. doi:10.1016/j.agrformet. 2015.03.014.

Myneni, R., Knyazikhin, Y., & Park, T. (2015). *MCD15A2H MODIS/Terra+Aqua leaf area index/FPAR 8-day L4 Global 500 m SIN Grid V006*. Technical Report, NASA EOSDIS Land Processes DAAC, USA.

Nadeau, D. F., Pardyjak, E. R., Higgins, C. W., Huwald, H., & Parlange, M. B. (2013a). Flow during the evening transition over steep alpine slopes. *Q. J. R. Meteorol. Soc.*, *139*, 607–624. doi:10.1002/qj.1985.

Nadeau, D. F., Pardyjak, E. R., Higgins, C. W., & Parlange, M. B. (2013b). Similarity scaling over a steep alpine slope. *Boundary-Layer Meteorol.*, *147*, 401–419. doi:10. 1007/s10546-012-9787-5.

Ni, W., Li, X., Woodcock, C. E., Roujean, J.-L., & Davis, R. E. (1997). Transmission of solar radiation in boreal conifer forests: Measurements and models. *J. Geophys. Res. Atmos.*, *102*, 29555–29566. doi:10.1029/97JD00198.

Nijssen, B., & Lettenmaier, D. P. (1999). A simplified approach for predicting shortwave radiation transfer through boreal forest canopies. *J. Geophys. Res.*, *104*, 27859–27868. doi:10.1029/1999JD900377.

Nijssen, B., & Lettenmaier, D. P. (2002). Water balance dynamics of a boreal forest watershed: White Gull Creek basin, 1994–1996. *Water Resour. Res.*, *38*. doi:10.1029/2001WR000699.

Noël, P., Rousseau, A. N., Paniconi, C., & Nadeau, D. F. (2014). Algorithm for delineating and extracting hillslopes and hillslope width functions from gridded elevation data. *J. Hydrol. Eng.*, *19*, 366–374. doi:10.1061/(ASCE)HE.1943-5584.0000783.

Norman, J. M., & Campbell, G. S. (1989). Canopy structure. In R. W. Pearcy, J. R. Ehleringer, H. A. Mooney, & P. W. Rundel (Eds.), *Plant physiological ecology* (pp. 301–325). Dordrecht, The Netherlands: Springer.

Ochsner, T. E., Sauer, T. J., & Horton, R. (2007). Soil heat storage measurements in energy balance studies. *Agron. J.*, *99*, 311–319. doi:10.2134/agronj2005.0103S.

Oke, T. R. (1987). *Boundary layer climates.* Routledge, New York, USA.

Oldroyd, H. J., Pardyjak, E. R., Huwald, H., & Parlange, M. B. (2016). Adapting tilt corrections and the governing flow equations for steep, fully three-dimensional, mountainous terrain. *Boundary-Layer Meteorol.*, *159*, 539–565. doi:10.1007/ s10546-015-0066-0.

Oliphant, A., Grimmond, C., Zutter, H., Schmid, H., Su, H.-B., Scott, S., Offerle, B., Randolph, J., & Ehman, J. (2004). Heat storage and energy balance fluxes for a temperate deciduous forest. *Agric. For. Meteorol.*, *126*, 185–201. doi:10.1016/j. agrformet.2004.07.003.

Olmo, F. J., Vida, J., Foyo, I., Castro-Diez, Y. & Alados-Arboledas, L. (1999). Prediction of global irradiance on inclined surfaces from horizontal global irradiance. *Energy*. *24*, 689-704. doi:10.1016/S0360-5442(99)00025-0.

Oltchev, A., Cermak, J., Gurtz, J., Tishenko, A., Kiely, G., Nadezhdina, N., Zappa, M., Lebedeva, N., Vitvar, T., Albertson, J. et al. (2002). The response of the water fluxes of the boreal forest region at the Volga's source

area to climatic and land-use changes. *Phys. Chem. Earth Pt A/B/C*, *27*, 675–690. doi:10.1016/ S1474-7065(02)00052-9.

Ono, K., Mano, M., Miyata, A., & Inoue, Y. (2008). Applicability of the planar fit technique in estimating surface fluxes over flat terrain using eddy covariance. *J. Agric. Meteorol. (Jpn)*, *64*, 121–130.

Ouranos. (2015). *Sommaire de la synthèse des connaissances sur les changements climatiques au Québec (Édition 2015)*. Consortium Ouranos, Montréal, Canada.

Pan, Y., Birdsey, R. A., Fang, J., Houghton, R., Kauppi, P. E., Kurz, W. A., Phillips, O. L., Shvidenko, A., Lewis, S. L., Canadell, J. G., Ciais, P., Jackson, R. B., Pacala, S., McGuire, A. D., Piao, S., Rautiainen, A., Sitch, S., & Hayes, D. (2011). A large and persistent carbon sink in the world's forests. *Science*, *333*, 988–993. doi:10. 1126/science.1201609.

Papale, D., Reichstein, M., Aubinet, M., Canfora, E., Bernhofer, C., Kutsch, W., Longdoz, B., Rambal, S., Valentini, R., Vesala, T. et al. (2006). Towards a standardized processing of Net Ecosystem Exchange measured with eddy covariance technique: algorithms and uncertainty estimation. *Biogeosciences*, *3*, 571–583.

Papale, D., & Valentini, R. (2003). A new assessment of European forests carbon exchanges by eddy fluxes and artificial neural network spatialization. *Glob. Change Biol.*, *9*, 525–535. doi:10.1046/j.1365-2486.2003.00609.x.

Parviainen, J., Pomeroy, J. et al. (2000). Multiple-scale modelling of forest snow sublimation: initial findings. *Hydrol. Process.*, *14*, 2669–2681. doi:10.1002/ 1099-1085(20001030)14:15<2669::AID-HYP85>3.0.CO;2-Q.

Pastorello, G., Agarwal, D., Papale, D., Samak, T., Trotta, C., Ribeca, A., Poindexter, C., Faybishenko, B., Gunter, D., Hollowgrass, R. et al. (2014). Observational data patterns for time series data quality assessment. In *2014 IEEE 10th International Conference on e-Science* (pp. 271–278). IEEE volume 1.

Payeur-Poirier, J.-L., Coursolle, C., Margolis, H. A., & Giasson, M.-A. (2012). CO_2 fluxes of a boreal black spruce chronosequence in eastern North America. *Agric. For. Meteorol.*, *153*, 94–105. doi:10.1016/j.agrformet.2011.07.009.

Penman, H. L. (1948). Natural evaporation from open water, bare soil and grass. *Proc. R. Soc. Lond.*, *A193*, 120–145.

Pierre, A., Jutras, S., Smith, C., Kochendorfer, J., Fortin, V., & Anctil, F. (2019). Evaluation of catch efficiency transfer functions for unshielded and single-Alter shielded solid precipitation measurements. *J. Atmos. Ocean. Tech.* doi:10.1175/ JTECH-D-18-0112.1.

Pieruschka, R., Huber, G., & Berry, J. A. (2010). Control of transpiration by radiation. *P. Natl. Acad. Sci. USA*, *107*, 13372–13377. doi:10.1073/pnas.0913177107.

Poggio, L. P., Furger, M., Prévôt, A. H., Graber, W. K., & Andreas, E. L. (2000). Scintillometer wind measurements over complex terrain. *J. Atmos. Ocean. Technol.*, *17*, 17–26. doi:10.1175/1520-0426(2000)017<0017:SWMOCT>2.0.CO;2.

Pomeroy, J., Parviainen, J., Hedstrom, N., & Gray, D. (1998). Coupled modelling of forest snow interception and sublimation. *Hydrol. Process.*, *12*, 2317–2337. doi:10.1002/(SICI)1099-1085(199812)12:15<2317::AID-HYP799>3.0.CO;2-.

Pomeroy, J. W., Marks, D., Link, T., Ellis, C., Hardy, J., Rowlands, A., & Granger, R. (2009). The impact of coniferous forest temperature on incoming longwave radiation to melting snow. *Hydrol. Process.*, *23*, 2513–2525. doi:10.1002/hyp.7325.

Pongratz, J., Bounoua, L., DeFries, R. S., Morton, D. C., Anderson, L. O., Mauser, W., & Klink, C. A. (2006). The impact of land cover change on surface energy and water balance in Mato Grosso, Brazil. *Earth Interact.*, *10*, 1–17. doi:10.1175/EI176.1.

Pypker, T. G., Bond, B. J., Link, T. E., Marks, D., & Unsworth, M. H. (2005). The importance of canopy structure in controlling the interception loss of rainfall: examples from a young and an old-growth Douglas-fir forest. *Agric. For. Meteorol.*, *130*, 113–129. doi:10.1016/j.agrformet.2005.03.003.

Reda, I., & Andreas, A. (2004). Solar position algorithm for solar radiation applications. *Sol. Energy*, *76*, 577–589. doi:10.1016/j.solener.2003.12.003.

Reichstein, M., Falge, E., Baldocchi, D., Papale, D., Aubinet, M., Berbigier, P., Bernhofer, C., Buchmann, N., Gilmanov, T., & Granier, A. (2005). On the separation of net ecosystem exchange into assimilation and ecosystem respiration: review and improved algorithm. *Glob. Change Biol.*, *11*, 1424–1439. doi:10.1111/j.1365-2486.2005.001002.x.

Reid, T., Essery, R., Rutter, N., & King, M. (2014). Data-driven modelling of shortwave radiation transfer to snow through boreal birch and conifer canopies. *Hydrol. Process.*, *28*, 2987–3007. doi:10.1002/hyp.9849.

Reifsnyder, W. E., Furnival, G., & Horowitz, J. (1971). Spatial and temporal distribution of solar radiation beneath forest canopies. *Agric. Meteorol.*, *9*, 21–37. doi:10.1016/0002-1571(71)90004-5.

Ricard, J.-P., Messier, C., Delagrange, S., & Beaudet, M. (2003). Do understory sapling respond to both light and below-ground competition?: a field experiment in a northeastern American hardwood forest and a literature review. *Ann. For. Sci.*, *60*, 749– 756. doi:10.1051/forest:2003069.

Rim, C. S. (2009). The effects of urbanization, geographical and topographical conditions on reference evapotranspiration. *Climatic Change. 97*, 483-514. doi:10.1007/s10584-009-9618-y.

Ritter, E., Dalsgaard, L., & Einhorn, K. S. (2005). Light, temperature and soil moisture regimes following gap formation in a semi-natural beech-dominated forest in Denmark. *Forest Ecol. Manag.*, *206*, 15–33. doi:10.1016/j.foreco.2004.08.011.

Ross, J., & Sulev, M. (2000). Sources of errors in measurements of PAR. *Agric. For. Meteorol.*, *100*, 103–125. doi:10.1016/S0168-1923(99)00144-6.

Rotach, M. W., Stiperski, I., Fuhrer, O., Goger, B., Gohm, A., Obleitner, F., Rau, G., Sfyri, E., & Vergeiner, J. (2017). Investigating exchange processes over complex topography: the Innsbruck Box (i-Box). *Bull. Am. Meteorol. Soc.*, *98*, 787–805. doi:10.1175/BAMS-D-15-00246.1.

Rotach, M. W., Wohlfahrt, G., Hansel, A., Reif, M., Wagner, J., & Gohm, A. (2014). The world is not flat: Implications for the global carbon balance. *Bull. Am. Meteorol. Soc.*, *95*, 1021–1028. doi:10.1175/BAMS-D-13-00109.1.

RPG (2014). *RPG-MWSC-160: Microwave scintillometer operation & software guide (2nd edition)*. Radiometer Physics GmbH, Meckenheim, Germany.

Samain, B., Defloor, W., & Pauwels, V. R. (2012). Continuous time series of catchment-averaged sensible heat flux from a large aperture scintillometer: Efficient estimation of stability conditions and importance of fluxes under stable conditions. *J. Hydrometeorol.*, *13*, 423–442. doi:10.1175/JHM-D-11-030.1.

Samain, B., Ferket, B. V., Defloor, W., & Pauwels, V. R. (2011). Estimation of catchment averaged sensible heat fluxes using a large aperture scintillometer. *Water Resour. Res.*, *47*. doi:10.1029/2009WR009032.

Saugier, B., Granier, A., Pontailler, J., Dufrene, E., & Baldocchi, D. (1997). Transpiration of a boreal pine forest measured by branch bag, sap flow and micrometeorological methods. *Tree Physiol.*, *17*, 511–519. doi:10.1093/treephys/17.8-9.511.

Schaphoff, S., Reyer, C. P., Schepaschenko, D., Gerten, D., & Shvidenko, A. (2016). Tamm Review: Observed and projected climate change impacts on Russia's forests and its carbon balance. *Forest Ecol. Manag.*, *361*, 432–444. doi:10.1016/j. foreco.2015.11.043.

Sécurité Publique Canada (2019) Base de données canadienne sur les catastrophes. Consulté le 10 avril 2019. http://bdc.securitepublique.gc.ca/

Seiller, G., & Anctil, F. (2014). Climate change impacts on the hydrologic regime of a Canadian river: comparing uncertainties arising from climate natural variability and lumped hydrological model structures. *Hydrol. Earth Syst. Sci.*, *18*, 2033–2047. doi:10.5194/hess-18-2033-2014.

Sellers, P., Hall, F., Margolis, H., Kelly, B., Baldocchi, D., den Hartog, G., Cihlar, J., Ryan, M. G., Goodison, B., Crill, P. et al. (1995). The Boreal Ecosystem– Atmosphere Study (BOREAS): an overview and early results from the 1994 field year. *Bull. Am. Meteorol. Soc.*, *76*, 1549–1577. doi:10.1175/1520-0477(1995)076<1549:TBESAO>2.0.CO;2.

Sellers, P. J. (1985). Canopy reflectance, photosynthesis and transpiration. *Int. J. Remote Sens.*, *6*, 1335–1372. doi:10.1080/01431168508948283.

Sellers, P. J., Hall, F. G., Kelly, R. D., Black, T. A., Baldocchi, D., Berry, J., Ryan, M., Ranson, K. J., Crill, P. M., Lettenmaier, D. P. et al. (1997). BOREAS in 1997: Experiment overview, scientific results, and future directions. *J. Geophys. Res. Atmos.*, *102*, 28731–28769. doi:10.1029/97JD03300.

Serrano-Ortiz, P., Sánchez-Cañete, E., Olmo, F., Metzger, S., Pérez-Priego, O., Carrara, A., Alados-Arboledas, L., & Kowalski, A. (2016). Surface-parallel sensor orientation for assessing energy balance components on mountain slopes. *Boundary-Layer Meteorol.*, *158*, 489–499. doi:10.1007/s10546-015-0099-4.

Sevruk, B., Ondrás, M., & Chvíla, B. (2009). The WMO precipitation measurement intercomparisons. *Atmos. Res.*, *92*, 376–380. doi:10.1016/j.atmosres.2009. 01.016.

Seyednasrollah, B., Kumar, M., & Link, T. E. (2013). On the role of vegetation density on net snow cover radiation at the forest floor. *J. Geophys. Res. Atmos.*, *118*, 8359– 8374. doi:10.1002/jgrd.50575.

Sfyri, E., Rotach, M. W., Stiperski, I., Bosveld, F. C., Lehner, M., & Obleitner, F. (2018). Scalar-flux similarity in the layer near the surface over mountainous terrain. *Boundary-Layer Meteorol.*, *169*(1): 11–46. doi:10.1007/s10546-018-0365-3.

Shimizu, T. (2015). Effect of coordinate rotation systems on calculated fluxes over a forest in complex terrain: a comprehensive comparison. *Boundary-Layer Meteorol., 156*, 277-301. doi:10.1007/s10546-015-0027-7.

Sicart, J. E., Essery, R. L., Pomeroy, J. W., Hardy, J., Link, T., & Marks, D. (2004). A sensitivity study of daytime net radiation during snowmelt to forest canopy and atmospheric conditions. *J. Hydrometeorol.*, *5*, 774–784. doi:10.1175/ 1525-7541(2004)005<0774:ASSODN>2.0.CO;2.

Simic, A., Fernandes, R., & Wang, S. (2014). Assessing the impact of leaf area index on evapotranspiration and groundwater recharge across a shallow water region for diverse land cover and soil properties. *J. Water Resour. Hydraul. Eng*, *3*, 60–73.

Skartveit, A., Olseth, J. A., & Tuft, M. E. (1998). An hourly diffuse fraction model with correction for variability and surface albedo. *Sol. Energy*, *63*, 173–183. doi:10. 1016/S0038-092X(98)00067-X.

Sokal, R., Michener, C. (1967). The effects of different numerical technique on the phonetic classification of bees of the *hoplitis* complex (Megachilidae). *Proc. Linn. Soc. London, 178*(1, 59–74. doi:10.1111/j.1095-8312.1967.tb00963.x

Stähli, M., Jonas, T., & Gustafsson, D. (2009). The role of snow interception in winter-time radiation processes of a coniferous sub-alpine forest. *Hydrol. Process.*, *23*, 2498–2512. doi:10.1002/hyp.7180.

Stiperski, I., Calaf, M., & Rotach, M. W. (2019). Scaling, anisotropy and complexity in near-surface atmospheric turbulence. *J. Geophys. Res. Atmos., 124*(3). doi:10.1029/ 2018JD029383.

Stiperski, I., & Rotach, M. W. (2016). On the measurement of turbulence over complex mountainous terrain. *Boundary-Layer Meteorol.*, *159*, 97–121. doi:10.1007/ s10546-015-0103-z.

Storck, P., Lettenmaier, D. P., & Bolton, S. M. (2002). Measurement of snow interception and canopy effects on snow accumulation and melt in a mountainous maritime climate, Oregon, United States. *Water Resour. Res.*, *38*. doi:10.1029/2002WR001281.

Stoy, P. C., Mauder, M., Foken, T., Marcolla, B., Boegh, E., Ibrom, A., Arain, M. A., Arneth, A., Aurela, M., Bernhofer, C. et al. (2013). A data-driven analysis of energy balance closure across FLUXNET research sites: The role of landscape scale heterogeneity. *Agric. For. Meteorol.*, *171*, 137–152. doi:10.1016/j.agrformet.2012.11.004.

Stull, R. B. (1988). *An introduction to boundary layer meteorology*. Springer, Dordrecht, The Netherlands.

Suni, T., Rinne, J., Reissell, A., Altimir, N., Keronen, P., Rannik, U., Maso, M., Kulmala, M., & Vesala, T. (2003). Long-term measurements of surface fluxes above a Scots pine forest in Hyytiälä, southern Finland, 1996-2001. *Boreal Environ. Res.*, *8*, 287–302.

Talbot, J., Plamondon, A., Levesque, D., Aube, D., Prevos, M., Chazalmartin, F., & Gnocchini, M. (2006). Relating snow dynamics and balsam fir stand characteristics, Montmorency Forest, Quebec. *Hydrol. Process.*, *20*, 1187–1199. doi:10.1002/ hyp.5938.

Ter-Mikaelian, M. T., & Korzukhin, M. D. (1997). Biomass equations for sixty-five North American tree species. *For. Ecol. Manage.*, *97*, 1–24. doi:10.1016/ S0378-1127(97)00019-4.

Tesemma, Z., Wei, Y., Peel, M., & Western, A. (2015). Including the dynamic relationship between climatic variables and leaf area index in a hydrological model to improve streamflow prediction under a changing climate. *Hydrol. Earth Syst. Sci.*, *19*, 2821–2836. doi:10.5194/hess-19-2821-2015.

Thum, T., Aalto, T., Laurila, T., Aurela, M., Kolari, P., & Hari, P. (2007). Parametrization of two photosynthesis models at the canopy scale in a northern boreal Scots pine forest. *Tellus B*, *59*, 874–890. doi:10.1111/j.1600-0889.2007.00305.x.

Toba, T., & Ohta, T. (2005). An observational study of the factors that influence interception loss in boreal and temperate forests. *J. Hydrol.*, *313*, 208–220. doi:10.1016/j.jhydrol.2005.03.003.

Tremblay, Y., Rousseau, A. N., Plamondon, A. P., Levesque, D., & Jutras, S. (2008). Rainfall peak flow response to clearcutting 50% of three small watersheds in a boreal forest, Montmorency Forest, Quebec. *J. Hydrol.*, *352*, 67–76.

Tremblay, Y., Rousseau, A. N., Plamondon, A. P., Lévesque, D., & Prévost, M. (2009). Changes in stream water quality due to logging of the boreal forest in the Montmorency Forest, Quebec. *Hydrol. Process.*, *23*, 764–776. doi:10.1002/hyp.7175.

Tribbeck, M., Gurney, R., & Morris, E. (2006). The radiative effect of a fir canopy on a snowpack. *J. Hydrometeorol.*, *7*, 880–895. doi:10.1175/JHM528.1.

Turnipseed, A., Blanken, P., Anderson, D., & Monson, R. K. (2002). Energy budget above a high-elevation subalpine forest in complex topography. *Agric. For. Meteorol.*, *110*, 177–201. doi:10.1016/S0168-1923(01)00290-8.

Twine, T. E., Kustas, W., Norman, J., Cook, D., Houser, P., Meyers, T., Prueger, J., Starks, P., & Wesely, M. (2000). Correcting eddy-covariance flux underestimates over a grassland. *Agric. For. Meteorol.*, *103*, 279–300. doi:10.1016/ S0168-1923(00)00123-4.

Tymen, B., Vincent, G., Courtois, E. A., Heurtebize, J., Dauzat, J., Marechaux, I., & Chave, J. (2017). Quantifying micro-environmental variation in tropical rainforest understory at landscape scale by combining airborne LiDAR scanning and a sensor network. *Ann. For. Sci.*, *74*, 32–44. doi:10.1007/s13595-017-0628-z.

USDA (2007). *The Encyclopedia of Wood*. U.S. Department of Agriculture, Skyhorse Publishing Inc, New York, USA.

Van Gardingen, P., Jackson, G., Hernandez-Daumas, S., Russell, G., & Sharp, L. (1999). Leaf area index estimates obtained for clumped canopies using hemispherical photography. *Agric. For. Meteorol.*, *94*, 243–257. doi:10.1016/ S0168-1923(99)00018-0.

Van Kesteren, B., Hartogensis, O. K., van Dinther, D., Moene, A. F., & DeBruin, H. A. R. (2013). Measuring H_2O and CO_2 fluxes at field scales with scintillometry: Part I – Introduction and validation of four methods. *Agric. For. Meteorol.*, *178-179*, 75–87.

Van Wijk, W. (1963). *Physics of Plant Environment*. North Holland Publishing Co., Amsterdam, The Netherlands.

Verseghy, D. (2012). *CLASS–The Canadian Land Surface Scheme (version 3.6)*. Technical Report, Environment Canada, Science and Technology Branch.

Verseghy, D., McFarlane, N., & Lazare, M. (1993). CLASS — A Canadian land surface scheme for GCMs, II. Vegetation model and coupled runs. *Int. J. Climatol.*, *13*, 347– 370.

Verseghy, D. L. (1991). CLASS — A Canadian land surface scheme for GCMs. I. Soil model. *Int. J. Climatol.*, *11*, 111–133.

Verseghy, D. L. (2000). The Canadian Land Surface Scheme (CLASS): its history and future. *Atmos. Ocean*, *38*, 1–13. doi:10.1080/07055900.2000.9649637.

Verseghy, D. L., Saunders, I. R., Bowers, J., Huo, Z., & Bailey, W. (2000). Application of the Canadian Land Surface Scheme (CLASS) to the simulation of energy and water fluxes over alpine tundra. *Atmos. Ocean*, *38*, 37–55. doi:10.1080/07055900. 2000.9649639.

Vickers, D., & Mahrt, L. (1997). Quality control and flux sampling problems for tower and aircraft data. *J. Atmos. Ocean. Tech.*, *14*, 512–526.

Vuichard, N., & Papale, D. (2015). Filling the gaps in meteorological continuous data measured at FLUXNET sites with ERA-Interim reanalysis. *Earth Syst. Sci. Dat.*, *7*, 157–171. doi:10.5194/essd-7-157-2015.

Walker, X. J., Mack, M. C., & Johnstone, J. F. (2015). Stable carbon isotope analysis reveals widespread drought stress in boreal black spruce forests. *Glob. Change Biol.*, *21*, 3102–3113. doi:10.1111/gcb.12893.

Walland, D. J., & Simmonds, I. (1996). Sub-grid-scale topography and the simulation of Northern Hemisphere snow cover. *Int. J. Climatol.*, *16*, 961-982. doi:10.1002/(SICI)1097-0088(199609)16:9<961::AID-JOC72>3.0.CO;2-R.

Wang, S. (2005). Dynamics of surface albedo of a boreal forest and its simulation. *Ecol. Model.*, *183*, 477–494. doi:10.1016/j.ecolmodel.2004.10.001.

Wang, S., Grant, R. F., Verseghy, D. L., & Black, T. A. (2002). Modelling carbon-coupled energy and water dynamics of a boreal aspen forest in a general circulation model land surface scheme. *Int. J. Climatol.*, *22*, 1249–1265. doi:10.1002/joc.776.

Ward, H. C., Evans, J., Hartogensis, O., Moene, A., De Bruin, H., & Grimmond, C. (2013). A critical revision of the estimation of the latent heat flux from two-wavelength scintillometry. *Q. J. Roy. Meteorol. Soc.*, *139*, 1912–1922. doi:10. 1002/qj.2076.

Ward, H. C., Evans, J. G., & Grimmond, C. S. B. (2014). Multi-scale sensible heat fluxes in the suburban environment from large-aperture scintillometry and eddy covariance. *Boundary-Layer Meteorol.*, *152*, 65–89. doi:10.1007/s10546-014-9916-4.

Ward, H. C., Evans, J. G., & Grimmond, C. S. B. (2015a). Infrared and millimetre-wave scintillometry in the suburban environment - Part 2: Large-area sensible and latent heat fluxes. *Atmos. Meas. Tech.*, *8*, 1407–1424. doi:10.5194/amt-8-1407-2015.

Ward, H. C., Evans, J. G., Grimmond, C. S. B., & Bradford, J. (2015b). Infrared and millimetre-wave scintillometry in the suburban environment - Part 1: Structure parameters. *Atmos. Meas. Tech.*, *8*, 1385–1405. doi:10.5194/amt-8-1385-2015.

Ward, H. C. (2017). Scintillometry in urban and complex environments: a review. *Meas. Sci. Technol.*, *28*, 064005. doi:10.1088/1361-6501/aa5e85.

Watson, D. J. (1947). Comparative physiological studies on the growth of field crops: I. Variation in net assimilation rate and leaf area between species and varieties, and within and between years. *Ann. Bot. London*, *11*, 41–76.

Webb, E. K., Pearman, G. I., & Leuning, R. (1980). Correction of flux measurements for density effects due to heat and water vapour transfer. *Q. J. R. Meteorol. Soc.*, *106*, 85–100.

Wharton, S., Ma, S., Baldocchi, D., Falk, M., Newman, J., Osuna, J., & Bible, K. (2017). Influence of regional nighttime atmospheric regimes on canopy turbulence and gradients at a closed and open forest in mountain-valley terrain. *Agric. For. Meteorol.*, *237*, 18–29. doi:10.1016/j.agrformet.2017.01.020.

Whiteman, C. D., & Allwine, K. J. (1986). Extraterrestrial solar radiation on inclined surfaces. *Environ. Soft.*, *1*, 164–169.

Wigmosta, M. S., Vail, L. W., & Lettenmaier, D. P. (1994). A distributed hydrology-vegetation model for complex terrain. *Water Resour. Res.*, *30*, 1665–1679. doi:10. 1029/94WR00436.

Wilczak, J. M., Oncley, S. P., & Stage, S. A. (2001). Sonic anemometer tilt correction algorithms. *Boundary-Layer Meteorol.*, *99*, 127–150. doi:10.1023/A:1018966204465.

Williams, M. W., Losleben, M., Caine, N. & Greenland, D. (1996). Changes in climate and hydrochemical responses in a high-elevation catchment in the Rocky Mountains, U.S.A. *Limnol. Oceanogr. 41*, 939-946. doi:10.4319/lo.1996.41.5.0939.

Wohlfahrt, G., Hammerle, A., Niedrist, G., Scholz, K., Tomelleri, E., & Zhao, P. (2016). On the energy balance closure and net radiation in complex terrain. *Agric. For. Meteorol.*, *226*, 37–49. doi:10.1016/j.agrformet.2016.05.012.

Wohlfahrt, G., Irschick, C., Thalinger, B., Hörtnagl, L., Obojes, N., & Hammerle, A. (2010). Insights from independent evapotranspiration estimates for closing the energy balance: a grassland case study. *Vadose Zone J.*, *9*, 1025–1033. doi:10. 2136/vzj2009.0158.

Wyngaard, J., Izumi, Y., & Collins, S. A. (1971). Behavior of the refractive-index structure parameter near the ground. *J. Opt. Soc. Am.*, *61*, 1646–1650. doi:10. 1364/JOSA.61.001646.

Yang, D. (2014). Double fence intercomparison reference (DFIR) vs. bush gauge for "true" snowfall measurement. *J. Hydrol.*, *509*, 94–100. doi:10.1016/j.jhydrol. 2013.08.052.

Yang, R., Friedl, M. A., & Ni, W. (2001). Parameterization of shortwave radiation fluxes for non-uniform vegetation canopies in land surface models. *J. Geophys. Res. Atmos.*, *106*, 14275–14286. doi:10.1029/2001JD900180.

Yee, M. S., Pauwels, V. R., Daly, E., Beringer, J., Rüdiger, C., McCabe, M. F., & Walker, J. P. (2015). A comparison of optical and microwave scintillometers with eddy covariance derived surface heat fluxes. *Agric. For. Meteorol.*, *213*, 226–239. doi:10.1016/j.agrformet.2015.07.004.

Zeweldi, D. A., Gebremichael, M., Wang, J., Sammis, T., Kleissl, J., & Miller, D. (2010). Intercomparison of sensible heat flux from large aperture scintillometer and eddy covariance methods: Field experiment over a homogeneous semi-arid region. *Boundary-Layer Meteorol.*, *135*, 151–159. doi:10.1007/s10546-009-9460-9.

Zha, T., Barr, A. G., van der Kamp, G., Black, T. A., McCaughey, J. H., & Flanagan, L. B. (2010). Interannual variation of evapotranspiration from forest and grassland ecosystems in western Canada in relation to drought. *Agric. For. Meteorol., 150*, 1476–1484. doi:10.1016/j.agrformet.2010.08.003.

Zhang, L., Walker, G. R., & Dawes, W. (1999). *Predicting the effect of vegetation changes on catchment average water balance*. Technical Report 99/12, Cooperative Research Center for Catchment Hydrology, CSIRO Land and Water, Canberra, Australia.

Zhao, W., & Qualls, R. J. (2005). A multiple-layer canopy scattering model to simulate shortwave radiation distribution within a homogeneous plant canopy. *Water Resour. Res.*, *41*. doi:10.1029/2005WR004016.

Zheng, D., Hunt, E. R., & Running, S. W. (1996). Comparison of available soil water capacity estimated from topography and soil series information. *Landscape Ecol.*, *11*, 3-14. doi:10.1007/BF02087109.

Zitouna-Chebbi, R., Prévot, L., Jacob, F., Mougou, R. & Voltz, M. (2012). Assessing the consistency of eddy covariance measurements under conditions of sloping topography within a hilly agricultural catchment. *Agric. For. Meteorol*., *164*, 123-135. doi:10.1016/j.agrformet.2012.05.010.

Annexe A – Arbres instrumentés

Une courte description de l'instrumentation déployée pour calculer ΔQ_b est faite à la section 2.4.3. Dans cette annexe, le détail du montage expérimental est présenté. Tel que mentionné, 39 thermistors ont été installés dans cinq arbres : trois sapins baumiers (*Abies balsamea*), une épinette blanche (*Picea glauca* (Moench) Voss) et un bouleau blanc (*Betula papyrifera*). Le tableau suivant décrit quelques caractéristiques de ces arbres essentielles au calcul du stockage de chaleur dans ceux-ci.

Tableau A 1: Caractéristiques des arbres instrumentés près de la station Juvénile

Espèce	Sapin baumier	Sapin baumier	Sapin baumier	Bouleau blanc	Épinette blanche
Numéro	1	2	3	-	-
Position vs. Juvénile	SE	SO	O	SE	SO
DBH [m]	0.131	0.140	0.074	0.078	0.087
h_v [m]	8	8.1	6.4	7.1	6
Hauteur [m] (premières branches)	2.34	1.89	2.12	2.38	1.8
Diamètre [m] (premières branches)	0.017	0.019	0.011	0.027	0.014
Longueur [m] (premières branches)	1.38	1.48	0.83	1.84	0.79
Hauteur [m] (dernières branches)	8	7.6	6.4	6.1	5.6
Diamètre [m] (dernières branches)	0.0032	0.0064	0.0016	0.0064	0.0095
Longueur [m] (dernières branches)	0.1	0.2	0.1	0.5	0.3
Densité de branches sur le tronc [m^{-1}]	20	32	17	5	30

Également, la section 2.4.2 décrit brièvement la localisation des 39 thermistors dans ces 5 arbres. Pour plus de clarifications, la figure suivante schématise en détail ces 39 senseurs avec leur hauteur et leur position :

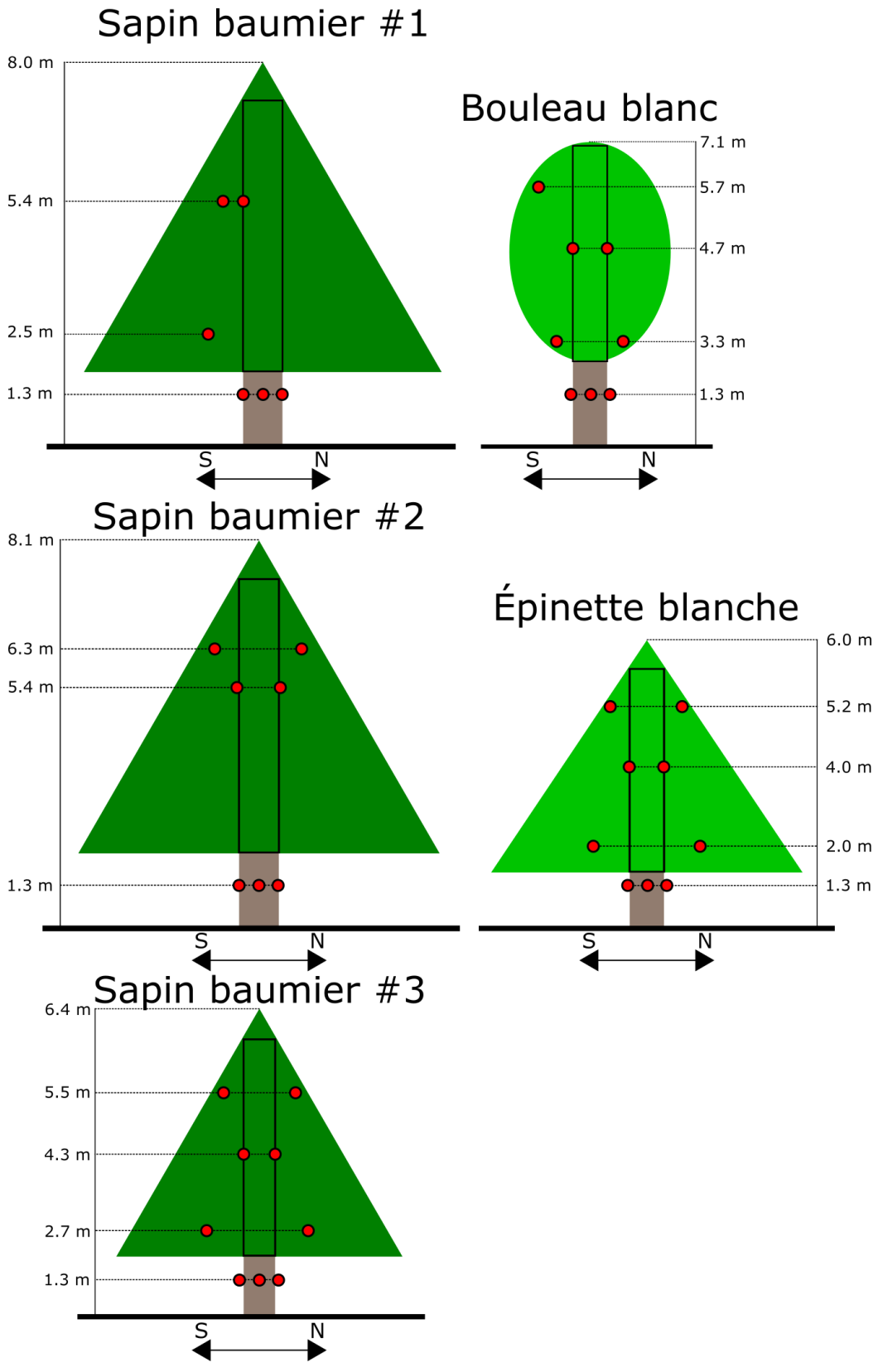

Figure A.1 : Localisation des thermistors dans les cinq arbres instrumentés.